Multi-Scale Modelling and Design of Thermal Energy Storage (TES) Devices Based on Cementitious Materials.

by

Mohammad Rahjoo

Supervisors:

Dr. Jorge Sánchez Dolado

Dr. María Esther Rojas Bravo

University of the Basque Country - UPV/EHU

Materials Physics Center (CSIC-UPV/EHU)

San Sebastián, Spain

February 2024

Abstract

This thesis investigates the potential of using geopolymer concrete as an alternative to ordinary Portland cement (OPC) for thermal energy storage (TES) systems, particularly for high-temperature applications. OPC concrete, the conventional material proposed in TES systems, exhibits thermal degradation at elevated temperatures, limiting its suitability for high-temperature applications. Geopolymer concrete, on the other hand, offers several advantages over OPC concrete for TES, including superior thermal stability, higher heat capacity, and lower environmental impact.

To evaluate the potential of geopolymer concrete for TES, a broad research approach was employed, combining numerical modeling, experimental validation, and machine learning optimization. A 2-D numerical model was developed to simulate the thermal performance of TES prototypes made with OPC and geopolymer-based materials. The model successfully demonstrated the superior thermal performance of geopolymer concrete compared to OPC concrete, particularly at high temperatures.

Experimental validation of the numerical model was conducted using real TES prototypes made of OPC and geopolymer concrete. The experiments confirmed the superior thermal stability and storage capacity of geopolymer concrete, with temperature differences up to 30-40°C and storage capacity up to 2-3.5x higher than OPC concrete.

To further optimize the design and performance of TES systems based on geopolymer concrete, a 3-D computational model was developed. This model enabled systematic evaluation of design choices and operating parameters to maximize the performance of TES systems for up-scale approaches.

Finally, machine learning techniques were employed to optimize the design and performance of TES systems based on solid materials. A decision tree machine learning (ML) model was trained to predict TES performance metrics based on a dataset generated from the validated numerical model. The ML model was then used in conjunction with multi-objective optimization to identify Pareto optimal solutions that balanced objectives such as efficiency and pressure drop for up-scale design.

Resumen

Esta tesis investiga el potencial del hormigón geopolimérico como alternativa al cemento Portland (OPC) para sistemas de almacenamiento de energía térmica (TES), particularmente para aplicaciones de alta temperatura. El hormigón de OPC, material convencional propuesto en los sistemas TES, presenta degradación térmica a temperaturas elevadas, lo que limita su idoneidad para las aplicaciones de alta temperatura. El hormigón geopolimérico, sin embargo, ofrece varias ventajas sobre el hormigón de OPC para TES, como una estabilidad térmica superior, una mayor capacidad calorífica y un menor impacto ambiental.

Para evaluar el potencial del hormigón geopolimérico para TES, se empleó un enfoque de investigación amplio que combina modelado numérico, validación experimental y optimización de aprendizaje automático. Se desarrolló un modelo numérico bidimensional para simular el rendimiento térmico de prototipos TES fabricados con OPC y materiales a base de geopolímeros. El modelo demostró con éxito el rendimiento térmico superior del hormigón geopolimérico en comparación con el hormigón de OPC, especialmente a temperaturas altas.

La validación experimental del modelo numérico se realizó utilizando prototipos TES reales fabricados con OPC y hormigón geopolimérico. Los experimentos confirmaron la superior estabilidad térmica y capacidad de almacenamiento del hormigón geopolimérico, con diferencias de temperatura de hasta 30-40 °C y capacidad de almacenamiento hasta 2-3,5 veces mayor que el hormigón de OPC.

Para optimizar aún más el diseño y el rendimiento de los sistemas TES basados en hormigón geopolimérico, se desarrolló un modelo computacional en 3D. Este modelo permitió una evaluación sistemática de las opciones de diseño y los parámetros de operación para maximizar el rendimiento de los sistemas TES para enfoques de mayor escala.

Finalmente, se emplearon técnicas de aprendizaje automático para optimizar el diseño y el rendimiento de los sistemas TES basados en materiales sólidos. Se entrenó un modelo de aprendizaje automático (ML) de árbol de decisiones para predecir métricas de rendimiento de TES basado en un conjunto de datos generado a partir del modelo numérico validado. El modelo ML se utilizó luego en conjunto con la optimización multiobjetivo para identificar soluciones Pareto óptimas que equilibraran objetivos como la eficiencia y la caída de presión para un diseño a mayor escala.

To my parents I extend my deepest appreciation.

Grateful for the countless individuals who have encouraged and supported me, and for the inspiration I have drawn from all those who have touched my life.

And most of all, Negar. Thank you for being my rock, my cheerleader, and my best friend.

Related dissemination and projects

Geopolymer concrete was presented as a potential high-temperature TES material. Parametric studies were conducted to optimize the performance of geopolymer concrete for high-temperature applications. Data-driven approaches were proposed for the design and optimization of solid-based TES systems. The research on geopolymer concrete as a high-temperature thermal energy storage (TES) material has been presented by several means. The diverse dissemination of these findings, encompassing both publications and presentations, has effectively communicated the applications of geopolymer concrete in the field of thermal energy storage.

Publications

[1] Geopolymer concrete performance study for high-temperature thermal energy storage (TES) applications (M Rahjoo, G Goracci, P Martauz, E Rojas, JS Dolado)

Sustainability 14 (3), 1937 - https://doi.org/10.3390/su14031937

[2] Thermal Energy Storage (TES) Prototype Based on Geopolymer Concrete for High-Temperature Applications (M Rahjoo, G Goracci, JJ Gaitero, P Martauz, E Rojas, JS Dolado)

Materials 15 (20), 7086 - https://doi.org/10.3390/ma15207086

[3] A Numerical Study of Geopolymer Concrete Thermal Energy Storage: Benchmarking TES Module Design and Optimizing Thermal Performance (M Rahjoo, E Rojas, G Goracci, JJ Gaitero, P Martauz, JS Dolado)

Journal of Energy Storage 74 (B), 109389 - https://doi.org/10.1016/j.est.2023.109389

[4] Data-Driven and Machine Learning-Enabled Design and Optimization of Solid-Based Thermal Energy Storage Units (M Rahjoo, E Rojas, G Goracci, JS Dolado)

Submitted - http://dx.doi.org/10.2139/ssrn.4479433

[5] Exploring the Role of Surface Roughness in Concrete-Based Thermal Energy Storage Systems: A Computational Study (M Rahjoo, E Rojas, G Goracci, JS Dolado)

Submitted - http://dx.doi.org/10.2139/ssrn.4589146

[6] Numerical Approaches to Thermal Property Modelling and Design Optimization in Cementitious Sensible Thermal Energy Storage: A Review (M Rahjoo, JS Dolado, JJ Gaitero, A. Caggiano)

Under Preparation

[7] Sensible TES in cementitious composites – Book Chapter under RILEM TC 299-TES committee (M Rahjoo, JS Dolado, JJ Gaitero, A. Caggiano)

Under Preparation

Chapter I presents the motivation and objectives behind this research. Chapter II leverages the review in [6-7] to explore TES systems, cementitious materials, heat transfer, and geopolymer's potential based on [1]. Chapter III then builds on this knowledge, presenting the development and validation of a high-temperature TES prototype based on [2]. Subsequently, chapter IV utilizes insights from [3], [5], and [6-7] to develop and validate a numerical model for geopolymer TES systems, followed by an optimization study. Chapter V, drawing on [4], explores innovative machine learning for TES design.

Conferences and workshops

- Geopolymer concrete performance study for high temperature thermal energy storage (TES) applications - Workshop – Sustainable Materials for Energy Storage Solutions (San Sebastián, Spain, February 23-25, 2022)

- Geopolymer-based Concrete for high temperature thermal energy Storage - 1st Miracle Workshop (San Sebastián, Spain, May 4-6, 2022)

- Cement-based materials for thermal energy storage - Current Challenges in Materials for Thermal Energy Storage (Zaragoza, Spain, June 8-9, 2022)

- Geopolymer-based concrete for high-temperature thermal energy storage (TES) application - 12th Advances in Cement-Based Materials (Irvine, USA, July 11-13, 2022)

- Thermal Energy Storage (TES), Based on Geopolymer Concrete for High-Temperature Applications - RED-TES – Thermal energy storage for industrial heat and cold and for the building sector (Sevilla, Spain, November 23, 2022)

- Parametric Study and Optimization of Geopolymer based Concrete for High-Temperature Applications - The Sixth International Symposium on Innovative Materials and Processes in Energy Systems (Barcelona, Spain, October 25-28, 2022)

- Optimizing Geopolymer Concrete Thermal Energy Storage: A Parametric Study of Key Design Parameters for High-Temperature Applications - Eurotherm Seminar Innovative Solutions for Thermal Energy Storage Deployment (Lleida, Spain, May 24-26, 2023) - https://doi.org/10.21001/eurotherm.seminar.116.2023

- Geopolymer Concrete as a High Temperature Thermal Energy Storage Material - LTC Sarea Workshop, Euskampus Fundazioa (Bayonne, France, July 20, 2023)

- Data-Driven Design and Optimization of Solid-Based Thermal Energy Storage Systems - International Renewable Energy Storage and Systems Conference (IRES 2023) (Aachen, Germany, November 28-30, 2023)

- Geopolymer Concrete for High Temperature Thermal Energy Storage: A Sustainable and Circular Approach - 2nd International Workshop on Net Zero Carbon Buildings (Bath, UK, January 24- 25, 2024)

Related funded projects and working groups.

- ECRETE: Energy storage solutions based on CONCRETE - Proyectos de I+D+i Retos investigación 2018 (RTI2018) Project reference number: RTI2018-098554-B-I00 - https://www.ecrete.org/

- Grant PRE2019-087676 funded by MCIN/AEI/10.13039/501100011033 and co-financed by the European Social Fund under the 2019 call for grants for predoctoral contracts for the training of doctors contemplated in the State Training Subprogram of the State Program for the Promotion of Talent and its Employability in R&D&I, within the framework of the State Plan for Scientific and Technical Research and Innovation 2017–2020.

- International Union of Laboratories and Experts in Construction Materials, Systems and Structures (RILEM): Technical Committee 299-TES on thermal energy storage in cementitious composites. https://www.rilem.net/

Table of Contents

List of Tables

List of Figures

Nomenclature

Abbreviations

Abbreviation	Definition
TES	Thermal Energy Storage
SHS	Sensible Heat Storage
OPC	Ordinary Portland Cement
GEO	Geopolymer Concrete
FEM	Finite Element Method
FDM	Finite Difference Method
FVM	Finite Volume Method
CSP	Concentrating Solar Power
CA	Calcium Aluminate
CCN	Cement Chemist Notation
C-S-H	Calcium Silicate Hydrate
CH	Calcium Hydroxide
C-A-H	Calcium Aluminate Hydrate
HTF	Heat Transfer Fluid
TABS	Thermo-Active Building Systems
VCS	Ventilated Concrete Slabs
DSF	Double-Skin Facades
PCM	Phase Change Materials
CFD	Computational Fluid Dynamics
HX	Heat Exchanger
L-VEL (spf)	Interface in COMSOL for turbulent flow simulations
ML	Machine Learning
AI	Artificial Intelligence
SPH	Solar Process Heat
IWH	Industrial Waste Heat
MCDA	Multi-Criteria Decision Analysis
MOO	Multi-Objective Optimization
EMO	Evolutionary Multi-Objective Optimization
DT	Decision Tree
TPE	Tree-structured Parzen Estimator
MAE	Mean absolute error
MSE	Mean squared error
RMSE	Root mean squared error
EVS	Explained variance score
MAPE	Mean absolute percentage error

Symbols

Symbols	Units	Explanation
Q_S	[J]	Heat storage amount
Q_{src}	[J]	Heat source term
m	[kg]	Mass of material
C_P	[J/(kg·K)]	Specific heat capacity at constant pressure
T_0	[K or °C]	Initial temperature
T_f	[K or °C]	Final temperature
T_∞	[K or °C]	Ambient temperature
T_i	[K or °C]	Temperature at node i
T_e	[K or °C]	Average temperature in element e
α	[m^2/s]	Thermal diffusivity
k	[W/(m·K)]	Thermal conductivity
ρ	[kg/m^3]	Density of material
b	[m/s]	Thermal effusivity
∇	[m^{-1}]	Gradient operator
t	[s]	Time
x	[m]	Spatial coordinate in the x-direction
y	[m]	Spatial coordinate in the y-direction
z	[m]	Spatial coordinate in the z-direction
∂T/∂x	[°C/m]	Partial derivative of temperature with respect to x
∂T/∂y	[°C/m]	Partial derivative of temperature with respect to y
∂T/∂z	[°C/m]	Partial derivative of temperature with respect to z
$\hat{\imath}$	1	Unit vector in the x-direction
$\hat{\jmath}$	1	Unit vector in the y-direction
$\hat{k}$	1	Unit vector in the z-direction
$\overrightarrow{q''}$(x, y, z, t)	[W/m^2]	Heat flux vector in three-dimensional space
q''_{rad}	[W/m^2]	Radiative heat transfer rate per unit area
ε	-	Emissivity of a material, 0 (perfect reflector) to 1 (perfect emitter)
σ	[W/(m^2·K^4)]	Stefan-Boltzmann constant, $5.670374419 \times 10^{-8}$
q''_{conv}	[W/m^2]	Convective heat transfer rate per unit area
h	[W/(m^2·K)]	Convective heat transfer coefficient
N_e	-	Total number of elements
W_{ie}	-	Weight for node i in element e
N_p	-	Total number of basis functions
C_{ej}	-	Coefficient of basis function j
Φ_j	-	Basis function j
e	-	Element index
q_e	[W/m^3]	Heat source in element e
Δt	[s]	Time step size
u	[m/s]	Fluid velocity
PA	[Pa]	Thermodynamic pressure
αp	[K^{-1}]	Thermal expansion coefficient
τ	[N/m^2]	Viscous stress tensor

S	$[s^{-1}]$	Strain rate tensor
r_{xy}	-	Pearson's correlation coefficient
μ	[Pa·s]	Dynamic viscosity
ν	$[m^2/s]$	Kinematic viscosity
l	[m]	Characteristic length
Re	-	Reynolds number
k_s	[m]	Surface roughness
δ	[m]	Viscous sublayer thickness
k_T	$[m^2/s^2]$	Turbulent kinetic energy
ε_T	$[m^2/s^3]$	Turbulent dissipation rate
η_{charge}	-	Charging efficiency
$<T_{TES}>$	[K or °C]	Average Thermal Energy Storage temperature
R^2	-	R-squared value
y_i	-	Actual target value
$\hat{y}_i$	-	Predicted target value
$\bar{y}$	-	Mean of observed values
n	-	Number of samples
T_{HTF_out}	[°C]	Heat transfer fluid outlet temperature
ΔP	[Pa]	Heat transfer fluid pressure drop
$\dot{Q}$	[W]	Heat transfer fluid output heat rate

Chapter I.

Research Objectives

The transition towards a sustainable energy mix is a pressing global challenge, demanding the integration of renewable energy sources into existing energy systems. However, the intermittent nature of these sources poses a significant hurdle in their widespread adoption. Thermal energy storage (TES) emerges as a critical technology to overcome this challenge, enabling the storage of excess renewable energy during periods of surplus and its utilization when demand peaks. Sensible heat storage (SHS) stands as a widely employed TES method, where heat is stored within a material by raising its temperature. Conventionally, in concrete-based TES systems, cementitious materials, such as ordinary Portland cement (OPC) concrete, have been the primary choice for SHS applications due to their high heat capacity and cost-effectiveness. However, OPC concrete exhibits thermal degradation above 350ºC-400ºC, restricting its suitability for high-temperature TES applications.

The E-CRETE project is a research project funded by the Spanish Ministry of Science and Innovation that aims to develop new energy storage solutions based on concrete. The primary goal of this research is to investigate the viability of geopolymer concrete (GEO) as a substitute for OPC in thermal energy storage systems, particularly for high-temperature applications. The research is prompted by the limitations of OPC in TES systems, which exhibit thermal degradation above 400ºC. Conversely, geopolymer concrete shows potential advantages for TES, including improved thermal stability, higher heat capacity, and reduced environmental impact.

The thesis couples varied research methodologies, such as numerical modeling, experimental validation, and machine learning optimization, to assess the suitability of geopolymer concrete for TES. The initial phase involves the development and employment

of a 2-D numerical model for simulating the thermal performance of TES prototypes made with OPC and geopolymer materials. The numerical model serves as a proof of concept for the proposed material.

The research then proceeds with an experimental validation of the numerical model using real TES prototypes fabricated from OPC and geopolymer concretes. The experiments aim to confirm the superior thermal stability and storage capacity of geopolymer concrete.

The research further aims to optimize the design and performance of TES systems based on geopolymer concrete through the development of a 3-D computational fluid dynamics model. This model is intended to allow a systematic evaluation of design choices and operating parameters, maximizing the performance of TES systems for up-scale applications.

Lastly, the research aims to employ machine learning techniques for optimizing the design and performance of TES systems based on solid materials. A decision tree machine learning model is trained to predict TES performance metrics based on a dataset generated from the validated numerical model. The machine learning model is then used alongside multi-objective optimization to identify Pareto optimal solutions that balance efficiency and pressure drop objectives for up-scale design.

Chapter II studies GEO concrete as a promising alternative to OPC for TES applications. The manufacturing process of GEO concrete samples and defining their properties through experimental measurements are explained. A 2D finite element model to simulate and compare the thermal performance of GEO and OPC concrete is presented, providing preliminary evidence of the superior efficiency of GEO concrete.

Chapter III focuses on the experimental validation of TES prototypes constructed from GEO concrete and OPC concrete. It describes the process of fabricating the prototypes, setting up a test facility, and conducting thermal cycles under varying

temperature ranges. The chapter concludes with a comparative analysis of GEO and OPC performance metrics, supporting the superior thermal storage capabilities of GEO concrete highlighted in Chapter II.

Chapter IV extends the work of the previous chapters by developing a detailed 3D computational model to simulate the performance of GEO-based TES systems. This model allows for a systematic evaluation of various design parameters and their effects on TES system performance. It also helps identifying the most influential factors and the optimal configurations to maximize TES system efficiency and storage capacity, setting the stage for the next chapter.

Chapter V introduces machine learning and multi-objective optimization techniques to further enhance the design and performance of TES systems. It describes the process of gathering and preprocessing data to train a decision tree machine learning model, and then using this model with the Tree-Structured Parzen Estimator (TPE) algorithm. The chapter concludes with the validation of these solutions, proposing a modular and parallel arrangement of concrete TES modules for enhanced TES system performance.

In conclusion, the research offers a contribution to the field of thermal energy storage by introducing and validating GEO concrete as a more sustainable and efficient material for TES applications. It provides a thorough and systematic approach to designing and optimizing TES systems, leveraging numerical simulation, experimental validation, and machine learning optimization techniques. The research lays the groundwork for future exploration of TES systems, particularly for high-temperature applications.

Chapter II.

Background

2.1 Thermal Energy Storage (TES) Systems

Amidst the burgeoning discourse towards a renewable energy-driven future, thermal energy storage will undoubtedly play a focal role in shaping a more efficient, resilient, and sustainable energy system as it offers a compelling solution to the intermittency of renewable energy sources, warranting a consistent supply of thermal energy for a wide range of applications. Its versatility extends from individual buildings to district and even regional scales, encompassing power generation, industrial processes, and more.

In the renewable energy sector, TES can balance power fluctuations, enhance system adaptability, and facilitate the storage and distribution of energy from variable renewable sources. Functioning as temporal gatekeepers, they capture and preserve transient heat energy for future utilization. TES is a key component in various industries (Cabeza, 2020a), including solar power generation (Alva et al., 2017; Pelay et al., 2017; Zunft et al., 2011), industrial proceses (Brückner et al., 2015a; Miró et al., 2016a), and building applications (Navarro et al., 2016c, 2016a; Shaw et al., 1994).

IRENA (IRENA, 2020) posits that TES technologies hold a vast, as-of-yet untapped, potential in the energy transition across five key sectors: power, industry, district heating and cooling, cold-chain applications, and buildings. By 2030, it is predicted that TES-related costs in power generation could drop by over 50%, to an estimated USD 15 per kWh. In the industrial sector, sensible technology costs could decrease nearly 30%, from USD 35/kWh to USD 25/kWh.

In the building sector, improvements in material composition and system enhancements in TES technologies could boost efficiency levels up to 90% (IRENA,

2020). TES is projected to reduce the energy load in the EU-25 by 5,854,139 MWth over the next decade. This equates to thermal energy savings of 9,527,227 GWhth and a reduction in CO_2 emissions by 2,579,088,559 metric tons (Cabeza, 2020a). Such projections emphasize the principal role of TES in advancing sustainable energy practices, energy management and mitigating the impacts of global climate change.

TES systems can be broadly categorized into three types based on the method of storing energy: sensible heat storage, latent heat storage, and thermochemical storage. TES materials can be solids, liquids, and get used of phase change processes, such as melting or crystallization.

Sensible TES systems primarily rely on the temperature change of the storage medium, latent on the energy gained/released while the material changes phase at nearly constant temperature, while chemical TES systems exploit reversible thermochemical reactions to store heat. Thermochemical energy storage systems are inherently more intricate than sensible and latent heat systems, as they encompass not only heat transfer phenomena but also mass transfer considerations and the kinetics of chemical reactions. Figure 2-1 illustrates the three primary TES systems and their corresponding physical phase or chemical reaction type.

Within this broader renewable energy context, TES technology empowers us to store thermal energy for diverse applications down the line. It acts as an instrumental tool enhancing not only the stability and proficiency of energy systems but also mitigating environmental impacts (Cabeza, 2012a; Sarbu and Sebarchievici, 2018). The global market for TES could triple in size by 2030 to over 800 GWh (“Innovation outlook,” 2020). Forecasting the global market trends, TES is set to unleash its potential by claiming a whopping market size of $10.1 billion by 2027. The market dominion is held by sensible heat TES technologies, owing to their cost-affordability and comprehensive applicability (Pompei et al., 2023).

Sensible TES represents a mature and straightforward method for heat storage. It operates by altering the temperature of Sensible TES Materials, such as water, oil, rock beds, bricks, sand, concrete or soil, without any accompanying phase change (Alva et al., 2017; Becattini et al., 2017; Koçak et al., 2020). Performance of a sensible TES system is evaluated based on capacity, power, efficiency, charge and discharge time, and cost (González-Roubaud et al., 2017; Koçak et al., 2020). However, manifesting TES systems is not devoid of challenges. The hurdles span from the need for bespoke TES designs suiting individual applications, the stability and attributes of the materials employed, to the intricate process of melding TES into existing systems (Gunasekara et al., 2021a). Furthermore, Ge et al. (Ge et al., 2014) discuss the challenges and opportunities of TES technology in four aspects: materials, components, devices, and integration with energy networks. Each of these facets demands strategic planning and design for effective TES assimilation.

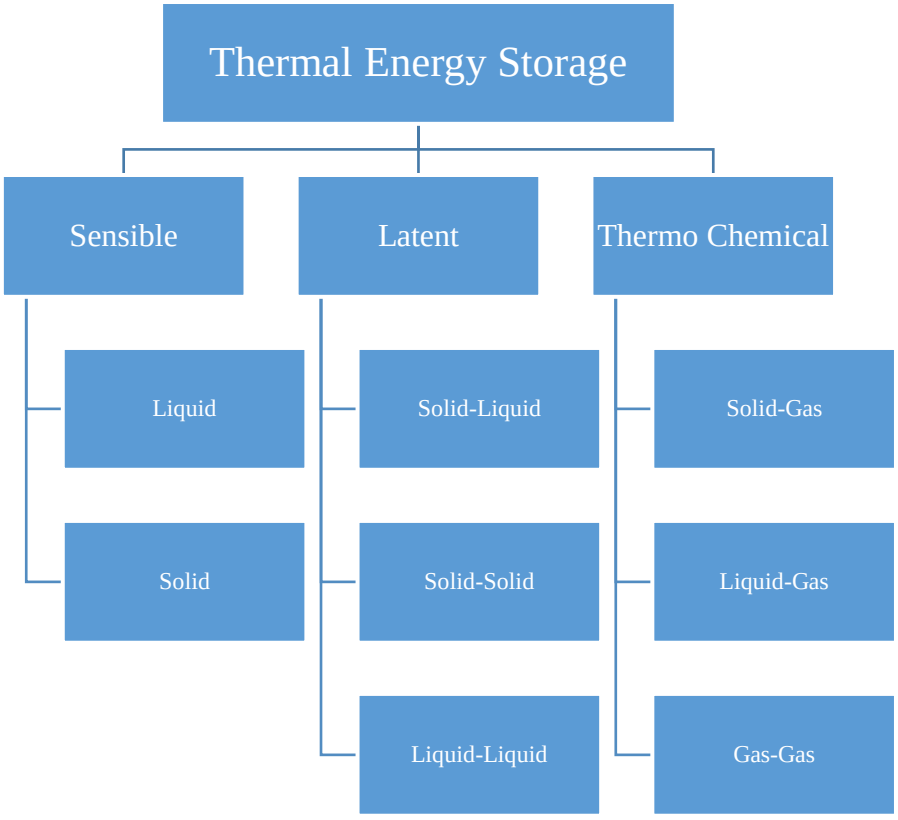

Figure 2-1. Thermal energy storage classification based on technology.

The diversity of TES systems in terms of temperature, power level, and heat transfer fluids necessitates tailored designs, media, and methods for specific applications (Bauer et al., 2012). TES systems span a remarkable temperature range, encompassing close to cryogenic conditions (-150°C) to scorching temperatures exceeding 1000°C. This expansive operating spectrum demands accurate selection of the storage medium and heat transfer fluid (HTF), the fluid responsible for transporting heat between the storage medium and the application. HTFs are classified into two primary categories: single-phase and two-phase.

Single-phase HTFs remain in a single fluid state throughout their operation, typically liquids or gases. Water, molten salts, and organic fluids are common examples. Two-phase HTFs undergo phase transitions between liquid and vapor states during operation, providing enhanced heat capacity and transfer coefficients. This property stems from the unique characteristics of phase change processes, which involve latent heat storage and rapid heat exchange. Water-steam and refrigerant-vapor mixtures are prominent examples of two-phase HTFs. The selection of HTFs for TES systems is governed by several factors, including the operating temperature range, desired heat transfer rates, cost, safety considerations, compatibility with the storage medium and an appropriate integration with the application and energy source.

On the other hand, TES systems can be distinguished as active, or passive based on the mechanism of energy transfer between the storage medium and the heat sink or source (Cabeza, 2020b, 2012b). Active TES systems employ external power sources, typically pumps or compressors, to circulate the HTF through the storage medium. Passive TES systems rely solely on natural convection or diffusion for heat transfer. Section 2.3 will present a detailed overview of diffusion type of heat transfer in solids.

Direct TES systems straight store heat within the HTF, eliminating the need for a separate storage medium. This simplifies system design but may be constrained by HTF material limitations, primarily pressure and temperature tolerances (Bauer et al., 2012). Indirect TES systems utilize two distinct media – the HTF and the storage medium – for heat storage. This separation allows for the use of HTFs with higher operating parameters,

broadening TES application horizons. Indirect storage systems can involve direct or indirect contact between the HTF and the storage medium. Direct contact facilitates faster heat transfer but requires HTF-storage medium-structural material compatibility studies. Indirect contact systems employ heat exchangers or tube registers to transfer heat from the HTF to the storage medium without direct contact.

Effective heat storage materials should exhibit a combination of attributes: substantial gravimetric and volumetric storage capacity, long-lasting performance, non-toxic, non-flammable, and inert characteristics, resistance to material compatibility issues, compatibility with inexpensive structural materials, durability under repeated charging and discharging cycles, economic viability with ample availability, high thermal diffusivity and effusivity for efficient heat transfer, and minimal density variation with temperature to mitigate thermo-mechanical stresses(Bauer et al., 2012; Cabeza et al., 2022a; Gil et al., 2010; Gunasekara et al., 2021b).

The capacity of a heat storage system is determined by the volumetric and gravimetric energy densities of the materials used. In sensible heat storage systems, the volumetric heat capacity $\rho.c_p$ is the indicator of how much heat can be stored per unit volume of material. A high volumetric heat capacity reduces the required storage volume for a given heat capacity. The capacity of a sensible heat storage system is defined by Equation 2-1, where Q_s represents the stored heat (in Joules), m is the mass of the heat storage medium (in kg), c_p is the specific heat (in J/(kg·K)), T_i is the initial temperature (in °C), and T_f is the final temperature (in °C). Thermal diffusivity (α) and thermal effusivity (b) are two other key parameters, defined by Equations 2-2 and 2-3 respectively.

The thermal diffusivity, where k is the thermal conductivity (in W/m·K) and ρ is the density, is a measure of how quickly a material responds to changes in temperature. A material with high thermal diffusivity allows for rapid charging and discharging of the heat storage system.

$$Q_{\mathrm{s}} = \int_{T_{\mathrm{l}}}^{T_{\mathrm{f}}} mc_{\mathrm{p}} \mathrm{d}t = mc_{\mathrm{p}}(T_{\mathrm{f}} - T_{\mathrm{i}}) \tag{2-1}$$

$$\alpha = \frac{k}{\rho . c_p} \tag{2-2}$$

$$b = \sqrt{k . \rho . c_p} \tag{2-3}$$

On the other hand, thermal effusivity defines how the temperature at the surface of the material reacts to a heat flux exchange. The next section will focus on cementitious thermal energy storage (TES) materials, which have gained prominence due to their widespread availability, ease of fabrication, and potentially high energy storage density.

2.2 Role of Cementitious Materials in TES

Having established the principles of sensible heat storage and the importance of thermal diffusivity and effusivity, cementitious thermal energy storage materials will be discussed. These materials, derived from cement, water, and aggregates, offer a promising avenue for cost-effective and sustainable TES solutions (Boquera et al., 2021a; Cabeza et al., 2022a; Lavagna et al., 2020a; Ndiaye et al., 2018; Wang et al., 2023a).

In particular, the integration of SHS with cementitious composites, such as concrete, brings numerous advantages, given the inherent properties of these materials including high thermal mass, broad availability, cost-effectiveness, and durability (Fernandez et al., 2010; Navarro et al., 2016d; Tatsidjodoung et al., 2013).

Concrete-based TES is a more efficient and economical option than other mechanical or chemical storage technologies due to its relatively low cost and high operating efficiency (Lavagna et al., 2020b) (Kuravi et al., 2013). Recent research highlights the use of concrete as a TES material, with notable progress and emerging trends.(Navarro et al., 2016d, 2016d; Novotny et al., 2022; Sarkar et al., 2024; Tatsidjodoung et al., 2013; Wang et al., 2023b).

In low-temperature applications, the utilization of concrete as a TES material has been extensively associated with its use in building envelopes, facilitated by the integration of phase change materials (PCMs) to augment latent heat storage. This methodology has gained considerable traction, particularly in regions such as China and Europe, which exhibit a prominent research output volume on this subject matter.(Boquera et al., 2021b).

Concrete SHS systems in building sector can be implemented in various forms, including hydronic Thermo-Active Building Systems (TABS), ventilated concrete slabs (VCS) (Chen et al., 2010) (Fraisse et al., 2007), and integrated with double-skin facades (DSF). These systems offer several advantages, including improved thermal comfort, reduced energy consumption, and enhanced building sustainability. TABS allows the building's structure to serve as a thermal storage, enabling the utilization of renewable energy sources (Lehmann et al., 2007) (Chen et al., 2010). Double Skin Facades (DSF) have emerged as a defining feature of contemporary architecture, primarily owing to their

aesthetic appeal and their significant contribution to natural daylighting (Shameri et al., 2011) (Navarro et al., 2016b) (Fallahi et al., 2010).

In addition to building and renewable energy applications, SHS systems using cementitious composites also find substantial use in the management of industrial waste heat. Modern research is investigating the potential of storing waste heat recovered during industrial processes, a move that could contribute to energy efficiency and sustainability (Brückner et al., 2015b; Laing et al., 2008; Miró et al., 2016b).

Further, a noticeable shift towards high temperature thermal energy storage in concrete, particularly for concentrating solar power (CSP) plants, has been recognized. Thermal energy storage in CSP plants improves dispatchability, can provide buffering, delivery period displacement or extension, and improve the annual capacity factor of a CSP plant (Kuravi et al., 2013). This trend, highlighting the need to store and utilize high-temperature energy, marks an exciting research direction in the context of energy-efficient design and renewable energy systems based on concrete (Wang et al., 2023b).

Concrete based TES using ordinary Portland cement has found its role in CSP sector, as evidenced by a growing body of research and development efforts (Beine et al., 1989; Buscemi et al., 2018; Hoivik et al., 2019; Laing et al., 2012, 2006; Martins et al., 2015; Salomoni et al., 2014). Salomoni et al. (Salomoni et al., 2014) and Laing et al. (Laing et al., 2006) assessed the thermal sizing of the concrete based storage modules and their integration within a CSP system. Another study states that a 50 MW parabolic trough power plant with 1100-MWh concrete storage can deliver about 3500 full load hours annually in southern Europe, with about 30% of electricity generated by the storage system (Laing et al., 2012). The TES system has shown no changes in thermal performance after two years of operation. No cracking or separation has been observed between the storage material and steel pipes. The Concrete TES system has been tested at temperatures up to 380 °C for over 20 months (Hoivik et al., 2019). Buscemi et al. proposed the integration of solar energy in conjunction with TES for a pasta factory (Buscemi et al., 2018), demonstrating a substantial storage capacity of approximately 85 MWh_{th}. It exhibited a yearly storage efficiency of roughly 87%.

The initial investment costs for constructing and installing the proposed solar industrial process heating plant amounted to approximately 2 million euros, with a simple

payback time of 8 years. At an estimated material cost of less than 50 euros per ton in 2018, it is an economically viable choice for such applications even without government incentives. Concrete among other solid based materials like metals, rocks, minerals, and castable materials exhibits energy storage capabilities, displaying a volume-specific capacity of 69.8 kWh/m³ and a mass-specific capacity of 25.4 kWh/ton at a 100 K temperature difference. When evaluating the economic aspect of concrete as a TES material, the estimated capacity-specific material costs are remarkably low. In the year 2022, these costs are approximately 2.0 euros per kWh.(Steinmann, 2022). This efficiency, coupled with its economical characteristics, enhances concrete's suitability for thermal energy storage across various applications. Similarly, the material under consideration demonstrates remarkable storage capacity, holding an average of 106 kJ/kg. It further excels in volume-specific energy storage, managing up to 233 MJ/m³ or 65 kWh/m³. Materials with lower costs and adequate thermal storage capacities, such as concrete, could be increasingly favored in the development of TES systems.

A number of pilot-scale installations have been implemented by various innovators in recent years, signaling the technology's budding potential and the industry's growing interest in its deployment (Hoivik et al., 2017; “Kraftblock,” n.d.; “STORWORKS POWER,” n.d.; Novotny et al., 2022; Saeed et al., 2022). TES systems that utilize concrete as the medium for SHS are typically constructed by embedding a tube matrix register heat exchanger in the concrete, enabling the transfer of thermal energy to or from heat transfer fluids such as water, steam, molten salt, air, and synthetic oil.

The potential of cementitious materials is not confined merely to solar energy, though. They are also being tested for other medium and high-temperature applications, including industrial process heat and bulk electrical energy storage, a concept called Carnot battery (Dumont et al., 2020; Novotny et al., 2022). A Carnot battery is an energy storage system that converts electricity into thermal energy and later reconverts it into electricity. It offers potential cost advantages for large-scale (gigawatt-hour scale) storage compared to lithium-ion batteries. This technology is regarded as a promising option for economically and environmentally friendly storage of electricity from renewable energy sources, surpassing conventional battery solutions.

At commercial level, EnergyNest (Bergan and Greiner, 2014) utilizes high temperature concrete modules with a temperature limit of up to 380 °C. Storworks power ("STORWORKS POWER," n.d.) offers BolderBloc high temperature concrete modules that can handle temperatures up to 600 °C. Their system has a thermal capacity starting from 30 MWh and they have a demo unit of 200 kWh with construction underway for a 10 MWh capacity. Kraftblock ("Kraftblock," n.d.) employs high temperature concrete granules capable of withstanding temperatures up to 1300 °C. Their system is scalable from 4 MWh with a current capacity of 70 MWh. Concrete-based TES systems can also be used in steam generation (Singh and Sørensen, 2017) and the integration of high temperature TES into combined-heat-and-power (CHP) plants is viable as well (Gong and Ottermo, 2022).

However, Concrete thermal conductivity and specific heat vary based on concrete mix design and temperature (Lavagna et al., 2020b; Wang et al., 2023b). Optimizing these properties for TES is challenging due to variability in concrete mix designs and interactions between different constituents. Concrete used in TES needs to withstand cyclic temperature demands without thermal fatigue or degradation. Heterogeneous concrete composition can affect overall performance. Concrete has low storage density and long-term seasonal storage is challenging due to heat losses over time (Ndiaye et al., 2018).

Permanent microstructure changes can also occur at high temperatures. Ordinary Portland cement (OPC) concrete has long been the cornerstone of concrete-based TES systems (Wang et al., 2023b). The hydration process of OPC is a chemical reaction that occurs when water is added to the cement. This process transforms the cement from a plastic state to a solid state and is influenced by various parameters such as the water-cement ratio, use of admixtures, curing, and cement type. The main hydration products of OPC in Cement chemist notation (CCN) are calcium silicate hydrate (C-S-H) [1], calcium hydroxide (CH), and calcium aluminate hydrate (C-A-H) which contribute to the strength and durability of concrete ("The hydration of Portland cement," 1978; Scrivener et al., 2015). However, there are concerns about the effects of high temperatures on concrete,

[1] C=CaO (Calcium oxide, or lime); S=SiO_2 (Silicon dioxide, or silica); H= H_2O (Water); A= Al_2O_3 (Aluminum oxide, or alumina); $= SO_3 (Sulfur trioxide); N= Na_2O (Sodium oxide)

including decomposition of CH and degeneration of C-S-H (Andic et al., 2008; John et al., 2010) at temperatures beyond 300 °C (Rivera et al., 2016).

Apart from OPCs, there are other binder families. Calcium sulfoaluminate (C$A) cements with ability to store heat at relatively low temperatures (<100°C) (Ndiaye et al., 2020, 2018). C$A cements can produce much higher amounts of ettringite (40-80%) compared to Portland cements (a few percent). Ettringite is the key mineral that enables thermal energy storage through dehydration/rehydration reactions. Also, prototypes using C$A concrete for ettringite-based thermal storage have shown favorable performance - up to 71% storage efficiency and 117 kWh/m3 density in lab tests (Ndiaye et al., 2020).

Belite cement, also known as low-energy cement, is a type of cement that can be used as an ecological alternative to OPC. It is produced with less energy and has a lower environmental impact due to its lower limestone requirement and lower kiln temperatures, which result in lower CO_2 emissions and energy consumption (Cuesta et al., 2021; Guerrero et al., 2005). Belite cement has some advantages such as high durability and good late strength development (Cuesta et al., 2021; Irico et al., 2022). However, its utilization for TES applications in literature remains unexplored.

Calcium aluminate (CA) materials are other candidates for high-temperature TES applications, particularly in CSP plants and solar process heat systems (Alonso et al., 2016; Cabeza et al., 2022a). Their high enthalpy and storage capacity, heat resistance, versatility, and relatively low cost make them attractive alternatives to conventional OPC materials. However, CA materials also face challenges in long-term stability and capacity retention under repeated thermal cycling. Corrosion and deterioration of concrete-based CA systems and a decrease in heat storage capacity upon cycling (Cabeza et al., 2022a; Ings and Brown, 1982) are major concerns that need to be addressed through further research and material optimization.

Geopolymer-based concrete is considered sustainable alternative binder to OPC due to its lower environmental impact and ability to utilize industrial byproducts (Barzegar et al., 2024; Duxson et al., 2007; Palomo et al., 1999; Provis et al., 2005).. It is produced by the alkaline activation of aluminosilicate materials like fly ash or slag (Singh et al., 2015). Geopolymer concrete, a mixture of fly ash and silica fume, exhibits a significantly lower global warming potential compared to traditional concrete, with reductions of up to

75-78%. Additionally, geopolymer concrete is generally 10-18% less expensive than traditional concrete with silica fume (Bajpai et al., 2020). GEO shows off notable early compressive strength, reaching a staggering 80 MPa, comparable or even superior splitting tensile and flexural strengths, and a denser interfacial transition zone fostering enhanced strength. It has lower elastic modulus, around 15-29% less than OPC. Moreover, it displays reduced drying shrinkage, around 0.025% after 12 weeks, and exhibits superior sulphate and acid resistance compared to OPC systems. This material proves its mettle in high-temperature environments, exhibiting residual strength after heating to 800°C, and demonstrating resistance to spalling up to 850°C (Singh et al., 2015).

In summary, geopolymer concrete possesses very good mechanical properties and durability compared to OPC, with additional advantages in terms of sustainability and high temperature resistance (Rivera et al., 2016; He et al., 2020). Geopolymers have an open, highly porous structure that allows pressure release and escape of steam generated during heating. In contrast, OPC has a dense microstructure that traps steam, leading to explosive spalling.

Geopolymers are composed of amorphous aluminosilicate gel and thermally stable aggregates. Upon heating, minimal dehydration or phase changes occur. On the other hand, OPC degrades above 300°C as key hydrates like C-S-H, CH, and ettringite decompose (Rivera et al., 2016). Geopolymers have good thermal stability compared to OPC (He et al., 2020). The presence of a significant amount of nanoconfined water within geopolymer composites is a notable characteristic that contributes to their high yet stable heat capacity. This higher proportion of water molecules in geopolymers compared to OPC is evident from the molar contents of their primary constituents: $C_{1.7}SH_{1.8}$ (Allen et al., 2007) and $N_{2.5}S_{3.5}A_2H_6$ (Lolli et al., 2018) with 1.8 moles of water for OPC, and 6 moles of water for geopolymers. They exhibit low mass loss, thermal expansion, and thermal conductivity when exposed to high temperatures (He et al., 2020). However, there are still few reports that GEO has been studied and proposed as TES material (Ferone et al., 2014; Frattini et al., 2021).

This thesis focuses on investigating GEO as a potential substitute for OPC, with its capacity to operate over a broader temperature range and higher storage capabilities as per Equation 2-1. The ensuing sections delve into the preparation of GEO samples, the assessment of their thermal properties, the fabrication and implementation of various scenarios involving GEO and OPC-based materials, and the development of two-dimensional and three-dimensional numerical models that simulate and compare GEO to OPC TES (thermal energy storage) units. However, before embarking on these tasks, a thorough examination of the heat equation and its significance to this study is warranted. As TES systems that employ cementitious materials necessitate a firm grasp of the heat equation in solids for effective modeling and simulation.

2.3 Heat Transfer Fundamentals in Solids

The previous sections explored the concept of thermal energy storage (TES) and introduced the potential of geopolymeric (GEO) materials as alternative TES materials to ordinary Portland cement (OPC). To fully comprehend the behavior of TES systems, a fundamental understanding of the governing heat transfer principles is essential. This section delves into the heat equation in solids, the primary mathematical framework that describes the transient and steady-state heat conduction processes within a solid material.

The study of heat transfer began in the early 1700s with the work of Gabriel Fahrenheit, who invented the mercury thermometer and standardized the temperature scale. In 1752, Abbé Nollet observed osmosis across animal membranes, which suggested that heat could transfer through materials even if they were not in contact. In the same year, Daniel Bernoulli showed that trigonometric series could be used to solve differential equations. This was an important base development for later existence of heat equation, which is a partial differential equation. In 1760, Joseph Black recognized the existence of latent heat and specific heat, two important concepts in heat transfer.

In 1779, Adair Crawford correlated the respiration of animals with their body heat, suggesting that heat was generated by metabolic processes. In 1783, Antoine Lavoisier, Marie Anne Pierrette and Pierre-Simon Laplace invented the first calorimeter, which allowed them to measure heat capacity and latent heat. In 1789, Laplace formulated the Laplace operator, which is used in the heat equation. In 1804, Jean-Baptiste Biot studied heat conduction among discontinuous bodies. In 1807, Joseph Fourier formulated the partial differential equation for heat conduction in solids. This equation is now known as the heat equation.

Fourier's heat conduction equation describes how heat diffuses through a solid over time. It was first formulated by Joseph Fourier in 1807 and published in 1822 (Narasimhan, 1999). Over 200 years later, Fourier's heat equation and Fourier's law continue to underpin the analysis of heat conduction and diffusive processes in solids and other media. The equation is based on Fourier's law, which states that the rate of heat conduction is proportional to the negative temperature gradient. Physically, it describes the conservation of heat energy over an infinitesimal volume element.

The heat equation in solids is derived from the energy balance equation, Fourier's law of heat conduction, and appropriate constitutive relations (Hahn and Özisik, 2012; Ozisik, 2013). The transient heat conduction equation of Fourier, a parabolic partial differential equation, captures the temporal evolution of temperature distribution within a solid material. It can be represented mathematically as Equation 2-4, where k, T, c_p, and t represent thermal conductivity, temperature, specific heat capacity, and time, respectively. T acts as a scalar potential, while k and c_p are empirical parameters.:

$$\nabla \cdot k\nabla T = c_p \frac{\partial T}{\partial t} \tag{2-4}$$

Heat exchange with the external environment is governed by boundary conditions, either prescribing the temperature or thermal fluxes at the boundaries. The initial temperature distribution at time t = 0 is also specified.

In the special case where the temperature remains constant with time and k is independent of temperature, Equation 2-4 simplifies to Laplace's equation, a fundamental equation in physics governing potential fields.

Heat transfer occurs through the mechanisms of conduction, convection, and radiation. While heat itself cannot be directly measured, its concept holds physical significance due to its direct correlation with temperature. Conduction is a specific mode of heat transfer characterized by the transfer of energy within solids or quiescent fluids (lacking macroscopic movement).

Once the temperature distribution, $T(\hat{r}, t)$, within the medium is known as a function of both spatial position (defined by the position vector ˆr) and time (represented by scalar t), the flow of heat can be determined from the governing heat transfer principles.

In Cartesian coordinate system, Fourier's law is applicable to a homogeneous and isotropic solid, characterized by a material with thermal conductivity that remains consistent regardless of direction. This relationship is expressed through equation 2-5, where ˆi, ˆj, and ˆk represent the unit direction vectors corresponding to the x, y, and z axes, respectively.

$$\overrightarrow{q''}(x,y,z,t) = -k\frac{\partial T}{\partial x}\hat{\imath} - k\frac{\partial T}{\partial y}\hat{\jmath} - k\frac{\partial T}{\partial z}\hat{k} \tag{2-5}$$

Beyond the heat flux, $\overrightarrow{q''}$, which represents the rate of heat power transfer across a unit area perpendicular to the direction of flow, the total heat flow, also known as the heat rate, *q*, is another crucial metric, determined by multiplying the heat flux by the total cross-sectional area over which heat transfer occurs. For three-dimensional (3D) problems, this can be achieved by integrating over the flow area. The heat rate in the x-direction for three-dimensional Cartesian problems is provided by Equation 2-6.

$$q_{cond,x} = -k\int_{y=0}^{L}\int_{z=0}^{H}\frac{\partial T(x,y,z)}{\partial x}dzdy \tag{2-6}$$

For the three-dimensional problem, Equation (2-6), the total cross-sectional area is defined by the surface extending from y = 0 to L in the second spatial dimension and from z = 0 to H in the third spatial dimension. This implies that the temperature distribution, T, is a function of all three spatial coordinates: x, y, and z.

The governing differential equation for heat conduction, as stated by Equation (2-4), necessitates two boundary conditions for each spatial dimension, along with one initial condition for non-steady-state problems.

The initial condition establishes the temperature distribution within the medium at the onset of the time-dependent process, represented by T(ˆr, t = 0). Boundary conditions, on the other hand, delineate the temperature or heat flux at the perimeter of the region under consideration. For instance, at a specific boundary surface, the temperature distribution may be specified, or the heat flux distribution may be prescribed.

Additionally, heat exchange by convection and/or radiation with a surrounding environment at a given temperature may occur. Boundary conditions are derived by establishing an energy balance equation at the surface of the solid. Before delving into formal boundary conditions, it is advantageous to define two supplementary laws governing heat transfer: radiation and convection heat transfer.

The Stefan-Boltzmann law relates the radiant energy emitted by a surface to its temperature and emissivity. The total emissivity, ε, is calculated by integrating the spectral emissivity over all wavelengths and directions. For non-gray surfaces, ε varies with temperature due to the Planck distribution. The net radiant heat flux between a surface and an ambient medium can be approximated using Equation (2-7), which assumes an ideal enclosure and a gray body surface. σ denotes the Stefan–Boltzmann constant, having a value of $\sigma = 5.670 \times 10{-}8$ W/(m²·K⁴) and T_∞ is the temperature of the ambient.

$$q''_{\text{rad}} = \varepsilon\sigma(T^4 - T_\infty^4) \tag{2-7}$$

Newton's law of cooling, Equation 2-8, relates the heat flux exchanged between a surface and its surroundings by convection to the temperature difference between the surface and the ambient environment, T_∞. The convection heat transfer coefficient, h [W/(m^2 · K).], quantifies the efficiency of heat transfer between the surface and the ambient.

$$q''_{\text{conv}} = h(T - T_\infty) \tag{2-8}$$

There are three primary types of boundary conditions in heat transfer:

1. Prescribed Temperature Boundary Condition (Dirichlet): Specifies a constant temperature at the boundary surface, Equation 2-9.
2. Prescribed Heat Flux Boundary Condition (Neumann): Defines a constant heat flux across the boundary surface, Equation 2-10.
3. Convection Boundary Condition: Describes heat transfer due to both conduction and convection. It is derived from the general heat transfer equation of Equation 2-9, by setting the radiation term to zero, see Equation 2-11.

Other boundary conditions include interface boundary conditions, which arise at the interface between different materials with distinct thermal properties, and symmetry boundary conditions, Equation 2-12, which are used when only one-half of the problem needs to be analyzed. Symmetry boundary conditions treat the line of symmetry as an adiabatic (perfectly insulated) surface. A symmetry boundary condition defines a mirror face/surface where the physical geometry and expected flow/heat transfer pattern are mirrored along that surface. It reduces the model size and computational requirements by modeling only half or a portion of the full geometry.

$$T|_{\text{surface}} = T_0 \tag{2-9}$$

$$-k\frac{\partial T}{\partial n}\Big|_{\text{surface}} = q_0'' \tag{2-10}$$

$$-k\frac{\partial T}{\partial n}\Big|_{\text{surface}} = h[T|_{\text{surface}} - T_\infty] \tag{2-11}$$

$$\frac{\partial T}{\partial n}\Big|_{\text{boundary}} = 0 \text{ (symmetry condition)} \tag{2-12}$$

Lumped system formulation or lumped capacitance method is a simplification of transient heat conduction analysis. It neglects spatial variation of temperature and considers temperature as a function of time only. In partial lumped analysis, the temperature variation is preserved in one of the space variables but lumped in the others. It is restricted to applications where the spatial variation of temperature is small or negligible.

Solving heat transfer problems requires a variety of techniques, each suited to specific scenarios. Between the main techniques it can be found:

The Separation of Variables Method (SVM) excels at handling linear homogeneous heat equations and their corresponding boundary and initial conditions. It involves decoupling the variables in the partial differential equation (PDE) and solving the resulting ordinary differential equations (ODEs) , which can often be solved analytically . It involves

assuming that the solution can be expressed as a product of functions, each of which depends only on a single variable. The method is particularly useful for problems with homogeneous boundary conditions, which means that the boundary values are independent of time or space. In such cases, the ODEs can be solved to obtain eigenfunctions and eigenvalues. These can then be used to construct the general solution of the PDE. The analytical solutions to different basic geometries are discussed in great detail, for example in (Hahn and Özisik, 2012).

Duhamel's Theorem proves useful when the boundary or initial conditions exhibit nonhomogeneous functions of time. It transforms the nonhomogeneous problem into a set of simpler problems, allowing the solution to be constructed using a convolution integral over past history.

The Green's Function Method effectively tackles problems with nonhomogeneous terms. It represents the effect of a delta function source and boundary conditions, enabling straightforward superposition for multiple sources.

The Laplace Transform Method effectively simplifies PDEs and their associated conditions by transforming them into the frequency domain, where they become algebraic equations. The solution can then be inverted back to the time domain.

The Integral Transform Technique, on the other hand, transforms the PDE into an integro-differential equation, with the eigenfunctions of the transform serving as basis functions (Hahn and Özisik, 2012; Ozisik, 2013).

For complex geometries and big systems, numerical techniques such as finite differences, finite elements, and boundary elements are commonly employed (Liu and Quek, 2014a; Özişik et al., 2017). In TES systems, the heat equation is employed to describe how heat is stored or retrieved within the TES material. For instance, when heat is injected into a TES system, the heat equation predicts the temperature distribution within the material as it absorbs and stores the energy. Conversely, when heat is extracted, the equation models how the temperature distribution evolves as the stored energy is released.

The heat equation provides a fundamental mathematical framework for understanding and modeling heat transfer processes in TES systems. In numerical modelling of GEO as TES material, the Finite Element Method (FEM) is employed to develop a numerical model. FEM is a numerical technique that discretizes complex geometries into smaller elements, enabling the solution of partial differential equations governing heat transfer. By incorporating the thermophysical properties of geopolymer concrete and the boundary conditions of the TES unit, the FEM model can predict temperature distribution, heat storage and retrieval rates, and thermal performance under various operating conditions.

In the next section, 2.4, in introduction of how to use of the Finite Element Method (FEM) to develop a Numerical Model of Geopolymer concrete will be presented. In Chapter IV, before doing 3D Multiphysics simulations, discussion on numerical methods for solving heat conduction problems will be presented, including finite differences, finite elements, and boundary elements.

2.4 The Potential of Geopolymer as a TES Material

The previous sections established the significance of geopolymer (GEO) materials as potential alternatives to ordinary Portland cement (OPC) in thermal energy storage (TES) systems. To validate this proposition, this section delves into the development of a numerical model based on the finite element method (FEM) to simulate and compare the thermal performance of GEO and OPC-based TES units.

Prior to constructing the numerical model, it is essential to characterize the thermophysical properties of the GEO and OPC materials. These properties, including thermal diffusivity and specific heat capacity play a central role in determining the heat transfer behavior of the TES system as discussed with Equations 2-2 and 2-3.

Building upon the material characterization data, a two-dimensional (2D) FEM model is developed to simulate heat transfer phenomena within GEO and OPC TES units. The model incorporates the thermophysical properties of the respective materials and boundary conditions representing the specific TES configuration. By simulating the heat storage and retrieval processes in the GEO and OPC TES units, the model enables a direct comparison of their thermal performance.

2.4.1 Material preparation

Geopolymer hybrid cement (H-Cement) is composed of fly ash, granulated blast furnace slag, highly alkaline wastewater from red mud ponds, and up to 20% Portland cement clinker. Compared to OPC, H-Cement production emits up to 80% less CO_2. It does not require heat treatment or autoclaving during production. It can be used similarly to regular cement for ready-mixed concrete applications. Industrially produced geopolymer hybrid cement containing 20% Portland cement clinker and 80% inorganic geopolymer from Považská Cementáreň was used as binder (Martauz et al., 2016).

To prepare GEO concrete, w/c = 0.6 and 75%wt of steel slag aggregate were employed. Geopolymer helps to maintain a stable and high heat capacity over different temperature ranges and slag maintains a proper thermal conductivity. Aggregates were crushed into fine powder (grain size < 0.25 mm). Therefore, powders were mixed using a mechanical blender at low speed (350 rpm) for 1 minute to obtain a uniform dispersion of

siliceous aggregates in the hybrid cement powder. Pure water was added, and the solution was stirred at 750 rpm for 1 min and 30 seconds. Later, the solution was allowed to rest for 1 minute and mixed again at 750 rpm for 1 min and 30 seconds. Mixes were cast in cylindrical silicone molds with d = 4 cm and sealed. After 24 hours, the specimens were removed from the molds and placed in an environmental chamber with 100% relative humidity at room temperature for 28 days.

2.4.2 Material characterization

Specific heat capacity of the sample was measured by differential scanning calorimetry (DSC) (Q2000TA Instrument). The experiment was conducted with a modulated method (MDSC); this technique provides information on both reversible and non-reversible thermal events. Consequently, MDSC allows signals coming from water evaporation (irreversible process) to be neglected and provides the real specific heat of the sample. Aluminum pans were used in the experiment and the sample weight was about 30 mg. Experiment was performed on heating between 100 and 400 °C with a heating rate of 3 °C/min and modulated with ± 0.48 °C every 60 s.

The main part of this work is the comparison of the GEO sample with other cement-based materials. So, for the right evaluation of material efficiency, it is necessary to have a proper characterization of thermal diffusivity. However, depending on the material and the sample preparation, relevant deviations can be observed on the thermal diffusivity measured by different techniques (Ricklefs et al., 2017; Streb et al., 2018). Therefore, first, a reference pellet of hydrated OPC was measured by laser flash analysis (LFA), and the results were normalized to the literature values. Later, thermal diffusivity values of the GEO sample were multiplied by the normalization factor. Sample powders (size grain < 64 μm) were compressed by a manual hydraulic press (SPE-CAC) applying 7 tons for 5 min. The pellet with a thickness of ~2 mm was investigated by LFA 457 Micro flash.

Measurements were made at room temperature, 50, 100, 200, 300, 400, 500, 600, 700, 800 and 900 °C. The heating rate was ten °C/min. Five laser shots were performed for each temperature. Intervals between shots were 1.5 min to allow the homogenization of the temperature of the samples.

The MDSC-measured values of specific heat capacity for GEO represent a consistent behavior versus temperature rise. For the selected OPC concrete counterparts, DLR (Laing et al., 2012) and HEATCRETE (Hoivik et al., 2019), in the current state of knowledge, there is a lack of data regarding the thermal properties of OPC beyond 400°C.

In fact, OPC-based concretes degrade at temperatures above 400–450°C. To facilitate a comparative analysis of GEO with other materials at temperatures ranging from 400°C to 700°C, two fictitious OPC types, OPC-1, and OPC-2, were introduced. The thermal properties of OPC-1 and OPC-2 were approximated by extrapolating the available data from HEATCRETE and DLR, respectively (see table 2-1). Data for other samples, DLR (Laing et al., 2012) and Heatcrete (Hoivik et al., 2019) show an increasing trend with temperature rise (Figure 2-2).

Measured α values for GEO show a more stable trend versus temperature compared to OPC-1 and OPC-2 (Figure 2-2). The thermal diffusivity (α) describes the rate of temperature spread through a material and is for characterizing unsteady heat conduction behavior. In fact, for temperatures more than 400 °C, the GEO concrete is expected to have higher thermal diffusivity than OPC-1 and OPC-2. Values for thermal conductivity, specific heat capacity and density of samples are tabulated in Table 2-1. For temperatures T > 400 °C, extrapolated values of DLR and Heatcrete concretes are used.

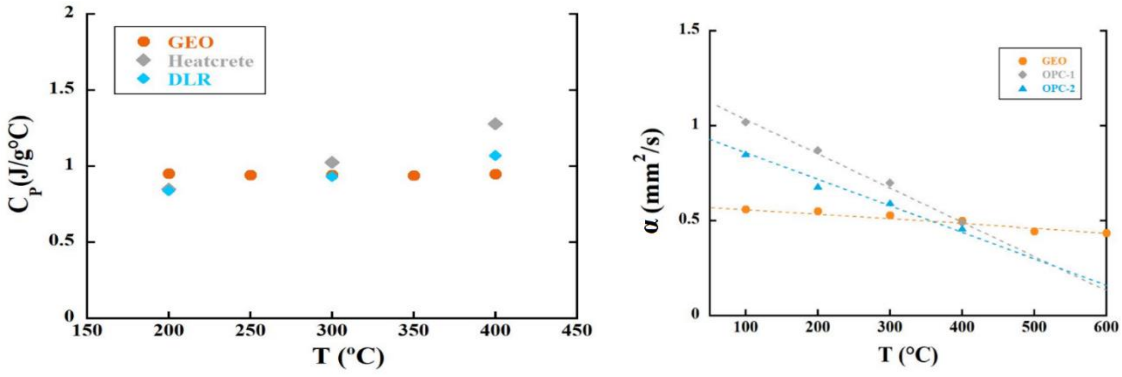

(A) (B)

Figure 2-2. Specific heat capacity and thermal diffusivity measurement.

(A) Measured specific heat of the GEO concrete, compared to other leading samples DLR and Heatcrete, and (B) Measured thermal diffusivity of the GEO concrete, compared to defined samples OPC-1 and OPC-2. The dashed lines are guides to the eye to notice the trends.

The thermal conductivity, specific heat capacity, and density of the GEO sample are presented in Table 2-1. Properties obtained for OPC-2 are based on DLR data (Laing et al., 2012), while reference formulas have been utilized for temperatures exceeding 400 °C. For OPC-1, curve-fitting was employed for temperatures up to 400 °C using HEATCRETE data (Hoivik et al., 2019), followed by extrapolation for higher temperatures. R-squared (R^2) values exceeding 0.9 were prioritized, necessitating linear extrapolation for c_p and exponential estimation for k and ρ.

Table 2-1. Thermophysical properties of different samples.

material	Properties	Equation Fitted
GEO	C_p[1]	1000
	K[2]	1.2
	ρ[3]	2400
OPC-1	C_p	$\begin{cases} 0.004521 \times T\text{^}2 + (-0.6148 \times T) + 802.5 \rightarrow if\ T \leq 400 \\ 1.05 \times T + 860 \rightarrow if\ T > 400 \end{cases}$
	K	$(5.081e+54) \times exp(-((T-(-1.963e+05))/(1.757e+04))\text{^}2$
	ρ	$71.4 \times exp\big((-0.004057) \times T\big) + 2240 \times exp\big((5.283e-07) \times T\big)$
OPC-2	C_p	$(0.7 + 8.75 \times 10\text{^}(-4) \times T) \times 1000$
	K	$1.467 - 6.667 \times 10\text{^}(-4) \times T$
	ρ	2250

[1] Specific heat capacity (W.s/kg. °C). [2] Thermal conductivity (W/m. °C). [3] Density (kg/m^3). T is temperature (°C).

2.4.3 Numerical Model (2D)

A finite element analysis (FEA) model of the TES module was developed using MATLAB (MATLAB, 2020), employing the experimentally determined thermal properties. The geometry used for the numerical analysis was a square cubic block of concrete with an embedded tube. Block sizes were 100 × 100 × 100 mm^3 and the tube diameter was 25.4 mm. This layout with larger scale and more tubes is by far the best-known and most widely used scheme, Figure 2-3 (A).

The front face of the block was considered for numerical modeling (2D) and thermal analysis. However, to calculate the energy storage amount, which is a quantity dependent on mass and volume, outputs of the two-dimensional model were used and generalized to the module's volume and mass.

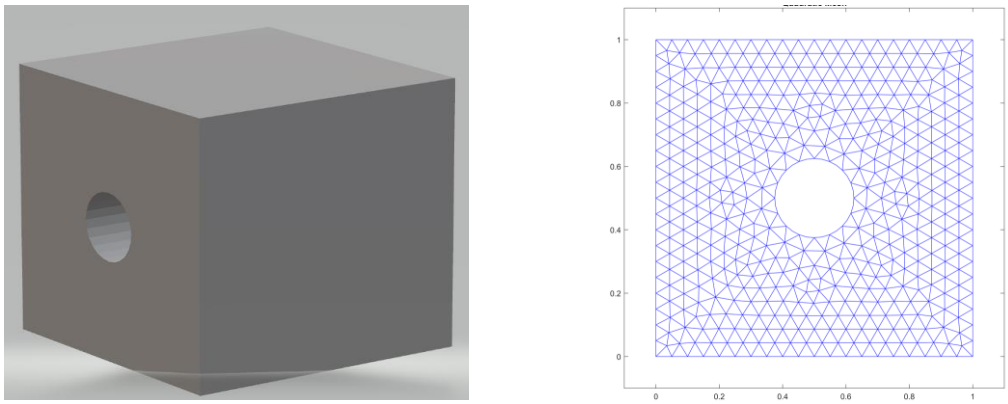

(A) (B)

Figure 2-3. Concrete block with model meshed geometry.

(A) Perspective view of geometry; module is 100 × 100 × 100 mm3 volume with an embedded 25.4 mm (1") tube. (B) Quadratic triangular mesh used for finite element modeling (FEM) (scale 1:100, dimensions in mm).

Transient heat transfer analysis can be performed using the finite element method , solving the heat diffusion equation, Equation 2-5, with time-dependent terms. The transient heat equation in 2D Cartesian coordinates is presented in Equation 2-13:

$$\frac{\partial T}{\partial t} = \alpha \left(\frac{\partial^2 T}{\partial x^2} + \frac{\partial^2 T}{\partial y^2} \right) \quad (2\text{-}13)$$

where α is thermal diffusivity, T is temperature, t is time. The FEM involves discretizing the domain of interest into a mesh of finite elements. Each element is assigned a temperature value, representing the average temperature within the element. Galerkin interpolation is a method for approximating the temperature distribution within each element.

By applying Galerkin FEM to derive discretized matrix equation as $[C]\{\dot{T}\} + [K]\{T\} = \{F\}$ where [C] is capacity matrix, [K] is conductivity matrix, {T} is nodal temperature vector, and {F} is load vector. It involves defining a set of basis functions that span the space of possible temperature variations within the element.

The heat equation is first converted into its weak formulation, which expresses the problem in terms of integrals over the domain of interest. This involves integrating the governing equation and its boundary conditions over each finite element. The weak formulation is then discretized using the weighted residual method (WRM), which approximates the integrals using the Galerkin interpolated temperature values. This leads to a set of algebraic equations that represent the discretized heat equation.

To simulate the transient heat transfer process, the system of algebraic equations obtained from the WRM is solved repeatedly over time steps. The initial temperature distribution is prescribed, and boundary conditions are applied at each time step.

The temperature value at a node is represented by the symbol T_i, where i is the index of the node. The average temperature within an element is represented by the symbol T_e, where e is the index of the element. The element assembly process involves solving the equation 2-14:

$$T_i = \sum_{e=1}^{N_e} w_{ie} T_e \tag{2-14}$$

where N_e is the total number of elements and w_{ie} is the weight associated with node i in element e. Later in Galerkin Interpolation, the temperature distribution within an element is approximated using the Equation 2-15:

$$T_e = \sum_{j=1}^{N_p} c_{ej} \phi_j \tag{2-15}$$

where $\mathbf{N_p}$ is the total number of basis functions, c_{ej} are the coefficients of the basis functions, and Φ_j are the basis functions. The weak formulation of the heat equation can be expressed as Equation 2-16:

$$\int_{\Omega} (k\nabla T \cdot \nabla v - qv) d\Omega = 0 \tag{2-16}$$

where Ω is the domain of interest v is a test function, and q is the heat source. The weighted residual method involves integrating the weak formulation over each finite element and approximating the integrals using the Galerkin interpolated temperature values. This leads to the following set of algebraic equations, Equation 2-17:

$$\int_{e} \left(k\nabla T_e \cdot \nabla \phi_j - q_e \phi_j\right) de = 0 \tag{2-17}$$

The time integration scheme involves solving the system of algebraic equations obtained from the WRM repeatedly over time steps. The implicit Euler method can be applied to the system of algebraic equations obtained from the WRM as shown in equation 2-18. Then, an implicit Euler method used, can be expressed as follows, Equation 2-19:

$$\int_{e} \left(k\nabla T_{e,n+1} \cdot \nabla \phi_j - q_{e,n+1} \phi_j\right) de = 0 \tag{2-18}$$

$$T_{i,n+1} = T_{i,n} + \Delta t\left(k\nabla T_{i,n+1} \cdot \nabla \phi_j - q_{i,n+1} \phi_j\right) \tag{2-19}$$

The implicit Euler method is a time integration scheme that assumes that the temperature distribution at the next time step ($T_{i,n+1}$) is known. This allows the system of algebraic equations to be solved for the temperature distribution at the current time step ($T_{i,n}$). The time step size (Δt) is typically chosen to be small enough to ensure that the assumption of a known temperature distribution at the next time step is valid. Once $T_{e,n+1}$

is known, the temperature distribution at the current time step ($T_{i,n}$) can be updated using the equation 2-20:

$$T_{i,n+1} = T_{i,n} + \Delta t \int_e \left(k \nabla T_{i,n+1} \cdot \nabla \phi_j - q_{i,n+1} \phi_j\right) de \tag{2-20}$$

This process is repeated for each time step until the desired solution is reached. The implicit Euler method is a simple and efficient time integration scheme that is commonly used for solving transient heat transfer problems. However, it can be unstable for problems with large time step sizes or sharp temperature gradients (Liu and Quek, 2014b).

The derivation of the transient, conduction-dominant heat transfer dynamics is based on a simplified model of a concrete block, with several assumptions made to facilitate the process. Firstly, it is assumed that there is no heat generation within the concrete block. This assumption is based on the premise that the block is not a source of heat but merely a medium to store thermal energy. Secondly, the heat distribution is assumed to be uniform along the length of the structure. This assumption is made under the condition that there is no dominant direction for heat transfer, thus necessitating a multi-dimensional approach to solve the conduction problem. Thirdly, radiation heat transfer is negligible. Lastly, the tube's wall thickness is assumed to be negligible, too, implying that its thermal resistance has a minimal impact on the heat transfer process. This assumption is practical when the tube wall is thin and has high thermal conductivity as metallic piping has.

Substituting the simplifying assumptions into the general transient heat equation, the resulting heat equation for the concrete block embedded in a heated tube (charging the storage medium) is presented as follows, Equation 2-21:

$$\frac{\partial}{\partial x}\left(k \frac{\partial T}{\partial x}\right) + \frac{\partial}{\partial y}\left(k \frac{\partial T}{\partial y}\right) = \rho c \frac{\partial T}{\partial t} \tag{2-21}$$

The equation is a partial differential equation that describes the distribution of heat (or variation in temperature) in the block over time.

Additionally, the boundary and initial conditions need to be defined. Initially, the TES is assumed to be at a uniform temperature, denoted by T_0. This condition reflects the fact that the TES is commonly charged or preheated to a specific temperature before being used.

On the tube side, the temperature is specified as T_{inlet}, indicating that the fluid flowing through the tube maintains a constant temperature. This boundary condition assumes that the fluid temperature does not significantly influence the heat transfer within the TES.

$$T\,(r=r_{out},\ \forall t) = T_{inlet}. \tag{2-22}$$

The insulated boundary condition represents the absence of heat transfer across the outer surface of the TES. This assumption is reasonable for well-insulated TES systems where heat loss is minimal or for a symmetric configuration. Specified heat flux - insulated boundary:

$$k\frac{\partial T(x=0,L,t)}{\partial x} = 0 \; and \; k\frac{\partial T(y=0,L,t)}{\partial y} = 0 \tag{2-23}$$

To simulate the temperature distribution in the TES module, a numerical scheme using quadratic triangular mesh was employed (Figure 2-3 (B)). The average temperature of all elements in the mesh region (denoted as "$T_{average}$") is a key parameter that depends on the initial and boundary conditions of the material, as well as its transient behavior.

It has been used in determining the charging/discharging time, estimating the amount of stored energy, and evaluating the transient heat distribution within the TES module. To ensure the validity of the results obtained from the numerical scheme, grid test analysis was performed on the mesh, see Appendix A.

Figure 2-4 depicts at which locations temperature values will be studied deeply, since they illustrate the rapid heat transfer from the heat source to the TES material, demonstrating the TES module's ability to store and release thermal energy efficiently.

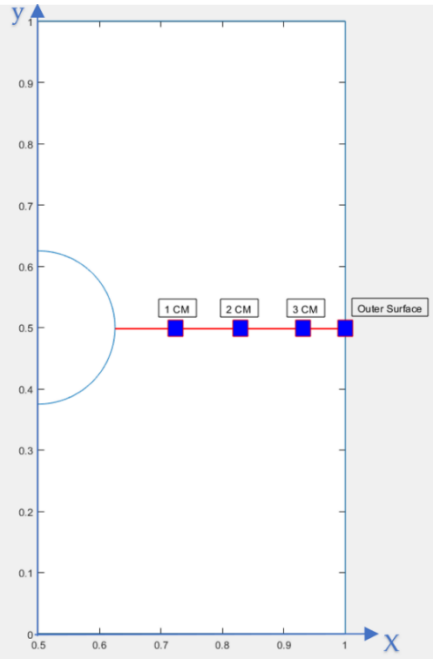

Figure 2-4. Temperature assessment points.

Points marked on the XY plane to monitor the temperature changes at specified distances from the tube wall, T1, T2, T3 and T4. (scale 1:100 mm).

2.4.4 Numerical Results

Initially, a low-temperature regime was considered, where T_{inlet} was set to 400°C and the initial temperature (T_0) of the storage modules was 250, 300, and 350°C, respectively. The $T_{average}$ of the modules was then calculated after 6 hours of heating. Among the tested modules, OPC-1 exhibits the highest $T_{average}$ after 6 hours. However, as the T_0 increases, the difference between the $T_{average}$ values of the TES modules diminishes (Table 2-2).

Table 2-2. Average temperature reached after 6 hours for T_{inlet} = 400 °C.

	T_0 = 250 °C	T_0 = 300 °C	T_0 = 350 °C
OPC-1	277.3	316.9	357.8
OPC-2	270.3	313.1	356.4
GEO	268.4	312.3	356.1

Subsequently, a high-temperature regime was imposed by of T_{inlet} = 700°C and a range of T_0 values from 250 to 650°C, with 50°C increments. The GEO module demonstrated superior performance for T_0 values greater than 350°C, attributed to its higher thermal diffusivity at elevated temperatures. This highlights the substantial impact of inlet and initial temperatures on the calculated average temperature of the GEO module. The results are summarized in Table 2-3.

Table 2-3. Average temperature reached after 6 hours for T_{inlet} = 700 °C.

	Initial temperatures °C								
	250	300	350	400	450	500	550	600	650
OPC-1	317.9	356.1	395.7	437	479.7	522.9	566.6	610.7	655.2
OPC-2	305.9	348.1	390.8	434	477.5	521.4	565.6	610.2	655.0
GEO	305.1	349.0	392.9	436	480.6	524.5	568.4	612.3	656.1

Stored thermal energy Q_s (kJ) after 6 hours of heating up the TES modules was calculated from Equation 2-1 for both low and high T_{inlet} conditions. As could be predicted from Tables 2-1 and 2-2, for T_{inlet} = 400 °C, the GEO module shows Q_s values close to those of the OPC-2 module, even though the values of Q_s are ~24% smaller than those of OPC-1 (Figure 2-5 (A)). Regarding the high temperature range (T_{inlet}=700 °C), an improvement in GEO results is observed; however, the amount of energy stored for GEO is still less than that for the OPC-1 sample (Figure 5B). As mentioned previously, the properties for OPC-1 and OPC-2 are extrapolated from concretes, and there is no evidence that these specimens can operate in this temperature range.

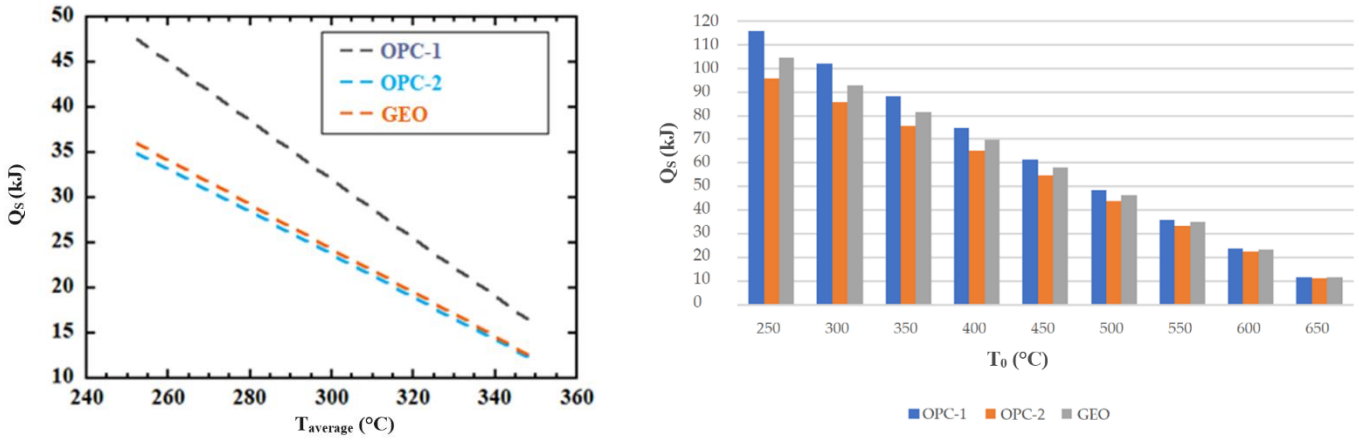

Figure 2-5. Stored thermal energy Qs (kJ) after 6 hours of heating.

(A) Energy stored (kJ) for T_{inlet}=400 °C, charging for 6 hours and different initial temperatures. **(B)** Energy stored (kJ) for T_{inlet} = 700 °C, charging for 6 hours and different initial temperatures.

To simulate the charge and discharge scenarios, T_{inlet} was considered as a stepwise approach of distinct stages. In this way, $T_{inlet} = T_{max}$ for the charging process and $T_{inlet} = T_{min}$ for the discharge process. T_{max} and T_{min} are operating temperature scenarios.

Each complete charge/discharge cycle is assumed to last 12 hours. Modeling was conducted with temperature data of two solar power plants currently operating. The first is the 1.0 MWh EnergyNest storage pilot at the Masdar Institute Solar Platform (MISP) in Abu Dhabi, United Arab Emirates (Hoivik et al., 2019), operating between 290 and 390 °C with thermo-oil as heat transfer fluid.

The second is the Solar Two power tower pilot in California, USA (Tyner et al., 1995), along with GEMASOLAR in Seville, Spain (Burgaleta et al., 2011), with molten salt as heat transfer fluid. T_0 = 290 °C and T_{inlet} = 565 °C were studied. Afterward, a high temperature regime (T_0 = 290ºC; T_{inlet} =700 °C) was considered to evaluate the GEO module's behavior at high temperature ranges.

Case 1: T_0 = 290ºC; T_{inlet} =565/290 °C Assuming that OPC-based samples are able to operate in this temperature range, in Figure 2-6 (A), the calculated $T_{average}$ of the TES modules is shown. An attempt has been made to estimate the time required for initial setup and reaching the inlet temperature, T_{inlet} = 565 °C. After about 280 hours, $T_{average}$ was compared for different modules (Figure 6B). OPC-1 module obtained the highest average temperature, followed by GEO and then OPC-2.

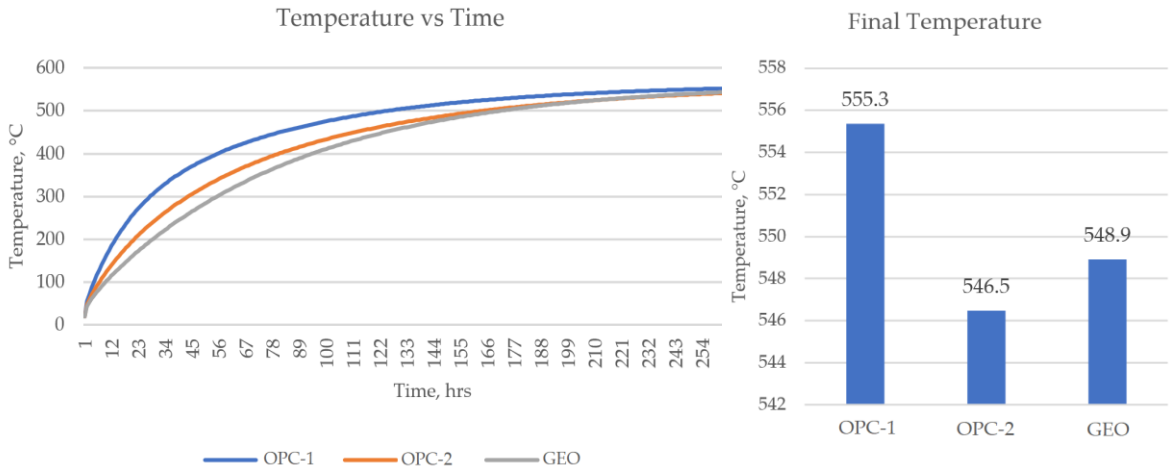

(A) (B)

Figure 2-6. Average temperature estimation for TES units (T_0 = 290ºC; T_{inlet} =565/290 °C).

(A) Commissioning for Tinlet = 565 °C, charging for 280 hours. (B) Temperature at final time.

Figure 2-7 (A) shows the charging and discharging cycles for three TES modules. After ~50 cycles, modules work at a defined temperature range. Observation shows that the GEO module works in a higher temperature margin, but as shown in Figure 2-7 (B), the OPC-1 module works with improved temperature differences (ΔT) for both charging and discharging over a specified time period. The higher ΔT values coupled with high thermal diffusivity characteristics allow the TES unit to change its operating temperature more rapidly.

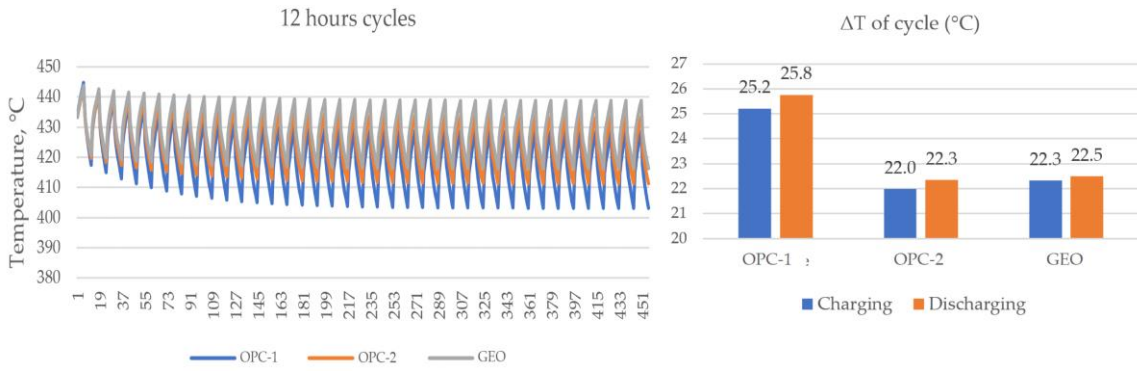

(A) (B)

Figure 2-7. Charging/Discharging cycles and ΔT for TES units (T_0 = 290°C; T_{inlet} =565/290°C).

(A) Charging/discharging cycles $T_{0,\ discharging}$ = 427.5 °C. (B) Temperature difference of each charging/discharging after stabilizing period, cycle > 50.

Temperatures inside the TES body at specified intervals along the X-axis between the tube's surface and right edge, as mentioned in Figure 3, were estimated. After the T_0 = 290 °C and T_{inlet}=565 °C were determined and the charging process was performed for 6 hours, OPC-1 achieved the highest temperature in all assessment temperature point, $T_{1,2,3}$ and $_4$. At 1 cm from the surface of the tube and after 3.5 hours, the GEO sample has a higher temperature than OPC-2 (Figure 2-8). This is because the temperature at that point is reaching the value where the thermal diffusivity of the GEO sample is higher.

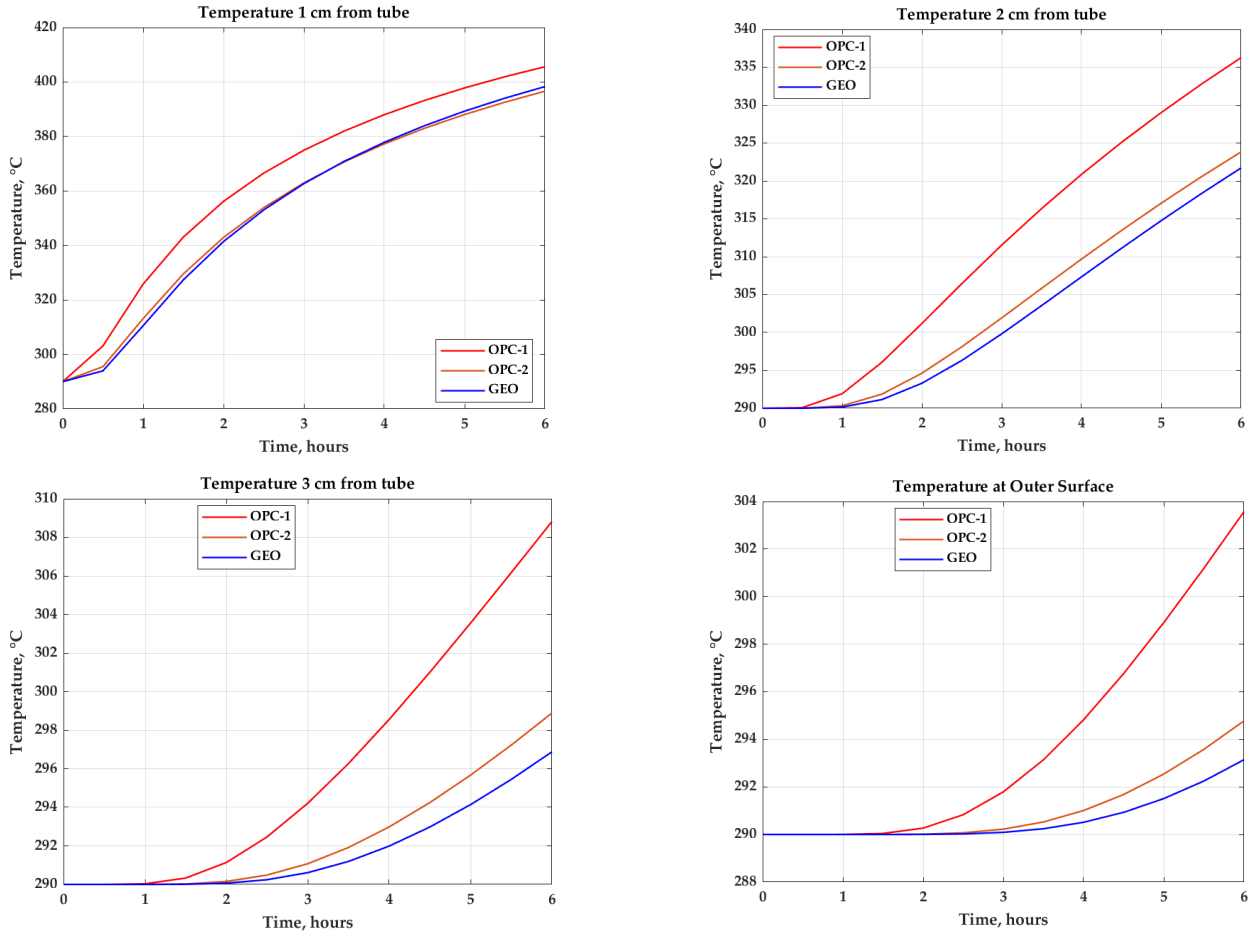

Figure 2-8. Transient temperature at different locations (T_0 = 290°C; T_{inlet} =565/290°C).

Transient temperature at different intervals after 6 hours.

The temperature distribution map, heat flux vector field and calculated average temperature for 6 hours of charging and discharging are shown in Figure 2-9. In the charging scenario (first row), the OPC-1 sample has the highest average temperature, and OPC-2 and GEO samples have relatively close average temperatures, with less than 1 °C difference. For the discharge scenario (Figure 2-9, second row), the calculated $T_{average}$ of GEO is lower than that of OPC-2 even though the values for OPC-1 are even lower.

It is worth mentioning that these calculations have been completed knowing there is no information for properties of counterparts above 400 °C and assuming the functionality of OPC-1 and OPC-2 at high temperatures. This makes GEO concrete a

potentially good choice that is able to operate in a wider temperature range, greater ΔT, and consequently greater energy storage capacity.

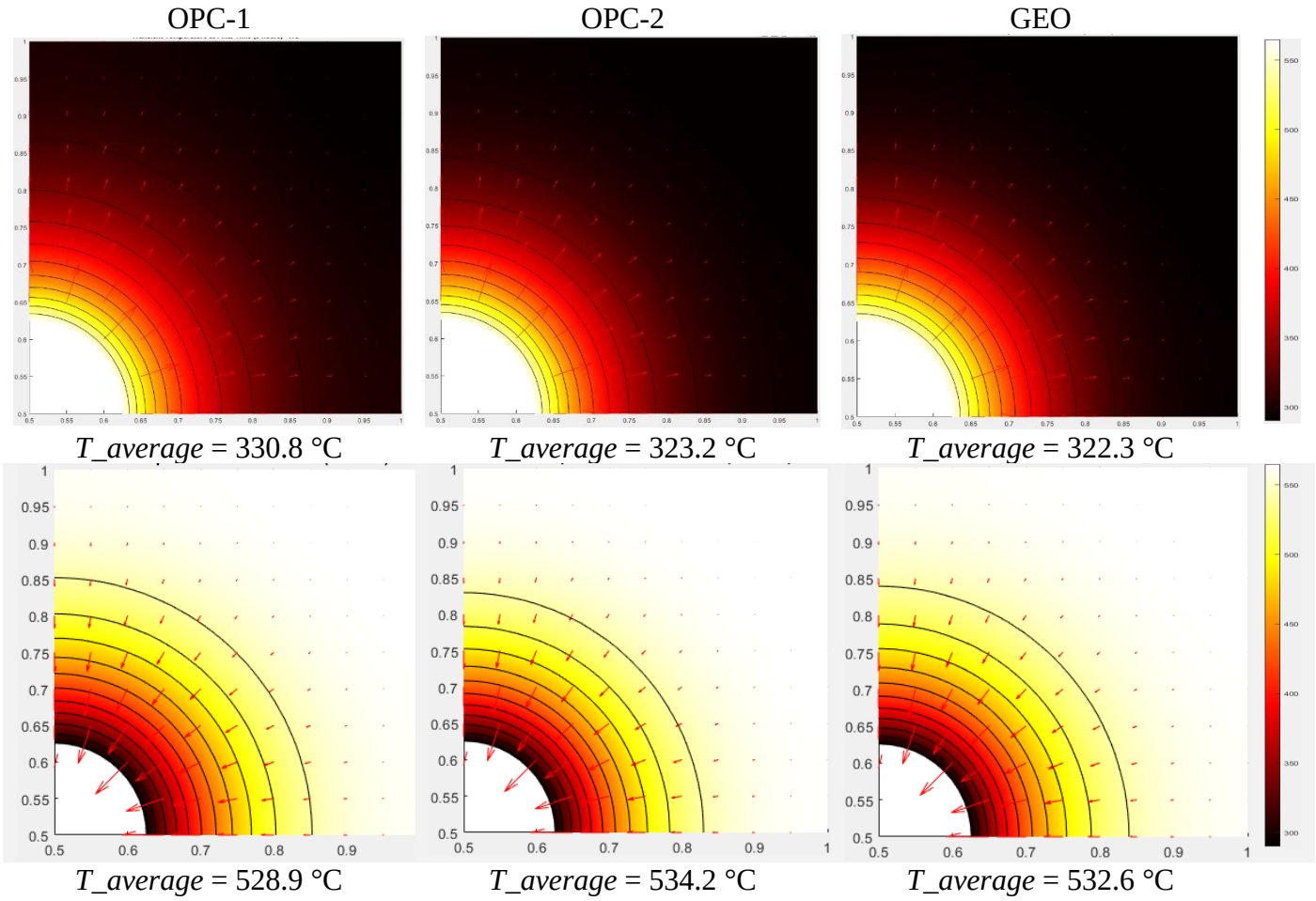

Figure 2-9. Transient temperature, heat flux distribution and average temperature after 6 hours (T_0 = 290°C; T_{inlet} =565/290°C).

First row: Charge. Second row: Discharge.

Case 2: T_0 = 290°C; T_{inlet} =700/290 °C

Assuming that OPC-based samples are able to operate in this temperature range, the GEO concrete has the better behavior. The GEO module reached the highest average temperature for T_{inlet} = 700 °C and after about 300 hours (Figure 2-10 A,B). Although Figure 2-10 C,D shows the same trend analyzed in case 1, the temperature difference of

charging/discharging after the stabilizing period, cycle > 50, for GEO is about 3% lower than that for OPC-1 and 6% higher than that for OPC-2.

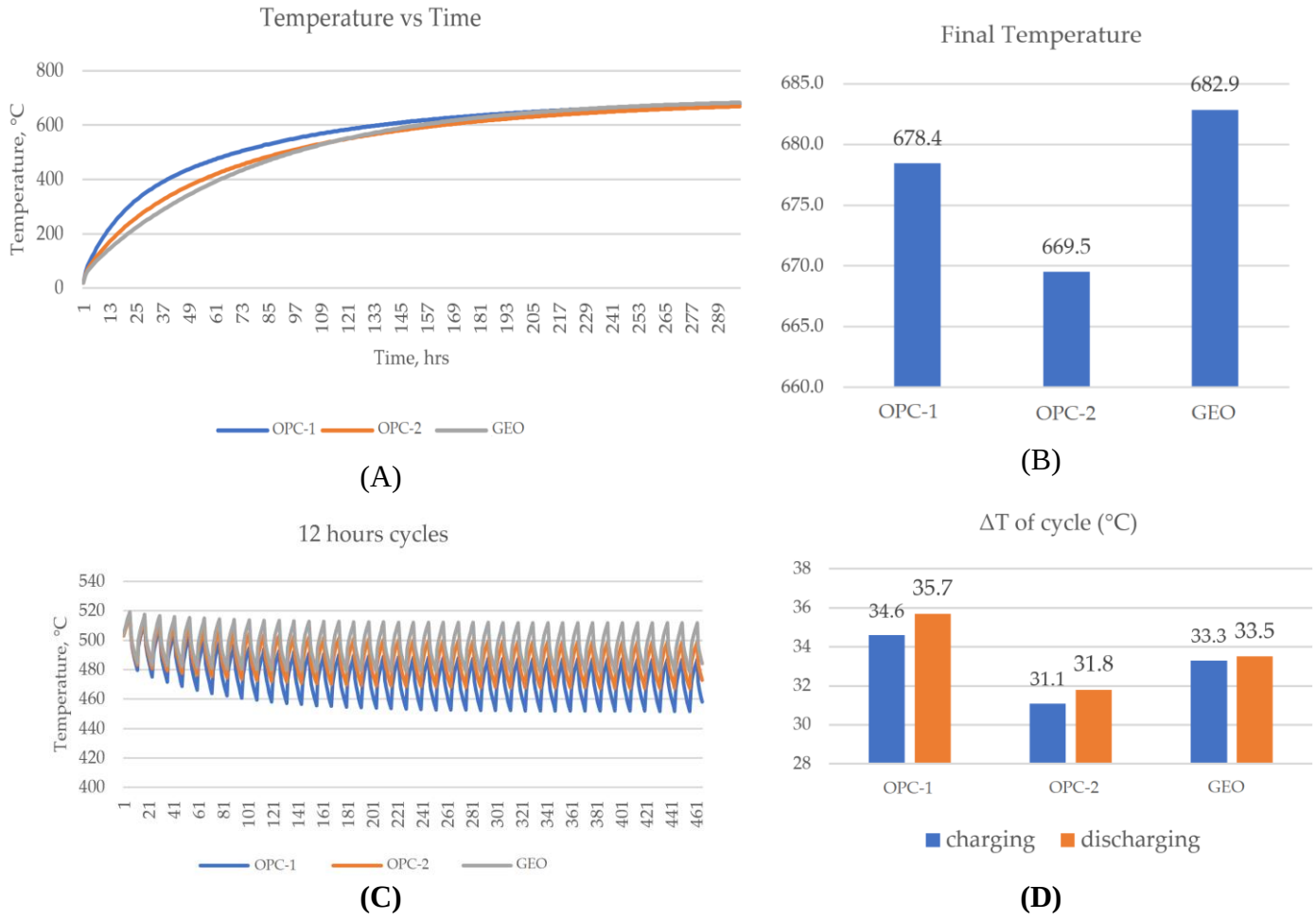

Figure 2-10. Average temperature and Charging/Discharging cycles (T_0 = 290°C; T_{inlet} =565/290°C).

(A) Commissioning for T_{inlet} = 700 °C, charging for 300 hours. (B) Average temperature of TES modules at final time. (C) Charging/discharging cycles T_0, discharging = 495 °C. (D) Temperature difference of charging/discharging after stabilizing period, cycle > 50.

Figure 2-11 shows the temperature values at different intervals inside the TES block for T_{inlet} = 700 °C and T_0 = 290 °C and after 6 hours. Unlike Case 1, this setup shows that

GEO achieves a higher temperature than OPC-2 at 1 cm from the surface of the tube and a temperature close to that of OPC-2 at 2 cm.

However, the values of OPC-1 are greater than those of OPC-2 and GEO. When TES modules were heated for 96 hours (Figure 2-12), GEO achieved the highest temperature in the 1 cm location and a higher temperature than OPC-2 in the rest of the intervals. The final average temperatures were 587.1, 568.7 and 587.3 °C for OPC-1, OPC-2 and GEO, respectively.

The results confirm what has been raised about the heat capacity and thermal stability of geopolymer-based concrete at higher temperature ranges. However, operating in the higher temperature regime leads to an overestimation of the specific heat values reported for OPC-1 and OPC-2 (Table 2-1, specific heat (J/kg °C) as a function of temperature). This was expected because extrapolating to temperatures beyond what was actually tested can lead to unrealistic and very high specific heat values. .

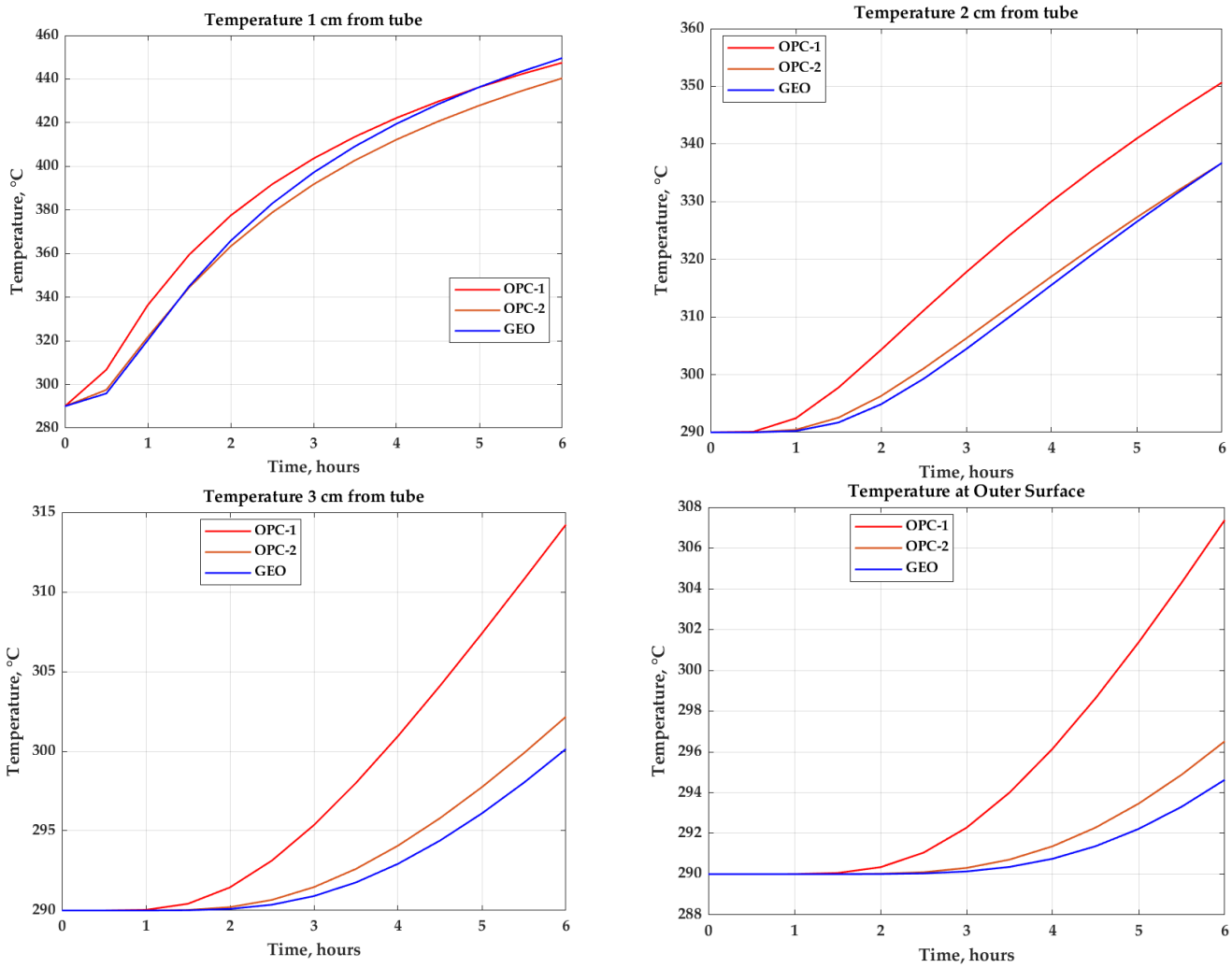

Figure 2-11. Transient temperature at different intervals (T_0 = 290°C; T_{inlet} =565/290°C)

Transient temperature of different intervals along X-axis versus time after 6 hours

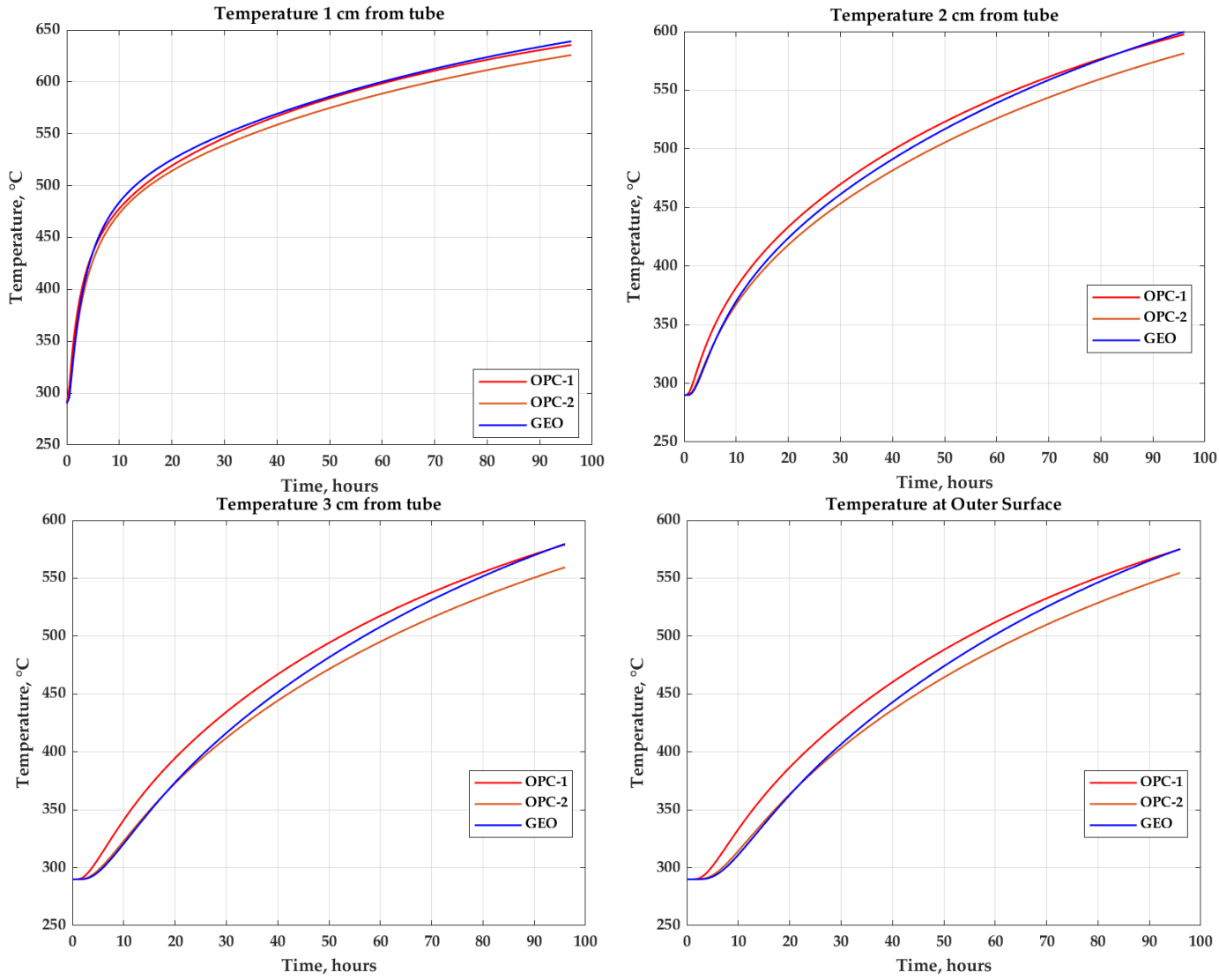

Figure 2-12. Transient temperature at different locations (96 hrs., T_0 = 290°C; T_{inlet} =565/290°C)

Temperature distribution contours and heat flux vectors for charging and discharging processes (Figure 2-13) show the same trend as Case 1. The OPC-1 sample has the highest average temperature, followed by the GEO sample and then the OPC-2 sample. However, in this scenario, the values of average temperature for GEO concrete are closer to those of OPC-1, showing about 1 °C difference with OPC-1 and 5 °C difference with OPC-2 .

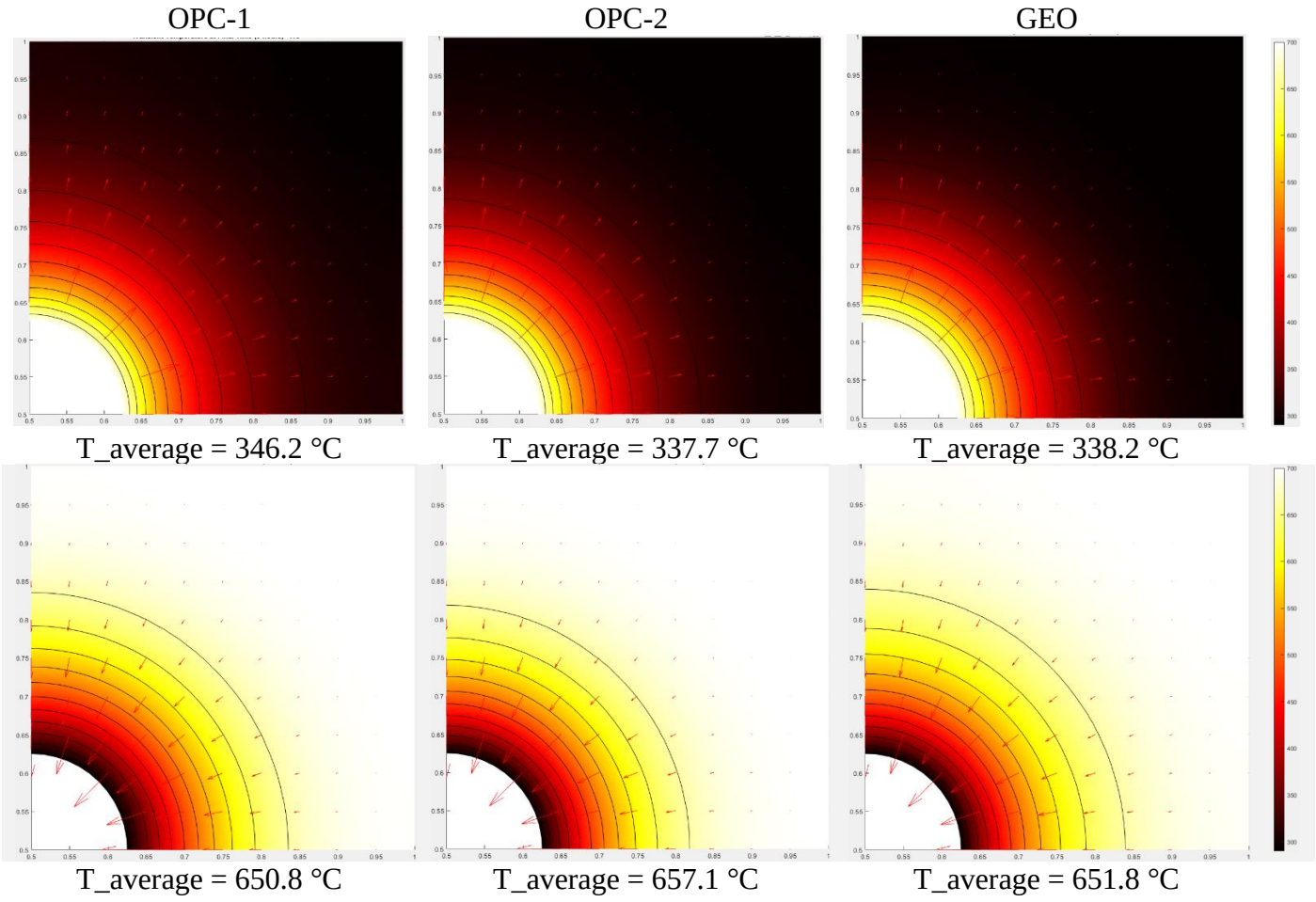

Figure 2-13. Transient average temperature and heat flux distribution after 6 hours (T_0 = 290ºC; T_{inlet} =565/290°C)

First row: Charging. Second row: Discharging

Apart from that real OPC1 and OPC2 are not able to stand temperatures above 350ºC, even extrapolating their behavior to higher temperatures, GEO thermal diffusivity is 5×10^{-7} m^2/s and is greater than that of OPC counterparts at temperatures T > 400 °C. The highest average temperature is obtained by GEO concrete, and the thermal energy storage capacity and temperature difference (ΔT) in cyclic charging and discharging operations are in a very acceptable range for TES material. Altogether, this work demonstrates that GEO concretes are a promising alternative so that CSP and SPH industries can work at higher temperatures with geopolymer-based materials.

In the next chapter, further investigations of the behavior of GEO-based concrete prototypes in realistic lab-scale test facility, subjected to various thermal scenarios will be presented. This experimental validation will provide another insight into the practical implementation of GEO concrete as a TES material in high-temperature applications.

Chapter III.

Prototype Development and Experimental Validation

3.1 Prototypes Manufacturing and Experimental Set Up

The previous section (2.4) demonstrated the potential of geopolymer-based concrete as a thermal energy storage material for high-temperature applications. Its low thermal resistance, high specific heat, and thermal stability compared to conventional OPC-based concretes suggest its ability to store and release heat efficiently under demanding temperature conditions. However, to fully assess the feasibility of GEO concrete in practical TES systems, experimental verification is necessary. This chapter delves into the prototyping and experimental validation of GEO concrete TES unit, subjected to various thermal scenarios mimicking real-world operating conditions.

A GEO prototype were fabricated using industrially produced geopolymer hybrid cement from Považská Cementáreň (Martauz et al., 2016), as mentioned in the previous chapter. This composition was chosen due to its ability to maintain a stable and high heat capacity over a wide temperature range, while the steel slag contributes to the desired thermal conductivity characteristics. In parallel, a control sample of ordinary Portland cement (OPC) concrete was prepared using the properties and formulation outlined in Table 3-1. Cubes of 10 cm^3 were cast and cured for 90 days to ensure adequate strength development. Compressive strength testing was conducted on the GEO and OPC samples, yielding values of 47.25 MPa and 50.87 MPa, respectively.

Table 3-1. Formulation of the GEO and OPC concretes.

Material	GEO	OPC
Cement	9.90 [kg]	9.00 [kg]
Limestone aggregates 0/2	-	35.25
Limestone aggregates 4/12	-	24.75
SLK aggregates 0/8	66.00	-
Water	5.78 [kg]	5.25 [kg]
Viscocrete	70.80 [g]	28.00 [g]
Sikament	104.50 [g]	95.00 [g]

To fabricate representative samples of TES devices, an embedded tube scheme was adopted, as depicted in Figure 3-1. Schedule 40 stainless steel pipe, specifically 304/304L, utilizing a 6-inch diameter welded tube, was employed. To facilitate attachment of the TES sample to the test facility, two flanges were positioned at opposite ends of the tubes. The experimental setup was housed at CIC EnergiGUNE, located in Vitoria, Spain. Three temperature probes were embedded at predetermined depths within the concrete matrix, enabling accurate monitoring of the module's temperature profile, Figure 3-1.

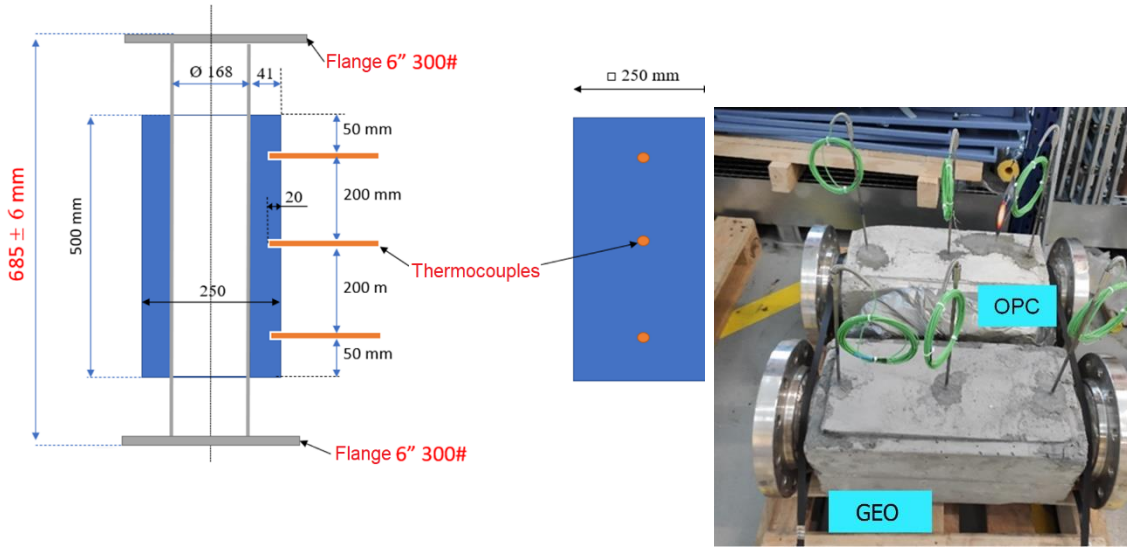

(A) (B)

Figure 3-1. Prepared TES samples with dimensions.

(A)Geometry and dimension of TES unit in mm, (B) prototyped TES modules.

Air was chosen as the circulating HTF for the TES experiment setup, in Figure 3-2. The HTF is pumped via a dedicated pump and then heated by an electric heater before being delivered to the TES modules. To ensure secure attachment and optimal heat exchange, the TES modules are flanged onto predetermined air heater tubes. Following flanging, an insulation and jacketing process is implemented to minimize thermal losses

during the experiment. This insulation helps maintain the desired temperature profile within the TES modules, ensuring consistent performance throughout the experimental cycles.

To evaluate the performance of the TES prototypes, two distinct operating scenarios were investigated. First, a low-temperature scenario involved four cycles of charging and discharging, with inlet air temperatures (T_{inlet}) fluctuating between 200 and 450 °C. These temperature ranges align with the typical operating conditions reported for OPC-based concrete (Heatcrete) (Hoivik et al., 2019), providing a benchmark for comparison. In contrast, the high-temperature scenario extended the operating envelope to a broader range, with T_{inlet} values varying between 200 to 600 °C. This extreme temperature range was explored to assess the GEO's ability to maintain operational efficiency and workability under such challenging conditions. To continuously monitor the performance of the various TES modules, real-time measurements were conducted utilizing thermocouples. These sensors recorded the temperature and velocity of the incoming air, providing view into the HTF's behavior.

(A) (B)

Figure 3-2. Thermal energy storage testing loop facility.

(A) before insulation and (B) after insulation and jacketing the module.

3.2 Procedures and Results of Experimental Runs

A comprehensive evaluation of the TES samples was conducted by conducting four thermal cycles, each lasting approximately 24 hours. These cycles enabled the investigation of the samples' behavior under varying thermal conditions and their ability to store and release heat effectively.

Two distinct thermal scenarios were explored: one with an inlet air temperature of 450 °C and another with 650 °C. To prevent thermal shock and ensure a smooth transition into the experimental cycles, a gradual start-up scenario was employed. Over a period of ten hours, the inlet air flow temperature was increased to approximately 120 °C, as depicted in Figure 3-3.

To monitor the temperature profile along the flow axis, three temperature probes (T_{1-3}) were placed within the concrete matrix, as shown in Figure 3-1(B). The preheating rate before initiating the experiment was determined for each scenario. For the 450 °C scenario, a preheating rate of 3°C/h was considered appropriate, while for the 650 °C scenario, a higher rate of 14°C/h was adopted due to the sample's prior exposure to thermal conditions.

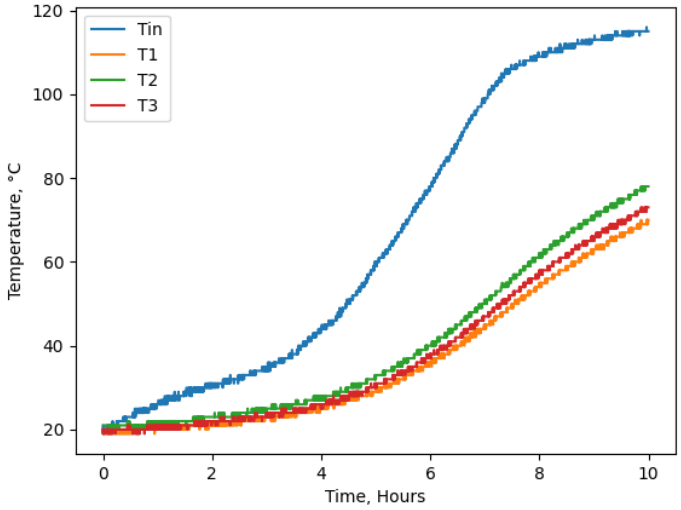

Figure 3-3. Startup scenario and first heating ramp for first 10 hours, GEO prototype.

Later, the maximum average temperatures attained by each prototype during the experiment are presented in Table 3-2, providing a quantitative comparison of their thermal storage capabilities. To gain a deeper understanding of the prototypes' behavior, complete experimental data for both temperature conditions are presented in Figures 3-4.

Analyzing the third and fourth cycles, which represent more stable thermal conditions, reveals significant temperature differences between GEO and OPC prototype. In the 450 °C scenario, the maximum temperature difference between the two prototypes is ΔT=30 °C, indicating a clear plus for GEO concrete. This temperature gap further widens to ΔT=40 °C for the 650 °C scenario, further demonstrating the thermal performance of GEO concrete.

Table 3-2. Maximum achieved temperature measured for GEO and OPC.

TES prototype	GEO (°C)	OPC (°C)
Inlet = 450 °C	398	366
	358	352
	380	350
	380	349
Inlet = 650 °C	561	500
	518	457
	503	463
	503	463

Temperature measurements presented are from thermocouple 2 located in the center of TES units.

While the exceptional performance of GEO concrete in high-temperature applications was anticipated, these results also demonstrate its competitive edge in the lower temperature range of 450 °C. This confirming GEO concrete's outstanding thermal capabilities, particularly at elevated temperatures (> 400 °C) where its thermal diffusivity remains remarkably consistent as discussed in previous chapter.

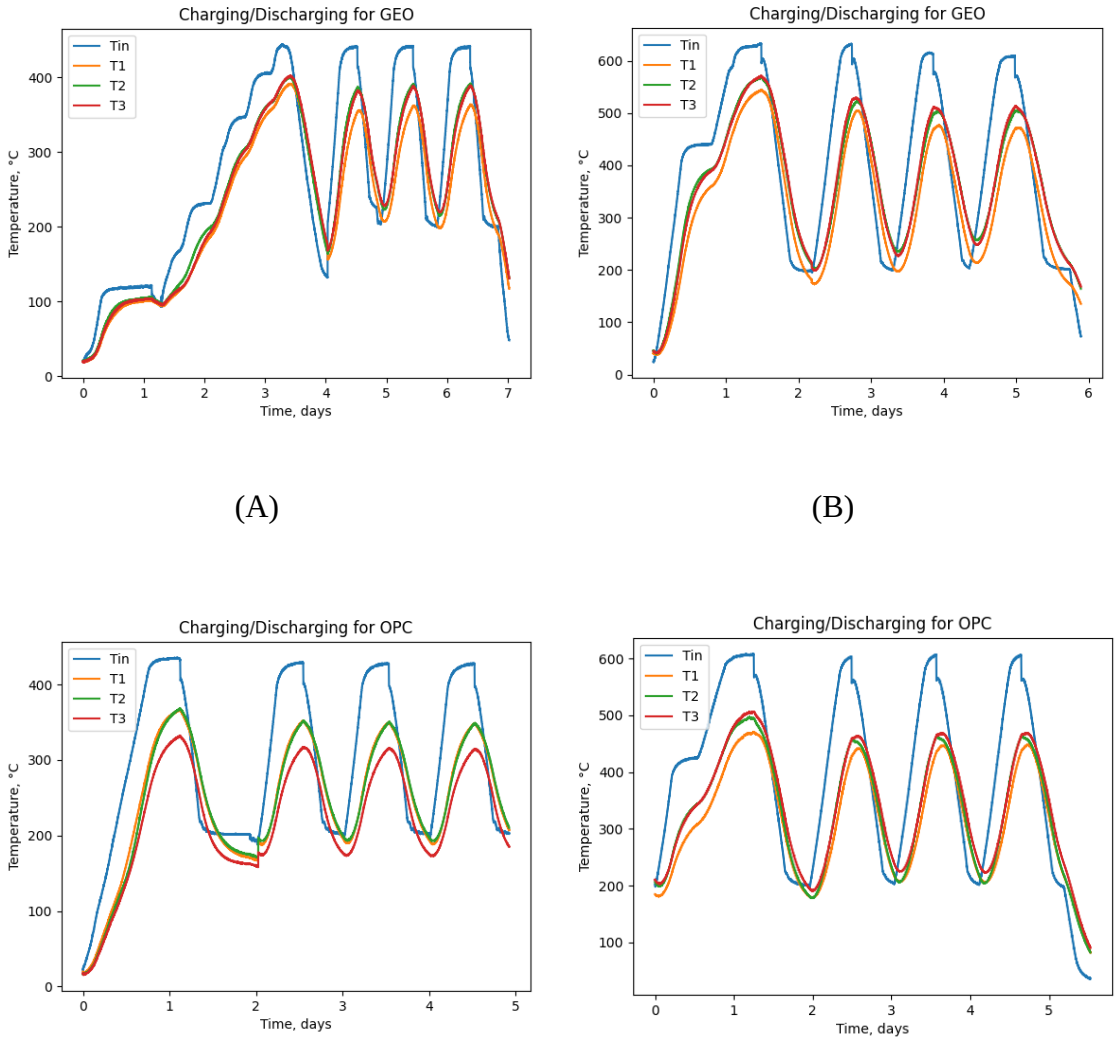

Figure 3-4. GEO and OPC concrete thermal cycles. GEO concrete.

(**A**) Low temperatures cycles (the temperature of the inlet varying from 200 ± 25 °C to 400 ± 25 °C); (**B**) High temperatures cycles (the temperature of the inlet varying from 200 ± 25 °C to 600 ± 25 °C). OPC concrete (**a**) Low temperatures cycles (the temperature of the inlet varying from 200 ± 25 °C to 400 ± 25 °C); (**b**) High temperatures cycles (the temperature of the inlet varying from 200 ± 25 °C to 600 ± 25 °C).

An average speed of 6 m/s was considered for incoming heat transfer fluid (HTF). The comprehensive pattern of HTF speed variation during the experiment is shown in

Figure 3-5. Also, the average flow rate for HTF was ± 412 m^3/h and the maximum and minimum values were 825 m^3/h and 275 m^3/h, respectively.

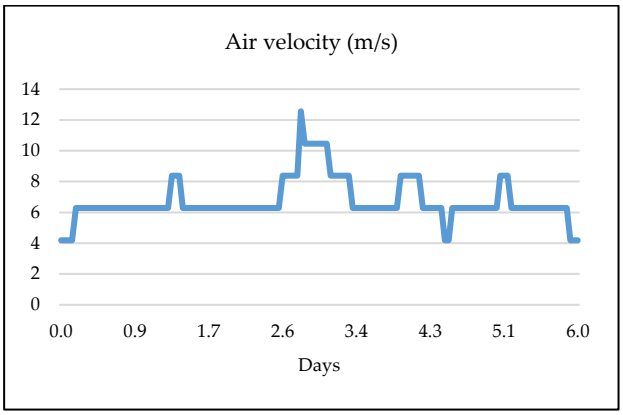

Figure 3-5. Measured HTF velocity over 6 days.

According to the results and graphs obtained Figure 3-4, other characteristics of a TES device such as thermal energy storage capacity (Q_s) can be estimated, using equation 2-1. To achieve this, the thermal properties of the materials prototypes must be available. Since the thermal properties of the tested OPC prototype are unknown, values from a state-of-the-art OPC prototype (Hoivik et al., 2019) were employed for evaluation and comparison with GEO data, as shown in Table 3-3.

Table 3-3. Thermal properties of materials prototypes.

Properties		GEO	Heatcrete
Density	kg/m^3	2890.0	2253
Thermal conductivity	W/m °K	1.2	1.78
Heat capacity	J/kg °K	1000	1280
Thermal diffusivity	*10-7 m^2/s	5.58	6.01

Data obtained at 400 °C for Heatcrete concrete (Hoivik et al., 2019).

The amount of stored thermal energy for the charge cycles of the GEO prototype is compiled for the low (T_{inlet}=450 °C) and high (T_{inlet}=650 °C) temperature scenarios in

Table 3-4. This table provides a concise overview of the operational temperature range, temperature difference, and volumetric thermal energy storage capacity (Q_{vol}) – the primary criterion for assessing the thermal performance of TES prototypes.

Table 3-4. Summary of data obtained during experiments (GEO).

Scenario	Cycle	Time, hrs.	Tmin, °C	Tmax, °C	ΔT, °C	Qvol, MJ/m^3
	1	81.6	20	397.7	377.7	1091.6
Tinlet	2	14.9	163	358	195	563.6
450 °C	3	12.0	219	380	161	465.3
	4	12.2	211	380	169	488.4
	1	35.3	44	561	517	1494.1
Tinlet	2	14.9	192	518	326	942.1
650 °C	3	14.9	219	503	284	820.8
	4	13.2	240	503	263	760.1

T_{min} and T_{max} are average of three temperature probes for GEO prototype.

The average temperature of OPC based concrete throughout its operating cycles, considering only charging cycles, is extracted and used to calculate the volumetric thermal energy storage capacity (Qvol, MJ/m^3) as outlined in Table 2-1. While the thermal properties of the OPC prototype are more favorable than GEO, the operational temperature limitations of OPC restrict the achievable ΔT to a certain range, thereby confining Qvol (as determined by Equation 2-1) to a specified range of approximately 260-265 MJ/m^3.

In contrast, the GEO prototype's wider operational temperature range enables higher ΔT values and, correspondingly, higher Qvol values. For the GEO prototype, Qvol ranges between 465 and 942 MJ/m3, which is at least two times greater and up to 3.5 times larger than that of the OPC prototype. When considering only cycles 2,3, and 4 as standard operating cycles for the thermal storage temperature range in both low and high temperature scenarios of the GEO prototype, the average Qvol is calculated and compared with the Heatcrete prototype, as shown in Table 3-5.

Table 3-5. Comparison of Qvol for GEO and Heatcrete .

Scenario	Cycles	Average Qvol, MJ/m3
GEO (Tinlet 450 °C)	2-4	505.27
GEO (Tinlet 650 °C)	2-4	841
Heatcrete (Tinlet 400 °C)	1-4	261.25

As evident from Table 3-5, the GEO prototype possesses superior thermal storage capacity owing to its ability to function over a broader temperature range. This feature, along with its capacity to operate at higher temperatures, renders GEO material more adaptable for applications, particularly in solar energy-related industries, where it can bridge the gap between generation and storage capacity. Furthermore, the need for durable, cost-effective, and high-temperature TES systems is apparent in applications such as converting electricity to thermal energy and recycling excess heat in industries.

In the upcoming phases of this research, it is crucial to develop a robust simulation model that can accurately predict GEO-TES device performance. Moreover, employing a robust numerical model will play a key role in the design of the heat exchanger, as it directly impacts charge/discharge efficiency.

Chapter IV.

Computational Modeling and System Optimization

The previous chapters have delved into the fundamental aspects of thermal energy storage systems, particularly those utilizing geopolymer as a novel TES material. This chapter focuses on developing a robust numerical model capable of accurately predicting the performance of sensible solid thermal storage devices, in general, focusing our attention on those that use GEO concrete. The model will be employed to study various configurations, operating conditions, and the impact of implementing or not implementing a metallic tube for enclosing the HTF within the TES system.

Developing a reliable computational model is crucial for several reasons. First, it allows for rapid and cost-effective evaluation of different design configurations and operating strategies without the need for extensive experimental work. This is particularly valuable in the early stages of device development, where rapid prototyping and testing can be resource intensive. Second, the model can simulate the behavior of sensible solid TES systems under various environmental conditions, including different ambient temperatures, heat transfer fluid properties, and operating cycles. This enables a comprehensive understanding of the system's performance under diverse scenarios, enhancing its applicability in real-world applications.

Third, the model can facilitate optimization studies to identify the optimal design parameters and operating conditions that maximize the TES system's thermal performance, and overall efficiency. In this chapter, a numerical model will be developed based on the heat equation in solids, incorporating the thermophysical properties of geopolymer TES materials. The model will consider various geometrical configurations, as well as different initial and boundary conditions. The impact of implementing a metallic HTF piping will be evaluated to assess its influence on heat transfer and overall, TES performance.

The developed numerical model will be validated against experimental data obtained from the test facility described in Chapter III. This validation will ensure the model's accuracy and reliability for predicting the performance of GEO-TES systems under various operating conditions.

4.1 Development and Validation of the Numerical Model

Computational methods have permeated various disciplines, including scientific research, engineering, and computer science. These methods, encompassing algorithms, mathematical models, and computer simulations, provide powerful tools for solving problems, analyzing data, and also making predictions. Its utilization helps to tackle challenges that would otherwise be impractical or time-consuming to address manually.

Moreover, computational methods play a fundamental role in solving optimization problems in engineering and industry. Optimization algorithms can identify optimal solutions given specific constraints and objectives. These methods are employed to optimize processes, designs, logistics, and resource allocation, enhanced efficiency, and improved decision-making (DEB, 2012; Khamis, 2024; Kochenderfer and Wheeler, 2019).

Various numerical methods, such as the Finite Difference Method (FDM), Finite Element Method (FEM), and Finite Volume Method (FVM) (Liu and Quek, 2014a; Özişik et al., 2017), among others, are regularly employed for developing computational models of thermal energy storage systems.

In circumstances with simple geometries and boundary conditions, it is feasible to seek exact solutions using analytical methods. These methods may involve techniques such as the separation of variables, method of characteristics, Fourier series, and Green's function methods (Hahn and Özisik, 2012; Ozisik, 2013).

However, despite their capacity for generating accurate solutions, the practical application of these methods can often be limited, especially when confronted with complex real-world problems that include intricate geometry and boundary conditions. Numerical methods discretize the continuous problem into a finite set of points, allowing for the approximation of derivatives. For practical implementations in TES systems, an appropriate method must be selected to accurately model the heat transfer process (Liu and Quek, 2014a).

The choice of method is governed by the specifics of the system under consideration, and often a combination of methods may be required to address different aspects of the problem. The specifics include geometry of the storage system, boundary conditions, computational resources, system design and operational constraints.

Among studies on design and optimizing TES units, FEM found its position. This computational approach has gained widespread recognition among researchers in the field, with numerous studies employing FEM (Cabeza et al., 2022a; Ferone et al., 2014; Laing et al., 2008; Rafidi and Blasiak, 2005; Singh and Sørensen, 2017; Vigneshwaran et al., 2019)

While the parameters outlined constitute the main considerations in the selection of modeling methods for TES systems, ease of implementation, maturity of the method can significantly influence the decision-making process. The use of commercial software in thermal energy storage modeling often requires consideration of the above factors. Tools like ANSYS Fluent ("ANSYS Fluent," n.d.), COMSOL Multiphysics ("COMSOL Multiphysics," n.d.), MATLAB's Simulink ("MATLAB," n.d.) and Modelica have established themselves as leading solutions in the field due to their robustness, flexibility, and wide range of capabilities. Open-source alternatives like OpenFOAM ("OpenFOAM," 2023) offer similar capabilities, albeit with a steeper learning curve and less comprehensive user support.

On the other hand, using computing and simulation tools and software allows us to model complex energy storage systems more easily. For instance, In a study conducted by Tamme et al. (Tamme et al., 2004a), a high temperature concrete sensible heat storage (SHS) system was developed and tested for parabolic trough solar power plants. The simulation tool employed, StorageTechThermo, utilizes the Modelica language. In another study, Tesfay (M Tesfay, 2014) dove into the design and analysis of a SHS system for solar thermal power plants using commercial software, Gambit and Fluent ("ANSYS Fluent," n.d.).

The design and fabrication of heat exchangers (HXs), or thermal storage devices, with sensible solid materials can be approached in two main ways: modular and integral. Integral HXs are monolithic entities that are cast or fabricated as a single unit, typically with the storage medium (e.g., concrete) included in their structure. Modular HXs, on the other hand, are composed of smaller, interconnected modules that can be easily added or removed. This modular design offers several advantages, including scalability, flexibility and repairability.

The modular approach has been extensively studied and applied to concrete TES systems (Cabeza et al., 2022a; Hoivik et al., 2019; Laing et al., 2006, 2008, 2012, 2012;

Prieto et al., 2023; Suárez et al., 2020) while integral design has been relatively neglected. The specific design of the modules can also be tailored to the type of concrete used, the desired operating temperature range, and the desired heat transfer rate.

The purpose of creating a validated 3D numerical model of the tested GEO module was to have a good tool to study and design an upscaling thermal storage regenerator with this GEO concrete. To lay the groundwork for this investigation, a three-dimensional Multiphysics FEM based numerical model developed using CFD, to validate with experimental data presented in previous chapter. Primary objectives encompass two key stages. First, to characterize the thermal energy storage capacity and thermal performance of a TES device based on geopolymer concrete, considering critical factors such as air velocity, piping diameter, and module size.

Second, a parametric study encompassing various piping sizes, arrangements, and configurations to optimize the design of a TES system employing GEO concrete. This step is pivotal for evaluating the scalability and adaptability of geopolymer concrete-based TES systems for practical applications.

As mentioned in previous chapter, for the Heat Transfer Fluid (HTF), a 6-inch diameter welded tube made of stainless steel 304/304L was used as a pipe. The thermal conductivity of stainless steel tubes is 44.5 W/m·K, and heat capacity is 475 J/kg·K. The stainless steel tube also has a density of 7850 kg/m^3. The tube was equipped with two flanges at its ends to ensure seamless integration with the testing facility. Additionally, three temperature probes (T_1, T_2, and T_3) were embedded into the concrete at predetermined intervals. In this study, the HTF was air, which was heated using an electric heater before passing through the GEO module being evaluated.

The thermo-physical properties of the GEO concrete were measured and presented in Table 2-1. The experiment incorporated four such cycles, with the inlet temperature (T_{inlet}) varying from 200 ± 25 °C to 600 ± 25 °C. The volumetric air flow rate registered an average of 412 m^3/h, often oscillating between maximum and minimum values of 825 m3/h and 275 m3/h, respectively. Given this data, it is reasonable to assume an average air velocity of 6 m/s.

4.1.1 Numerical Model Setup (3D)

To facilitate computational efficiency, the numerical model was developed utilizing COMSOL Multiphysics software ("COMSOL Multiphysics," n.d.). Given the expected axial symmetry of the GEO module, only a quarter section of the GEO TES module was modeled. Benefits of symmetry utilization was discussed in section 2.3. The mesh was constructed using a combination of tetrahedral and quadratic elements, ensuring finer resolution near boundaries and coarser resolution in other regions. A refined boundary layer mesh was incorporated within the HTF domain, specifically in the vicinity of the piping. This approach aimed to precisely capture the transition region where the air velocity transitions from zero to its fully developed state, commonly referred to as the dynamic boundary layer. Figure 4-1 aptly illustrates this crucial region. Three distinct domains were defined: one for the air as HTF, another for the piping, and the final domain for the concrete.

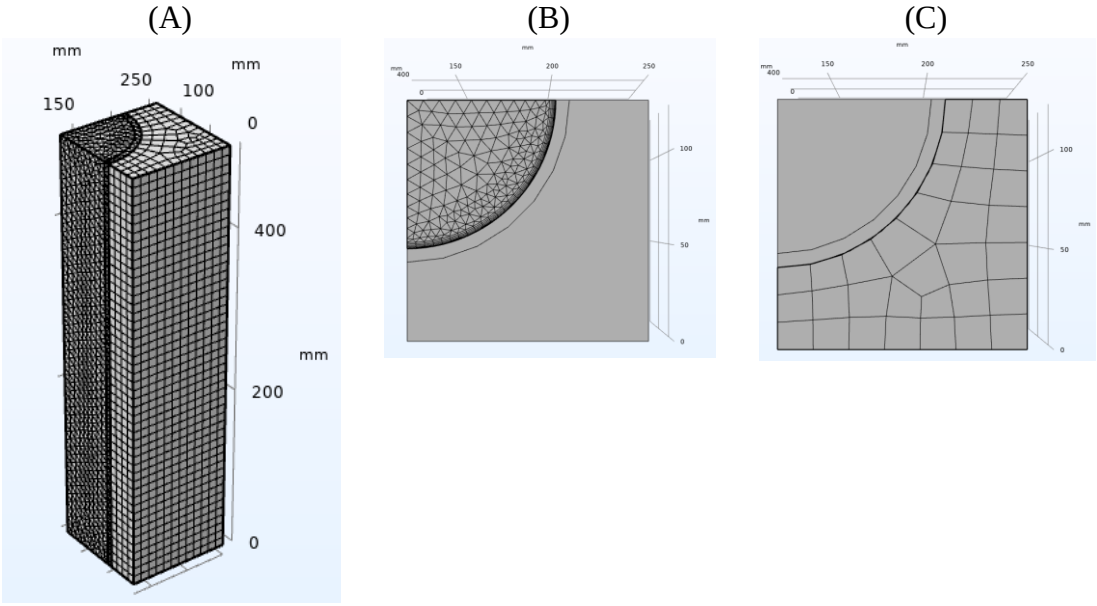

Figure 4-1. Meshed computational domain for TES.

(A) Perspective view of meshed TES module, quadratic elements used for concrete domain and tetrahedral for tube wall and fluid domains, (B) Fine mesh development near fluid to solid interphase, (C) showing mesh growth and benefiting coarse mesh in regions with low complexity.

To ensure the accuracy and validity of the mesh, six different grid sizes were evaluated, each with a varying number of elements, while adhering to a maximum element growth rate restriction of 1.15.

Employing the charging time, the duration for a TES module to attain its steady-state condition, as a comparative parameter, it was observed that reducing the grid size from 95096 elements to 55445 elements significantly influenced the charging time value. However, a further reduction from 55445 elements to 25349 elements resulted in negligible discrepancies.

This observation is depicted in Figure 4-2. Therefore, the grid with 25349 elements was deemed adequate for subsequent simulations.

Table 4-1. Maximum errors and average error percentages in charging time for each grid size compared to 95096 grid size elements.

Grid size (n. of elements)	Maximum Deviation (%)	Mean Deviation (%)
72652	0.67%	0.85%
55445	1.03%	0.56%
41218	0.51%	1.72%
25349	1.00%	0.54%
21802	0.04%	2.13%

It is important to note that while finer mesh sizes generally enhance accuracy, they also commensurately increase computational demands. Table 4-1 presents a comparison of the maximum errors and average error percentages associated with each grid size, relative to the highest grid size (95096 elements), with respect to the charging time parameter.

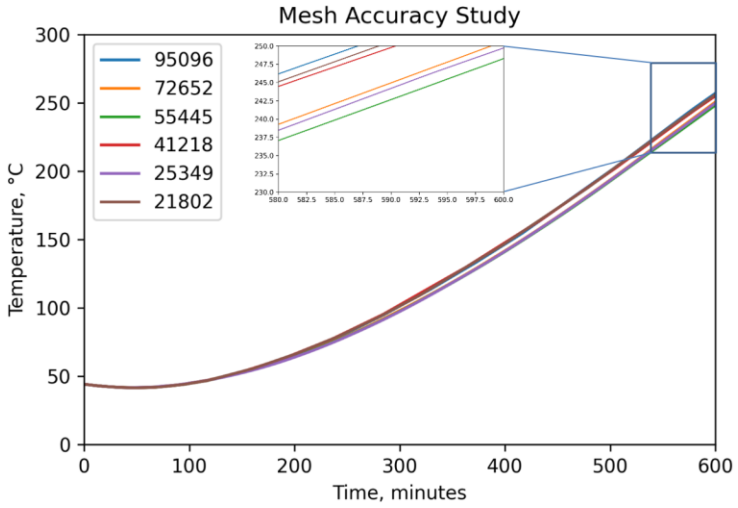

Figure 4-2. Mesh accuracy study for numerical model.

In order to effectively address the conjugate heat transfer problem, it is imperative to consider the conservation of energy, mass, and momentum in both solid and fluid media, as well as to apply appropriate boundary conditions.

Conjugate heat transfer refers to the coupled heat transfer analysis between a solid and a fluid. It combines heat conduction in the solid with heat convection in the surrounding fluid. Heat transfer in solid considered only conduction and follows Fourier's law, Equation 2-4, which in 3-D Cartesian coordinates becomes Equation 4-1.

$$\frac{\partial}{\partial x}\left(k\frac{\partial T}{\partial x}\right)+\frac{\partial}{\partial y}\left(k\frac{\partial T}{\partial y}\right)+\frac{\partial}{\partial z}\left(k\frac{\partial T}{\partial z}\right)=\rho c\frac{\partial T}{\partial t} \tag{4-1}$$

Equation 4-2 encapsulates the principles governing heat transfer in a moving fluid, incorporating three primary contributors: convection, viscous dissipation, and pressure work. Convection arises from the movement of the fluid itself, transporting heat along with the moving mass. This convective heat transfer can be significantly more potent than conduction, particularly in fluid flows with high velocities or complex geometries, where this turbulence enhances heat transfer.

Viscous dissipation, a secondary contribution to heat transfer, stems from the frictional forces generated by the fluid's motion. These frictional interactions dissipate kinetic energy into thermal energy, effectively heating the fluid. Pressure work, the third factor influencing heat transfer, emerges when the fluid density is temperature dependent. As the temperature changes, the fluid's density also alters, leading to pressure variations. These pressure changes can induce work, which in turn generates heat.

Equation 4-2 mathematically represents these heat transfer mechanisms:

$$\rho C_p \frac{\partial T}{\partial t} + \rho C_p \mathbf{u} \cdot \nabla T = \alpha_p T \left(\frac{\partial p_\mathrm{A}}{\partial t} + \mathbf{u} \cdot \nabla p_\mathrm{A} \right) + \tau : S + \nabla \cdot (k \nabla T) + Q_{src} \qquad (4\text{-}2)$$

Where, $\rho \cdot c_P$: fluid density and specific heat capacity, **u**: fluid velocity, T: fluid temperature, p_A: thermodynamic pressure, α_p: thermal expansion coefficient, τ: viscous stress tensor, S: strain rate tensor, k: thermal conductivity, Q_{src}: heat source.

The heat transfer physics at the interface between the solid and fluid domains are solved simultaneously. The L-VEL (spf) interface in COMSOL Multiphysics is designed for turbulent flow simulations. It solves the flow equations together with models for turbulence using a low Reynolds number turbulence model.

This interface can be coupled with the Heat Transfer in Solids and Fluids interface to perform conjugate heat transfer analysis. The following assumptions were made in the three-dimensional numerical simulation:

1) the outer shell boundary of the GEO module is adiabatic,

2) the GEO material is homogeneous and isotropic, and

3) radiative heat transfer is negligible.

The following initial and boundary conditions were employed in the simulations:

- Module initially at a uniform temperature, with the average temperature equal to the initial temperature:
  - $T_{avg}(x, y, z, t=0) = T_0$

- The exterior boundaries are adiabatic, meaning no heat is exchanged through the boundary, and the temperature gradient is null:
  - $k\frac{\partial T(x=0,L,t)}{\partial x} = 0; k\frac{\partial T(y=0,L,t)}{\partial y} = 0 ; k\frac{\partial T(z=0,L,t)}{\partial z} = 0$

- The velocity of the fluid (air) at its inlet (z=0), is specified as well as its temperature:
  - $v(r, \theta, z = 0, t) = v_{air}$ and $T_{air}(r, \theta, z = 0, t) = T_{air,\,in}$.

- At the air outlet, (z=L), the normal heat flux is zero and the pressure is the atmospheric pressure. At $z = L; \vec{n}(k_{air}\,\nabla T_{air}) = 0$ and $P(r, \theta, L, l) = P_{atmospheric}$

- No slip condition, i.e., the fluid velocity is zero at the solid interphase. $v(r = d_l/2, \theta, z, t) = 0$

4.1.2 Numerical Model Results

The simulation performed for the initial 10 hours of the GEO concrete charging cycle yielded satisfactory concordance with experimental measurements of temperatures at different locations. The mean errors for the four monitored temperatures were 17.0%, 2.6%, 4.9%, and 5%, respectively. This evidence bolsters the model's ability to accurately simulate the prevalent heat transfer mechanisms. Figure 4-3 illustrates the comparison between the numerical model's simulations and experimental measurements for various thermocouples (1 to 3) and the bulk average temperature.

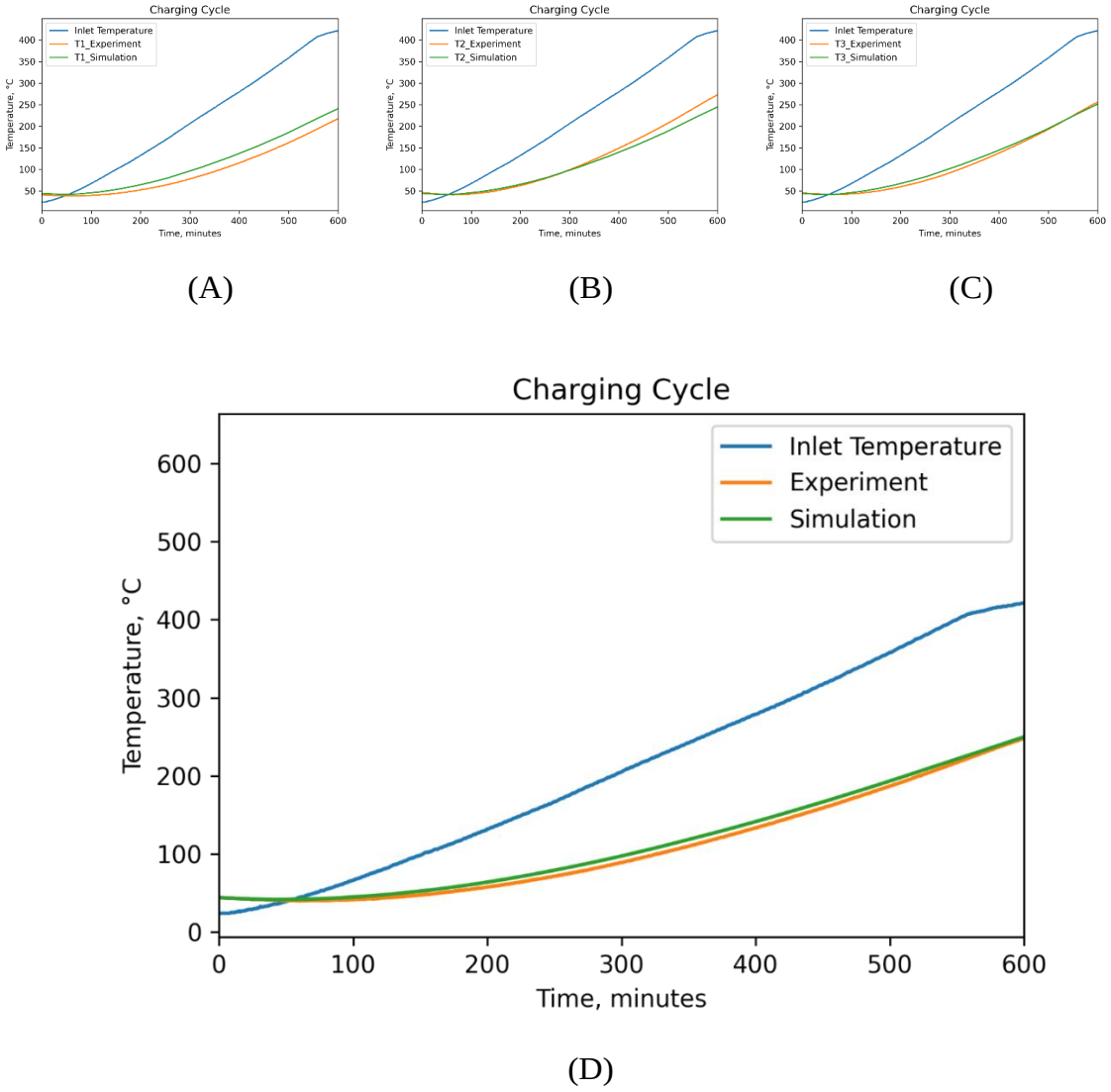

Figure 4-3. Comparison of simulation and experimental results in charging for 600 minutes.

(A) T_1, (B) T_2, (C) T_3 and (D) Average temperature (T_{avg}).

To reinforce the validity of the numerical model, the last three charging processes of experiments were simulated. The differences between simulated and experimental results were in the range 8-10%, which can be considered an acceptable deviation considering the uncertainties present in the experiment, such as temperature measurement errors or non-negligible heat losses. The assumption of a uniform temperature at the start

of simulation, which is a common practice in CFD, is a major source of uncertainty, too. Figure 4-5 illustrates the temperature distribution during the charging simulation at various time intervals through contour plots.

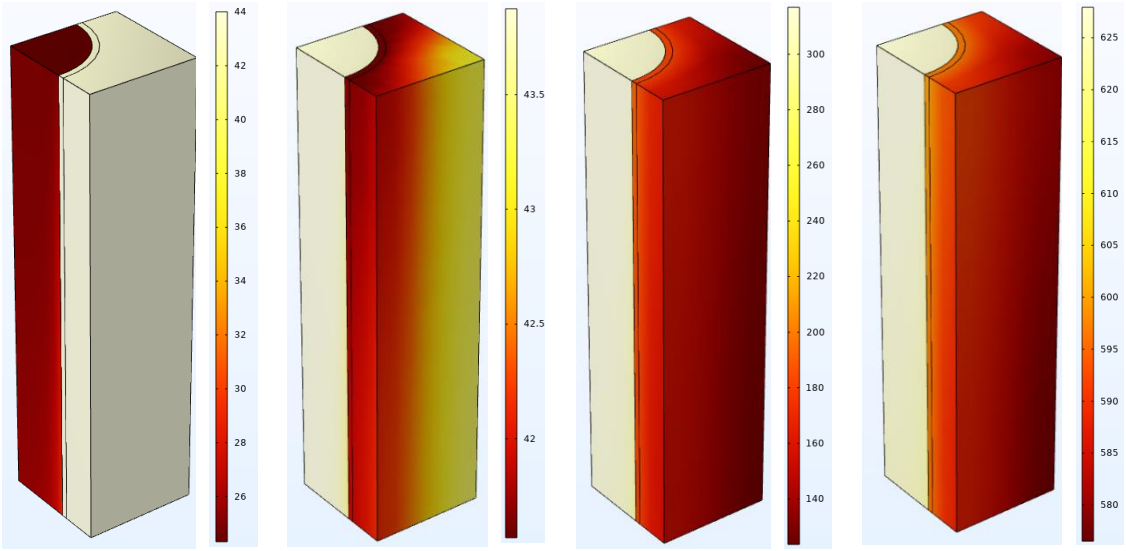

Time=0 min Time=60 min Time=450 min Time=2000 min

Figure 4-4. Average temperature distribution during the charging simulation

Resuming, a robust numerical model was developed to accurately simulate the heat transfer processes within the GEO TES module. The model was validated against experimental data, demonstrating its ability to capture the dominant heat transfer physics. The fine mesh resolution and boundary layer treatment ensured the model's fidelity in capturing the intricate flow patterns within the TES module. The well-established numerical model forms the cornerstone of the subsequent parametric studies, optimization, and final TES design.

It provides a powerful tool for systematically exploring the effects of various design parameters, configurations, air velocity, and boundary conditions on the TES performance. This allows for optimizing the TES design to maximize its efficiency and storage capacity.

4.2 Parametric and Optimization Study

This section delves into the optimization of the TES module design based on the insights gained from the parametric analysis and comparison of modular design with and without metallic tube. This optimization process aims to identify the optimal configurations and parameters that maximize the TES module's efficiency and storage capacity. The numerical model serves as the foundation for this optimization, allowing for systematic exploration of various design options and the evaluation of their impact on TES performance.

Cabeza et al. (Cabeza et al., 2022b) have outlined five essential challenges that require careful consideration for the effective implementation of concrete TES systems. These challenges encompass aspects such as on-site construction logistics, managing the disparate thermal expansion coefficients between HTF tube and concrete, mitigating the inherent low thermal conductivity of concrete, working within the constrained temperature range of HTF, and addressing the potential issue of HTF migration within the concrete structure. Concrete-based TES systems often use a tube embedded in the storage medium to transport the HTF (Laing et al., 2006; Salomoni et al., 2014; Skinner et al., 2014).

However, this approach can lead to mechanical stresses and potential failure of the system due to the different thermal expansion coefficients of the tube material and the storage medium (Cabeza et al., 2022b). A novel approach to address this challenge is to use air as the HTF in direct contact with the concrete.

This approach eliminates the need for a tube and can potentially alleviate the problems associated with thermal expansion mismatch. However, it also introduces new complexities, such as the impact of concrete surface roughness on the flow and heat transfer characteristics, as well as corrosion and long-term durability. Given the challenges and opportunities associated with concrete TES systems, a two-stage optimization investigation is done to determine the most effective design for utilizing concrete as a storage medium.

4.2.1 Stages and Objectives

The first stage focuses on conducting a parametric analysis to evaluate the impact of various geometric parameters on the thermal performance of concrete TES systems. Key variables to be considered include tube diameter, module size, module depth, inlet temperature, initial temperature, charging time, velocity, and the inclusion of a metallic pipe. The second stage delves into a more detailed comparison of modular concrete TES designs with and without a metallic tube and evaluating the impact of piping presence on heat transfer efficiency, pressure drop, and system performance. By comparing these design options, the optimal approach for specific applications can be determined.

Pearson's correlation coefficient was used to investigate the relationships between different design parameters and TES performance. This allowed for identifying the most influential parameters and understanding their impact on the thermal performance of the module. A more in-depth study will investigate the influence of concrete surface roughness on airflow and heat transfer in concrete TES systems. This aspect has often been overlooked in previous research, despite its potential impact on system performance. The study will build on existing knowledge and further explore the relationship between concrete surface roughness and TES performance parameters. The objective of Stage 1 was to assess the influence of metallic pipe diameter, which is commercial stainless steel 304/304L, and of the overall size of the TES unit on its thermal performance using numerical simulations. Three design schemes with varying tube diameters (0.5–2 inches) and sizes (175–300 mm) but a fixed depth of 1 m were considered (Figure 4-5).

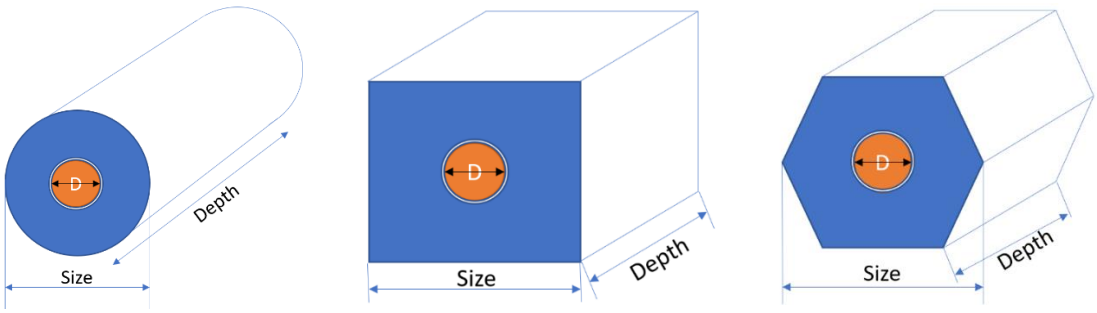

Figure 4-5. Different TES units' configurations.

Different geometry designs, pipe diameter and sizes. Pipe diameter is based on sch40-304/304L Welded Tube standard.

The performance of each design was evaluated with a fixed prescribed temperature boundary condition (Dirichlet) of 650°C at the inner surface of the tube and a temperature increase of 10.5°C per minute for the first 60 minutes. The external boundary of the units was assumed to be perfectly insulated, so thermal losses were considered negligible. The selection of the optimal GEO-TES module design in this study is primarily based on thermal energy storage capacity (Q_s) and its value normalized by mass (kJ/kg).

These criteria were evaluated to identify the design that could store the most energy per unit mass and volume, respectively, and those that achieved higher temperature increases, indicating more efficient heat transfer. The detailed simulation conditions can be seen in Table 4-2.

Table 4-2. Simulation conditions.

Conditions	Stage 1	Stage 2
Description	Parametric analysis and comparison of different geometries (square, circular and hexagonal) and size.	Parametric analysis and comparison of modular design with and No metallic piping (square geometry)
Tube diameter (in)	½, ¾, 1, 1 ¼, 1 ½, 2 (air-concrete interphase)	½, ¾, 1 (stainless steel-concrete interphase)
Module Size (mm)	175, 200, 225, 250, 275, 300	100, 150, 200, 250, 300
Module Depth (mm)	1000	1000
Inlet Temperature (°C)	650 (interphase air-solid temperature)	450 (air temperature at its entrance)
Initial Temperature (°C)	25 (ambient)	265
Charging Time (h)	7	7,5
Velocities (m/s)	N/A	3, 6, 9
Including a metallic pipe	YES	YES and NO
TES Module Boundary	No thermal losses	No thermal losses

Thermal properties of materials are based on GEO (Table 2-1) and stainless steel sch40 tube.

The calculated Q, normalized by mass, is shown in Fig. 4-7. The values of this stored energy density (in kJ/kg) are similar for the three designs and remain relatively constant with changes in size (‘L’ label in mm) or tube diameter (‘D’ label in inches).

The circular design (Fig.4-6(A)) was found to have the highest stored energy density, since, in spite of having a relatively lower concrete mass, the temperature step is much higher.

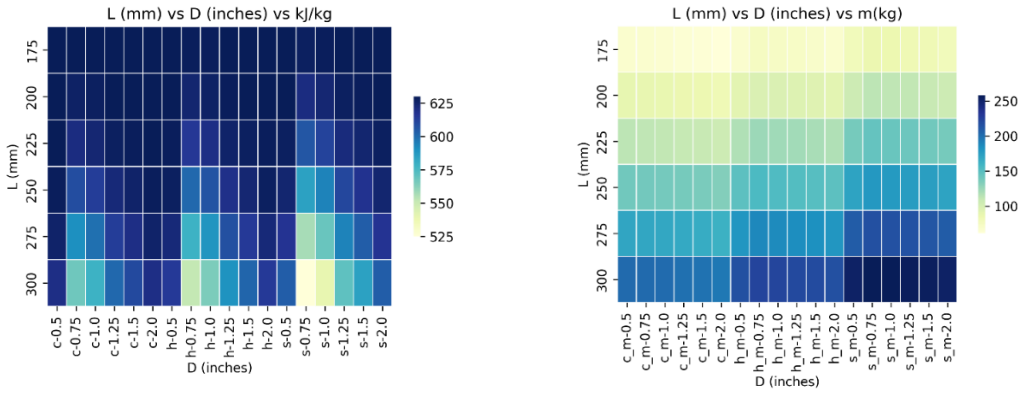

(A) **(B)**

Figure 4-6. Thermal energy storage calculations normalized by mass.

(A) Color-map of Stored Energy Density (kJ/kg) (B) Color-map of concrete mass (kg). Both for various module sizes (L) and tube diameter (D) (inches) with different designs, distinguishing between them by a preceding “c”, ”s,” “h” depending on having circular, square and hexagon (Fig.6.C) designs, respectively.

However, this is not the case for thermal storage capacity. The following color-maps (Fig. 4-7) show the thermal energy storage capacity for the three designs here considered. The square geometry had the highest thermal energy storage capacity. The diameter of the tube was found to significantly impact the energy storage capacity, Qs, of the TES. The circular model, despite having the highest average temperature, had a lower thermal energy storage capacity.

The difference in thermal energy storage capacity ranged from 29 to 75 MJ, while the difference in material mass ranged from 47 to 139 kg, indicating that mass is not the primary factor affecting TES capacity, since, fixing the charging time, the temperature achieved in the TES with the different designs are different.

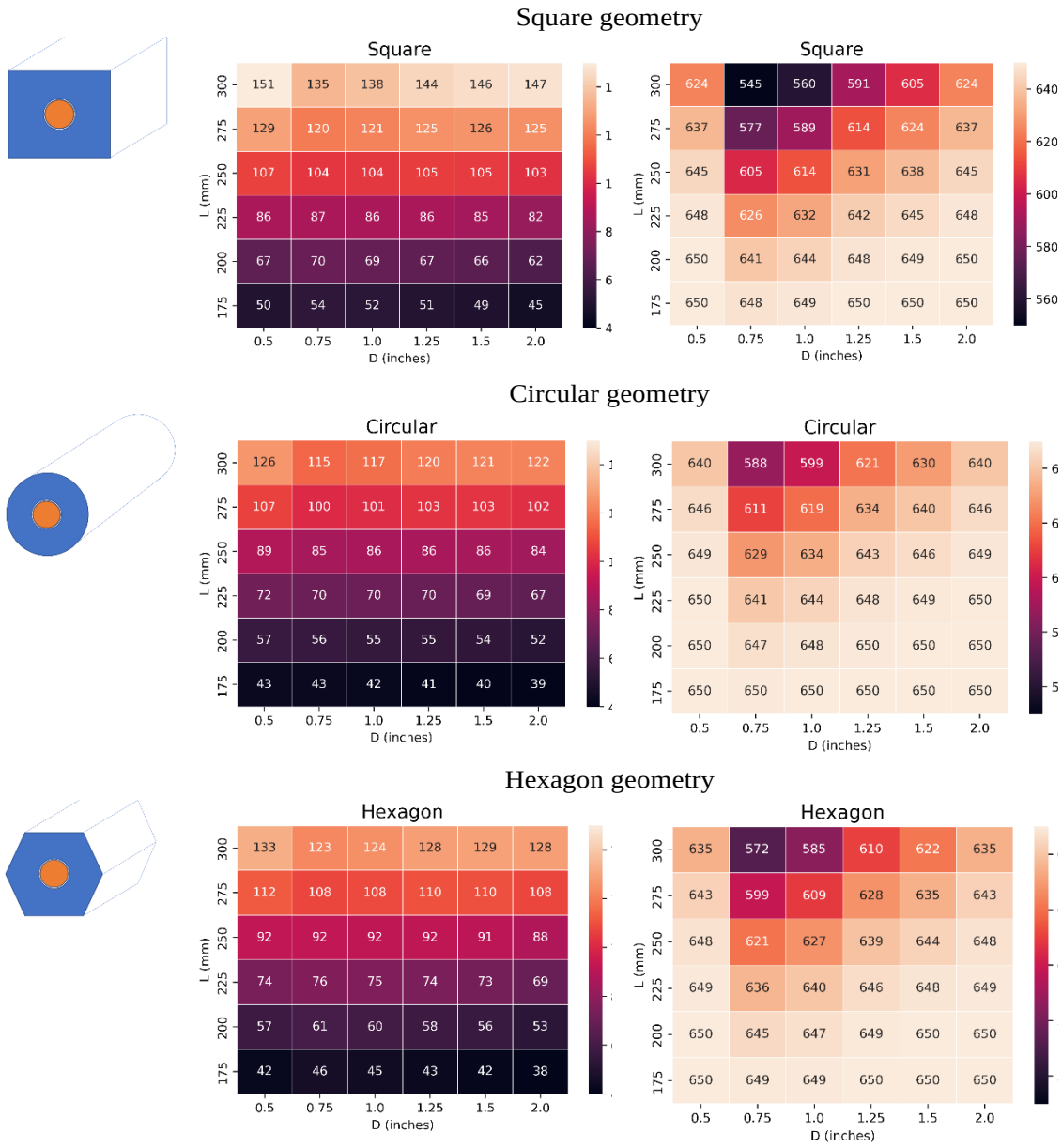

Figure 4-7. Energy stored amount and T_{avg} for different module sizes (lengths) and tube diameter (tube size).

The thermal energy storage (Qs) analysis suggests that circular geometry is less favorable. Additionally, in modular construction, voids exist between circular modules, reducing the stored energy per unit volume. Conversely, square and hexagonal geometries (Fig. 4-8) prove more suitable for modular construction and scalability, making it easier to achieve the required thermal storage capacity by adding more of these modules as needed.

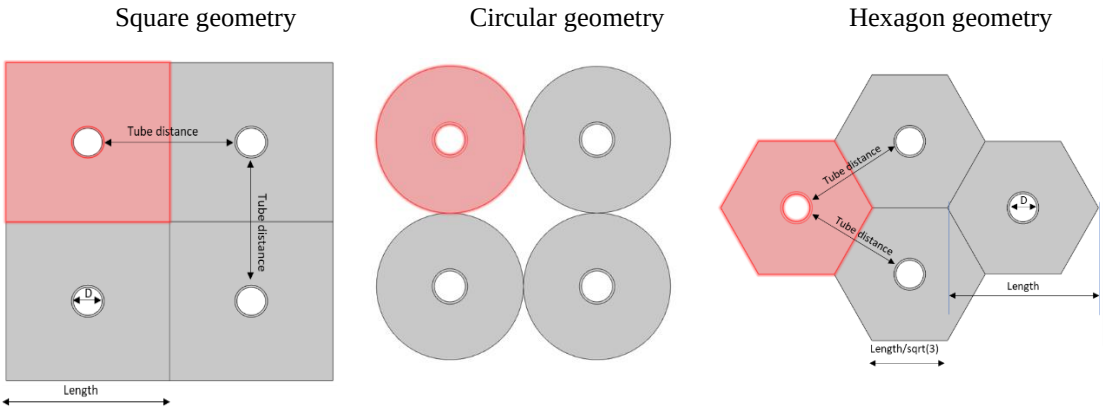

Figure 4-8. The scaled-up scheme of different designs.

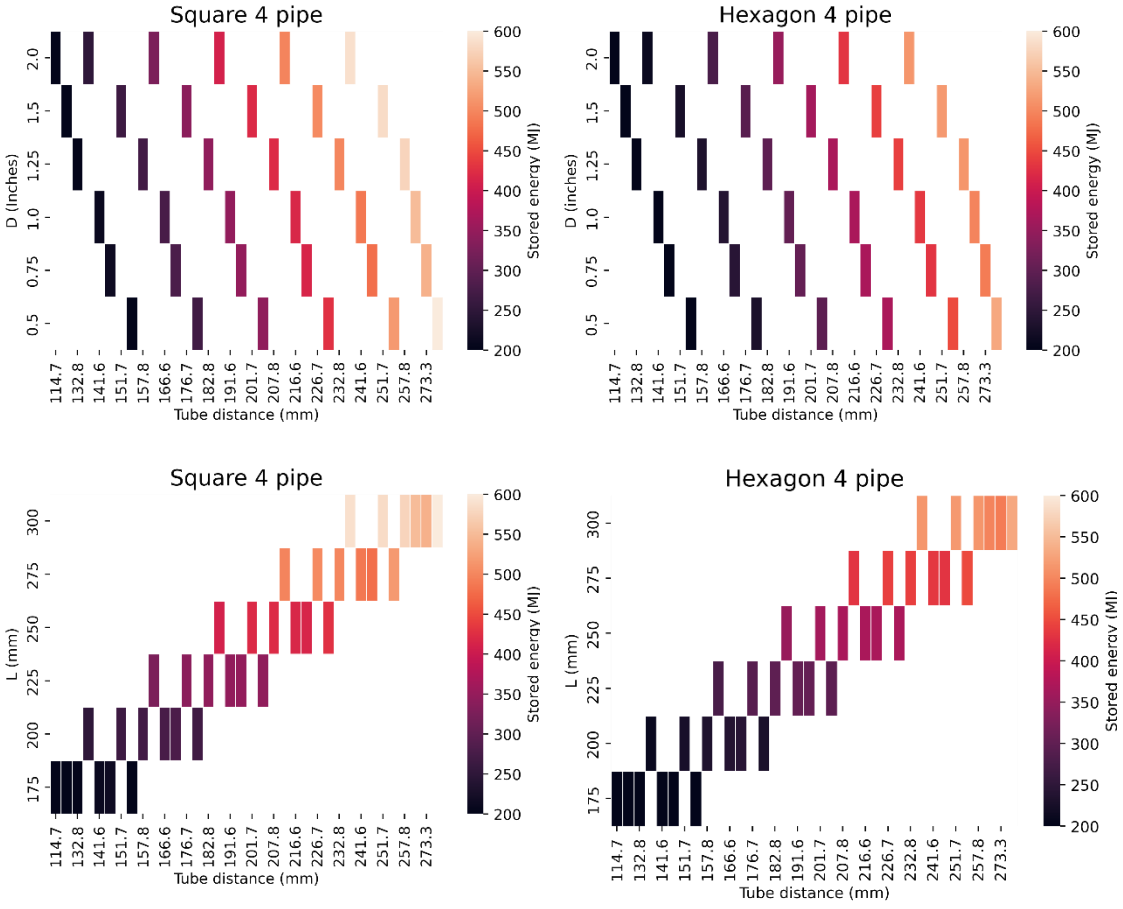

Figure 4-9. Theoretical thermal storage capacity for Square and Hexagon designs

Comparison for different module sizes (‘Length’) and tube diameter (‘Size’).

4.2.2 Effect of Tube Wall

From the results of Stage 1, the square design was selected to study the impact of air velocity on stored energy through all the cases presented in Table 4-3, including the effect of inserting or not a metallic pipe in the concrete hole. Square geometry is often preferred for TES module design due to its ease of molding and construction, as it involves fewer complex curves or angles.

This can simplify the manufacturing process, reduce material waste, and lower production costs. Additionally, square modules can be stacked or aligned more efficiently, minimizing void spaces and facilitating the assembly of larger TES systems using standardized components.

Table 4-3. Matrix of simulated cases.

Air velocity (m/s)	D (inch)	Module size (mm)
3	½	100, 150, 200, 250, 300
3	¾	100, 150, 200, 250, 300
3	1	100, 150, 200, 250, 300
6	½	100, 150, 200, 250, 300
6	¾	100, 150, 200, 250, 300
6	1	100, 150, 200, 250, 300
9	½	100, 150, 200, 250, 300
9	¾	100, 150, 200, 250, 300
9	1	100, 150, 200, 250, 300

In Figure 4-10 the obtained theoretical storage capacities and average temperatures are shown.

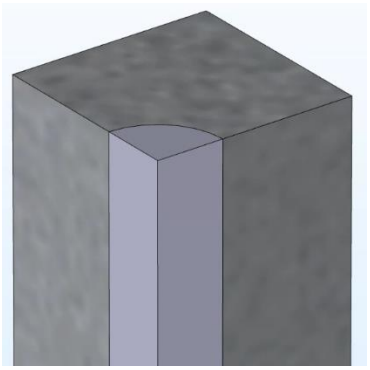

TES module without tube

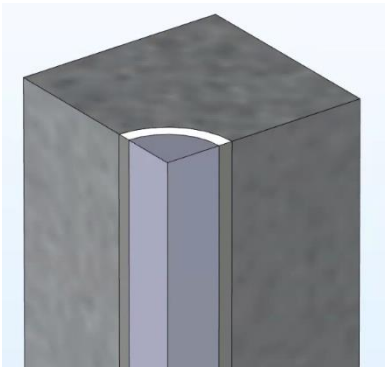

TES module with metallic tube

(A) Temperature comparison

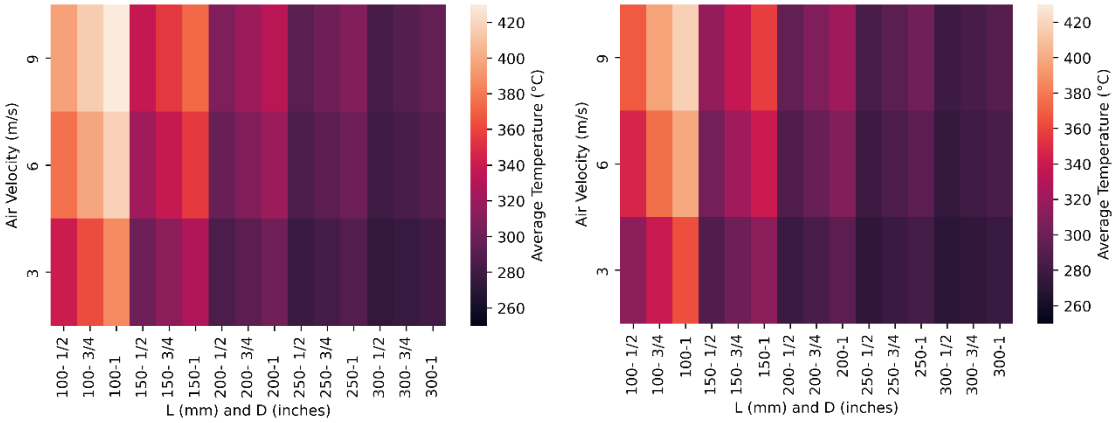

(B) Stored energy comparison

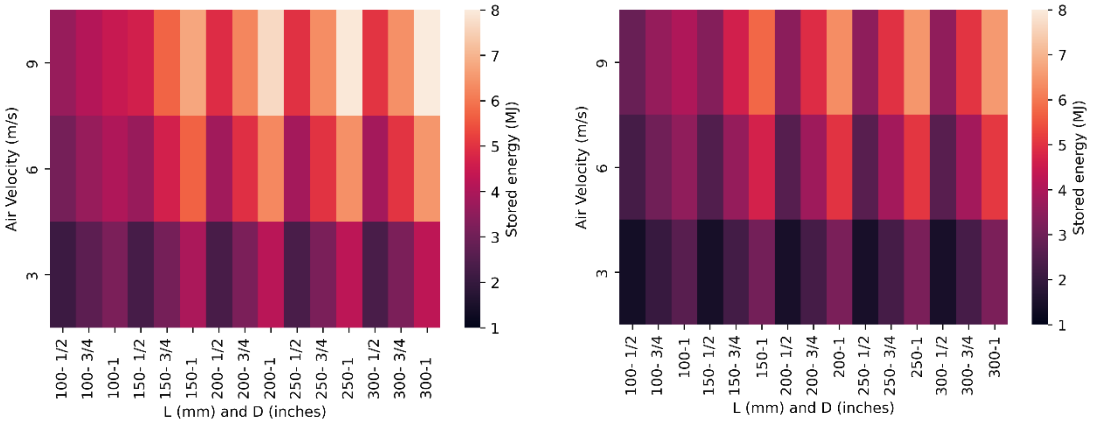

Figure 4-10. The amount of energy stored and T_{avg} per different sizes.

Average temperature (label as 'lengths'), tube diameters (label as 'Tubes') and air flow velocities.

The first input variable considered is velocity (m/s), which is assessed at three different values: 3, 6, and 9 m/s. In the case of no metallic pipe, the thermal storage capacity increases with velocity, rising from 3 MJ at 3 m/s to 5.79 MJ at 9 m/s. Similarly, in the case of with metallic pipe, the thermal storage capacity increases with velocity but to a lesser extent, from 3.11 MJ at 3 m/s to 4.6 MJ at 9 m/s.

The difference between the two cases is lowest for the lowest velocity, where it is 0.88 MJ at 3 m/s, and it increases as the velocity increases. The higher the air velocity, the better the heat transfer, so higher temperatures are achieved at the end of charge and, therefore, higher storage capacity are found (see Figure 4-11).

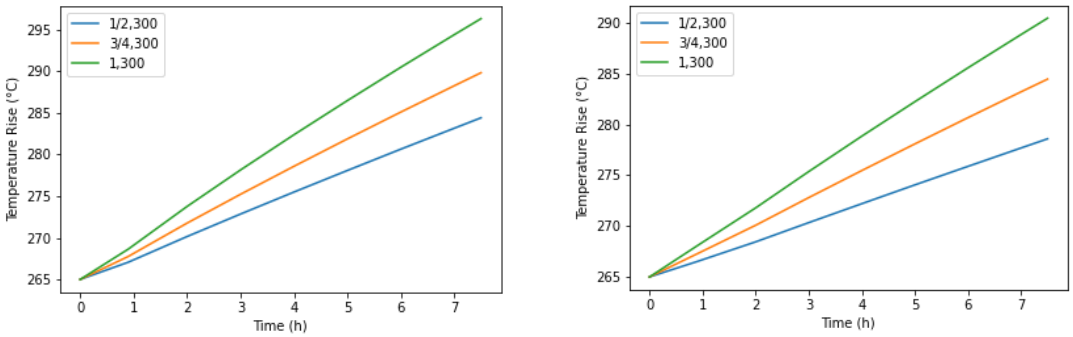

(A) (B)

Figure 4-11. The average temperature (T_{avg}) rises per air flow velocity=9 m/s.

For Length=300mm and hole/tube sizes ½,3/4 and 1 inch. (A) TES module without tube (hole) and (B) TES module with tube.

The second input variable examined is Tube diameter (inch), which is assessed at three different values: ½, ¾, and 1. In the no metallic pipe case, the thermal storage capacity increases with tube diameter, rising from 3.53 MJ for ½ inch to 5.57 MJ for 1 inch. Similarly, in the With metallic pipe case, the thermal storage capacity increases with tube diameter, but to a lesser extent, increasing from 2.43 MJ for ½ inch to 4.51 MJ for 1 inch.

The difference between the two cases is highest for the lowest tube diameter (1.1 MJ for 1/2 inch), and it decreases as the tube diameter increases. Although increasing the air flow section implies reducing the amount of mass to store the energy, the higher achieved temperatures disguise that effect (see Figures 4-12 and 4-13).

The third input variable investigated is Module size (mm), which is assessed at five different values: 100, 150, 200, 250, and 300. In the no metallic pipe case, the thermal storage capacity increases with module size, rising from 3.44 MJ for 100 mm to 4.96 MJ for 300 mm. Similarly, in the with metallic pipe case, the thermal storage capacity also increases with module size, but to a lesser extent, from 2.81 MJ for 100 mm to 3.73 MJ for 300 mm. The difference between the two cases is highest for the largest module size (1.23 MJ for 300 mm), and it decreases as the module size decreases. Here the increase in mass due to the increase of module size is the predominant effect on the storage capacity. Results on Figure 12 show that inserting a metallic pipe in the concrete hole in comparison without such insertion decreases the thermal storage capacity.

The insertion of a metallic tube in a TES module introduces an additional thermal resistance, which reduces the amount of heat absorbed and stored in the module in a specific time and transferred from an air flow with the same velocity (but different mass flow). As shown in Figure 4-13, a higher temperature rise is obtained without inserting the pipe compared to the corresponding TES module without it. The thermal resistance induced by the metallic pipe is not negligible, even at high velocities.

(A)

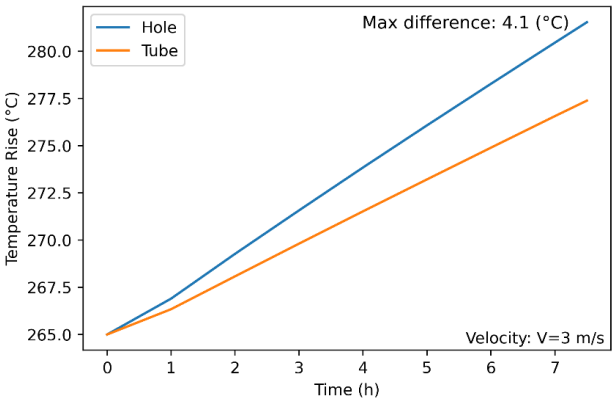

(B)

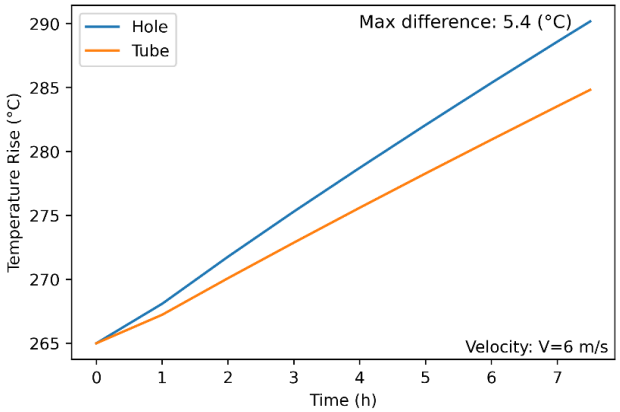

(C)

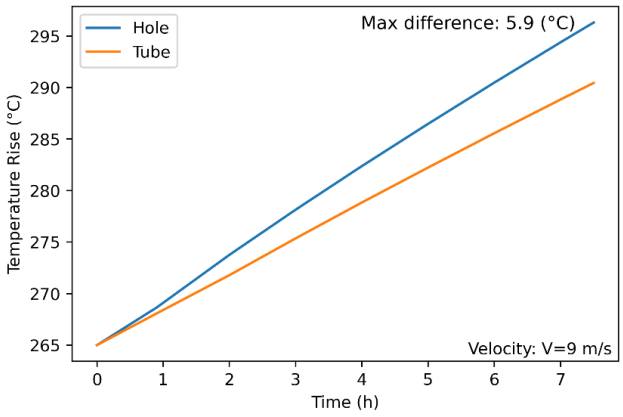

Figure 4-12. The average temperature (T_{avg}) rise.

For 1" hole/tube per different air flow velocities and for Length=300mm. (A) velocity=3 m/s, (B) velocity=6 m/s and (C) velocity=9 m/s.

These results give some support to the decision on not having a pipe when working with air as HTF, apart from the problem of thermal expansion mismatch between metallic piping and concrete. Figure 4-14 provides a visual representation of the air outlet temperature as it passes through the TES module with and without inserting a metallic pipe. Figure 4-15 (A) displays a scatter plot of the air outlet temperature for both the "hole" and "tube" cases. The results clearly indicate that the outlet temperature drops less in the "hole" case as compared to the "tube" case.

This observation is further reinforced by the comparison of the ΔT of the inlet and outlet temperature in Figure 4-15 (B), which shows that the tube case exhibits a higher ΔT. The higher ΔT in the tube case resulted in an average difference of 8% in all studied cases, however, this did not translate to a higher thermal energy storage value (Fig. 4-12 (A)) neither a higher overall heat transfer rate, Figure 16c.

The decision of whether a higher or lower ΔT is desirable depends on the specific application and desired outcome. For example, a higher ΔT may be preferable in some applications as it can lead to faster charging of the system. Conversely, for other applications, a lower ΔT may result in more efficient and controlled charging.

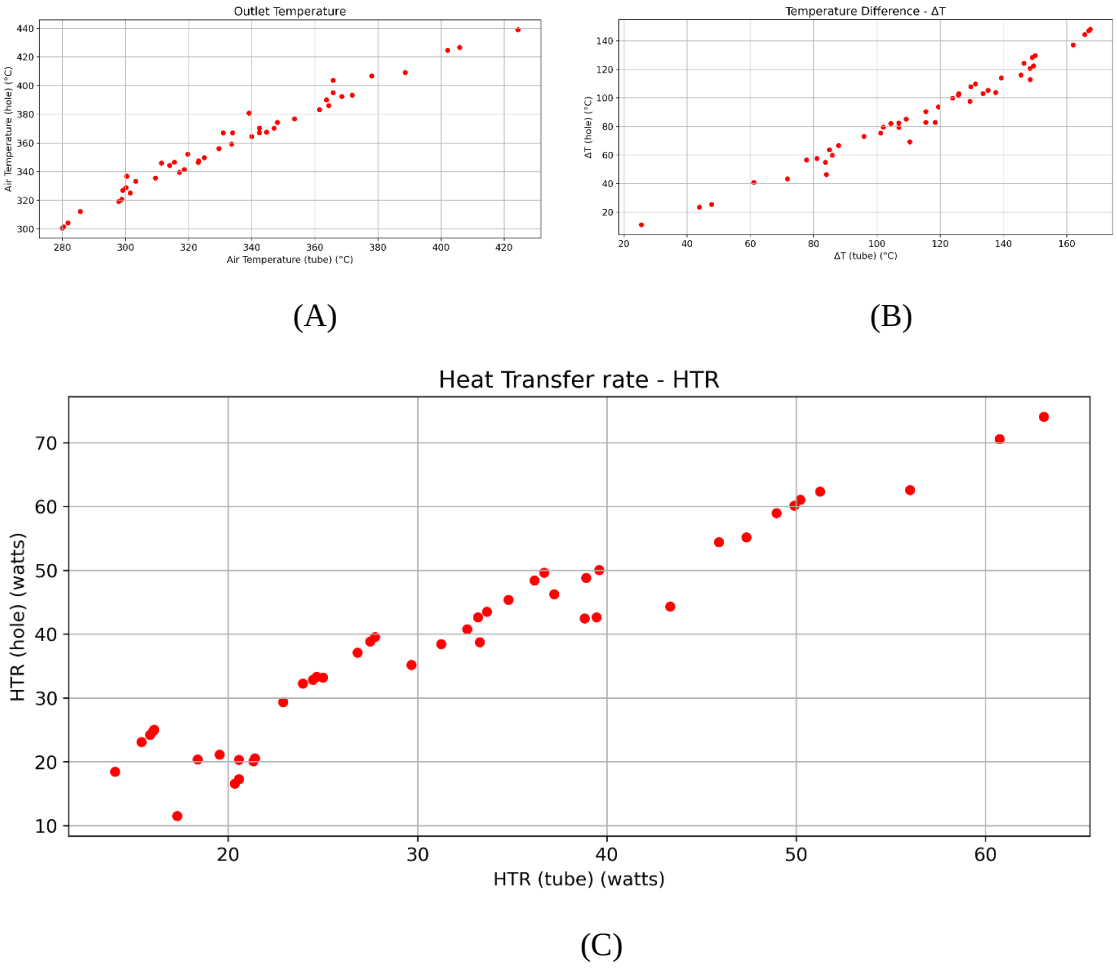

Figure 4-13. Heat Transfer Fluid (Air) Analysis for no-pipe and with-pipe cases.

(A) Air outlet temperature, **(B)** Air inlet and outlet temperature difference and **(C)** The overall heat transfer rate $\dot{Q}$ = $\dot{m}$ (kg/s) * Cp (J/kg°C) * ΔT (°C).

4.2.3 Sensitivity Analysis

Pearson's correlation coefficient equation (Sharma, 2005) is normally used to determine the relationship between variables x and y. It is denoted by the symbol "rxy" and ranges between -1 and 1, where -1 represents a lineal correlation with a negative slope, 0 represents no correlation, and 1 represents a lineal correlation with a positive slope. The equation can be written as follow:

$$r_{xy} = \frac{n\sum x_i y_i - \sum x_i \sum y_i}{\sqrt{n\sum x_i^2 - (\sum x_i)^2}\sqrt{n\sum y_i^2 - (\sum y_i)^2}}. \quad (4\text{-}3)$$

Using the equation mentioned above, where n is the number of data points, correlation matrices such as those shown in Figure 4-14 can be produced to display the pairwise correlation coefficients between different variables. From this figure, it is easy to see that air velocity has the greatest impact on the achieved Q_s , while D and L have lesser importance.

However, for T_{avg}, both air velocity and tube diameter are significant factors, and their correlation coefficients are close in value. This is especially true in the case when inserting a metallic tube since these values are even closer. L has a "negative" effect of achieved T_{avg} meaning that increasing module size will lead to less volume average temperature and less ΔT. The results of the correlation matrices align with those achieved thus far, highlighting the importance of air velocity, diameter, and module size in determining the thermal storage capacity and average temperature of the system.

In resume, the geometry scale, tube size, and air speed have a significant impact on the temperature and thermal energy storage of the thermal energy storage module. Increasing the air velocity results in higher T_{avg}. This is due to the increased heat transfer rate between the air and the thermal storage material. In contrast, increasing the length of the module leads to lower temperatures T_{avg}, with the lowest T_{avg} being seen at a length of 300 mm. The tube size also has an impact on the temperature and thermal energy storage. The 1-inch tube leads to the highest T_{avg} and thermal energy storage, followed by the 3/4 inch and 1/2-inch tubes. This is likely because the larger tubes provide more surface area for heat transfer between the air and thermal storage material. Overall, the highest T_{avg} are seen at smaller geometries and highest thermal energy storage are seen at bigger geometries which have bigger mass.

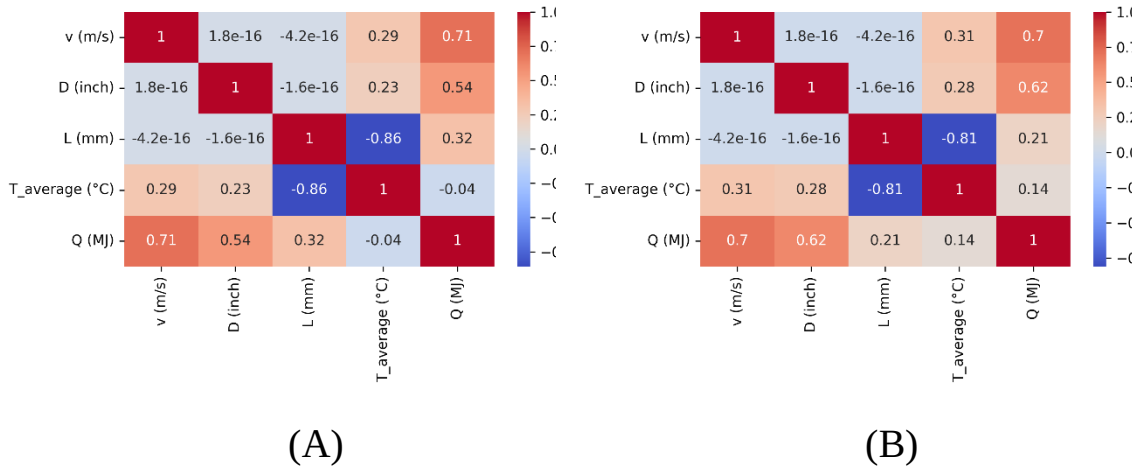

Figure 4-14. Pairwise Correlation Matrices.

(A) no metallic tube, (B) with metallic tube

The decision to go tubeless should not be taken only based on the obtained thermal performance. The interaction between the HTF and the storage material is crucial for maintaining the integrity and longevity of the TES system. In the case of concrete TES systems, the surface roughness of the concrete can significantly impact the flow of air and heat transfer. This is an aspect that has often been overlooked in previous research and warrants further investigation. Therefore, optimizing tubeless TES systems requires a comprehensive approach that considers both the benefits of eliminating thermal interfaces and the potential challenges associated with surface roughness and material compatibility. The following part of study builds on existing research and aims to further investigate the relationship between concrete surface roughness and TES performance parameters.

4.2.4 Effect of Surface roughness

Surface irregularities, also known as surface roughness (or wall roughness), have been demonstrated to have significant implications on the fluid dynamics, heat transfer rates, and overall performance of convective flow systems as well as boundary layer's characteristics, affecting the flow's turbulence, pressure drop, and heat transfer

(Achenbach, 1977; Aupoix, 2015; Kandlikar et al., 2003; Schlichting and Gersten, 2000; Taylor et al., 2006).

These irregularities induce alterations in the velocity profile, affecting surface drag, turbulent mixing, and subsequently, the heat transfer efficiency. Although surface roughness can potentially undermine system performance by increasing the pressure drop and the requisite pumping power, it can also enhance heat transfer in certain instances (Kadivar et al., 2021).

The fundamental exploration of surface roughness within turbulent flows was pioneered by scholars Hagen and Darcy (Darcy, 1857; Hagen, 1854). Their research demonstrated that the presence of surface roughness significantly elevates the pressure drop experienced by a fluid flowing over it. This elevation stems from the augmentation of drag forces and the increased flow area blockage caused by the rough surface irregularities (Darcy, 1857; Hagen, 1854). Moreover, the roughness also amplifies wall-normal functions close to the wall (Krogstad et al., 1992; Krogstadt and Antonia, 1999), thereby moderating the anisotropy of Reynolds stress (Shafi and Antonia, 1995).

Wall functions are mathematical models used in CFD to approximate the behavior of fluid flow near a wall boundary. They are typically employed in high Reynolds number flows where the boundary layer is too thin to be resolved directly by the computational grid (Versteeg and Malalasekera, 2007). These intricate dynamics between wall roughness and turbulent flow attributes were thoroughly scrutinized by researchers like Raupach et al. (Raupach et al., 1991) and Jiménez (Jiménez, 2004).

The analysis of turbulent flow over rough surfaces has been an area of keen interest, given the wide range of practical applications it covers. A commonly utilized approach to model wall roughness in industrial CFD simulations is the sand-grain method (Aupoix, 2015). The foundation of this approach lies in the concept of equivalent sand grain roughness. This is a hypothetical construct denoting the height of uniform and evenly distributed sand grains that would produce the same hydraulic resistance as the actual rough surface in question (Nikuradse, 1937).

This empirically derived method offers a robust scale of roughness that encapsulates its influence on the flow dynamics. Its uniqueness lies in its ability to provide a singular length scale that characterizes the roughness. Consequently, it allows for the

application of scaling laws in determining velocity fields and friction factors, making it a practical tool for such complex calculations.

The underlying principle of this approach involves conceptualizing the surface as being covered with a continuous layer of uniformly packed spheres, where the diameter of these spheres represents the equivalent sand-grain roughness height (k_s). This fundamental premise has been extensively explored and validated through numerous studies (Nikuradse, 1937, 1933; Schlichting, 1936). The roughness height (k_s), derived from the sand-grain method, is transformed into non-dimensional wall units (k_s+). This value becomes integral in adjusting the velocity profile and turbulence production in the cells adjacent to the wall (Spalding, 1974).

The k-ε turbulence model, explained in greater detail by authors such as Launder and Spalding (Spalding, 1974), is a way in dealing with these adjustments. In essence, these modifications help to build more accurate simulations of turbulent flows over rough surfaces. In the present study, the k-ε turbulence model is developed and deployed within the framework of COMSOL Multiphysics ("COMSOL Multiphysics® v. 6.1.," n.d.) to explore the implications of distinct concrete surface roughness levels on the air flow and heat transfer dynamics in a geopolymer-based concrete TES unit. The objective of this research endeavor is to understand these effects and to make contributions to the continuous progression of efficient and effective TES systems that utilize direct contact between concrete (or other solid mediums) and air (or other HTF).

Firstly, by considering the HTF, which in this case is air. Its behavior is governed by the continuity equation and the Navier-Stokes equations. The continuity equation ensures mass conservation and is expressed as:

$$\nabla \cdot (\rho \vec{v})_F = 0 \qquad (4\text{-}4)$$

Where 'ρ' is the HTF density and '$\vec{v}$' is the HTF velocity vector, character 'F' stands for fluid. The Navier-Stokes equation describe the momentum balance and neglecting gravitational acceleration are given as:

$$\frac{D(\rho\vec{v})_{\mathrm{F}}}{Dt} = -\nabla P + \mu_{\mathrm{F}}\nabla^2\vec{v}_{\mathrm{F}} \tag{4-5}$$

where 'P' is the fluid pressure, 'μ' is the fluid viscosity. These equations are solved concurrently to obtain velocity profiles of the air inside the TES unit. The energy equation for the heat transfer from the fluid to the concrete wall of the pipe is:

$$c_{p,\mathrm{F}}\frac{D(\rho T)_{\mathrm{F}}}{Dt} = k_{\mathrm{F}}\nabla^2 T_{\mathrm{F}} \tag{4-6}$$

Where 'c_p' is the specific heat capacity at constant pressure, 'k' is the thermal conductivity, and 'T' is the temperature. The velocities obtained from the solution of the continuity and Navier-Stokes equation are used in this equation to simulate the heat transfer. For the solid, concrete, the energy equation is used to simulate its thermal behavior, Equation 4-7. The equation is:

$$\rho_S c_{p,S}\left(\frac{\partial T_S}{\partial t}\right) = k_S\nabla^2 T_S \tag{4-7}$$

Building upon the previously discussed concepts, Figure 4-17 demarcates the Fluid, Interface, and Solid regions.

The Interface region is where the fluid (air) comes into contact with the solid (concrete). At this juncture, the equations entail the conditions of heat transfer between the fluid and the solid. These conditions ensure the continuity of temperature and heat flux at the interface, linking the fluid and solid regions. The Solid region, on the other hand, represents the concrete cylinder body. The thermal behavior of this solid region is guided by the energy equation, which captures the heat absorption, storage, and later release by the concrete.

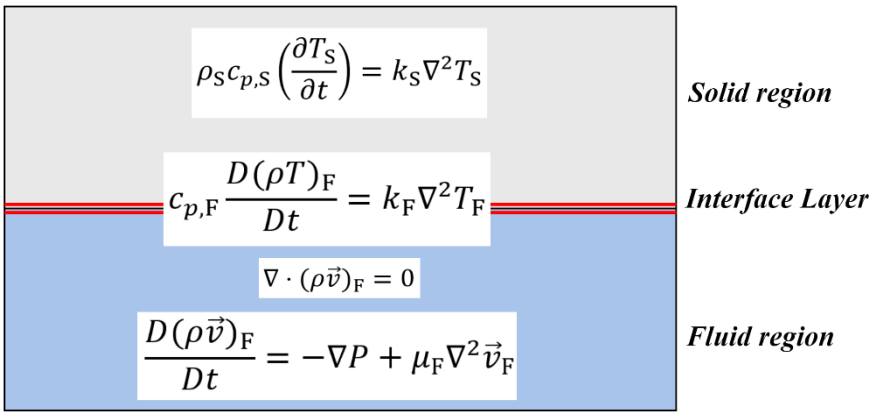

Figure 4-15. Schematic Representation of the Fluid, Interface, and Solid Region (concrete) with Corresponding Governing Equations.

The Reynolds number (see Equation 4-8) serves as an essential tool in this context. This dimensionless metric represents flow conditions and facilitates the prediction of turbulence onset. Its definition is as follows:

$$\mathrm{Re} = \frac{4\rho Q D_H}{\mu \pi D^2} = \frac{\rho v D_H}{\mu} \tag{4-8}$$

Where ρ is the fluid density, Q is the volumetric flow rate, D_H is the hydraulic diameter, μ is the dynamic viscosity, D_H is the hydraulic diameter of the pipe, and v is the mean velocity of the fluid.

A higher Reynolds number suggests the dominance of inertial forces, which promote turbulence, over viscous forces. The regime within a cylinder is given by Moody Diagram (Figure 4-16). The diagram distinguishes between laminar, transition, and turbulent flow regimes, with turbulent flow being further subdivided into smooth turbulent and rough, turbulent sub-regimes. In the turbulent flow regime, the friction factor is influenced by both Reynolds number and relative roughness of the pipe. For smooth-turbulent flow, the friction factor is primarily determined by the Reynolds number, while for rough-turbulent flow, it becomes independent of the Reynolds number and is governed by the relative roughness.

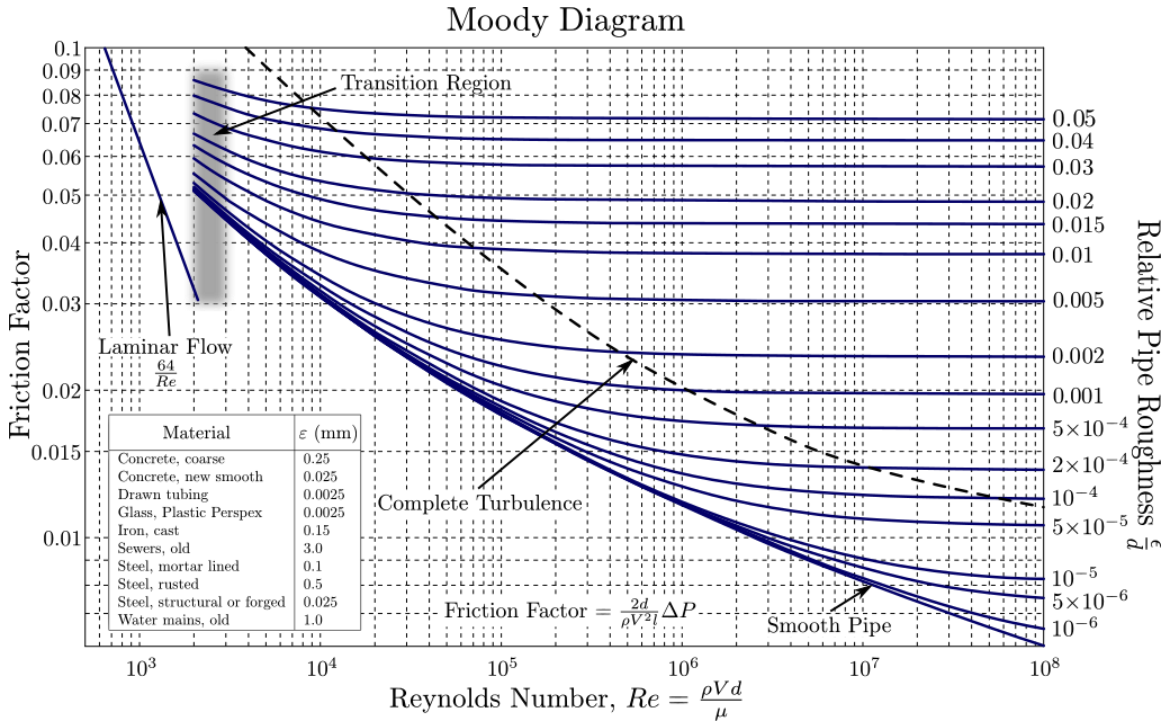

Figure 4-16. Moody Diagram for flow regime.

The chart represents the friction factor for fluid flow in a pipe as a function of the Reynolds number (Re) and the relative roughness of the pipe's inner surface (ε/D, where ε is the roughness height and D is the pipe diameter)

Turbulent flow regimes within TES systems have distinct advantages and drawbacks. On the upside, turbulence promotes fluid mixing, augmenting the heat transfer rate—an ideal characteristic for efficient energy exchange. It also ensures a uniform temperature distribution, preventing the formation of thermal inconsistencies such as 'hot-spots' or 'cold-spots'.

Nonetheless, turbulence brings challenges. Vigorous fluid movements can escalate system wear, potentially causing erosion or damage to the storage material walls and thus increasing maintenance costs. Additionally, maintaining turbulent flow often demands higher energy input, leading to increased pumping costs, partially offsetting the efficiency gains from the improved heat transfer rate. Turbulent flows might also induce vibrations and generate system noise in some instances. Thus, system design must consider both the advantages and disadvantages of turbulence to achieve a balanced solution.

4.2.5 Surface Roughness Simulation

The primary focus is to explore how the thermal performance of the TES unit is influenced by the roughness of the concrete surface. The Equivalent Sand-Grain roughness method is employed to quantify the roughness of the concrete surface. Figure 4-17 illustrates (A) the 2D and 3D schematics of random surface roughness, and (B) the 2D and 3D schematics of equivalent Sand-Grain roughness. In both (A) and (B), the upper part of the figure presents a 2D view, showing the flow U passing over the surface, while the lower part provides a 3D or perspective view of the same surface. In (B), K_s represents the height of the roughness. A numerical analysis on various Sand roughness values were conducted, which ranged from 0.3 to 3 mm.

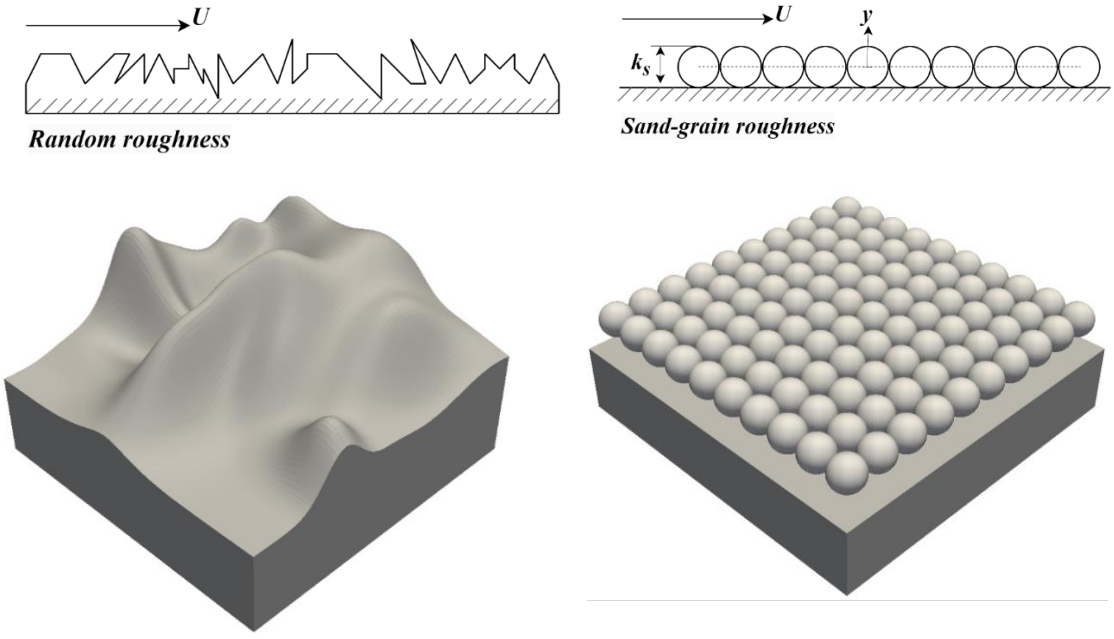

Figure 4-17. Wall roughness schematics.(A) random surface, and (B) equivalent Sand-Grain.

Turbulence models encompass sets of differential and algebraic equations, incorporating empirical constants and functions that effectively simulate the behavior of real turbulent fluids. The turbulent kinetic energy (k) and its dissipation rate (ε) are two fundamental quantities in the analysis of turbulent flows. Their evolution is governed by the respective transport equations, which describe the mechanisms of production, transport, and dissipation of turbulent energy.

The turbulent kinetic energy is defined as the average kinetic energy of the fluctuating velocity components in a fluid element:

$$k \equiv \frac{1}{2}\overline{u_i u_i}, \tag{4-9}$$

where u_i is the fluctuating component of velocity in the i-th direction. The turbulent kinetic energy equation (k-equation), describing how k is generated, transported, and dissipated, is given by:

$$\partial k/\partial t + U_j \partial k/\partial x_j = \partial/\partial x_j\left[(u + u_T/\sigma_k)\partial k/\partial x_j\right] + P_k - \varepsilon \tag{4-10}$$

The production term (P_k) represents the rate at which turbulent energy is generated from the mean velocity gradients. The turbulent eddy viscosity (ν_t) quantifies the transport of turbulent momentum across fluid elements and is given by:

$$u_t = \rho C_\mu k^2/\varepsilon \tag{4-11}$$

where μ is the molecular viscosity and C_μ is a model constant. The dissipation rate (ε) represents the rate at which turbulent energy is dissipated into heat due to viscous interactions. Its equation is given by:

$$\partial \varepsilon/\partial t + U_j \partial \varepsilon/\partial x_j = \partial/\partial x_j\left[(u + u_T/\sigma_\varepsilon)\partial \varepsilon/\partial x_j\right] + C_\varepsilon 1 \varepsilon/k P_k - C_\varepsilon 2 \varepsilon^2/k \tag{4-12}$$

The constants $C_\varepsilon 1$ and $C_\varepsilon 2$ are empirical coefficients that depend on the flow regime. The k-ε model, a widely used turbulence model, incorporates these equations along with additional closure coefficients and auxiliary relations derived from experimental data to simulate turbulent flows (Spalding, 1974; Wilcox, 1998).

Turbulent flows are characterized by complex interactions between vortices and fluid particles, resulting in a non-uniform velocity profile near solid boundaries. Accurately capturing this behavior near walls poses a significant challenge for CFD simulations. To address this challenge, wall functions are employed as computational tools to simplify the near-wall region and reduce computational cost. The logarithmic velocity profile, an empirical relationship derived from experimental data, provides a theoretical basis for wall functions. It describes the velocity distribution near a smooth wall as a function of the distance from the wall, y, and the friction velocity, u*.

Wall functions are mathematical expressions that approximate the logarithmic velocity profile and the associated turbulent shear stress near a wall. For smooth walls, the logarithmic velocity profile holds true, and wall functions can directly incorporate the logarithmic profile equation. Wall functions for rough walls can employ an equivalent sand-grain roughness approach, which introduces an effective roughness height, ks, to account for the influence of surface irregularities. The impact of wall roughness is typically accounted for by a shift factor, ΔB, in the logarithmic velocity profile:

$$u_\tau = \frac{|u|}{\frac{1}{\kappa_v}\ln \delta_w^+ + B - \Delta B} \tag{4-13}$$

This shift factor depends on the non-dimensional roughness height, k_s^+, defined as:

$$k_s^+ = \frac{\rho C_\mu^{1/4}\sqrt{k}}{\mu} k_s \tag{4-14}$$

Where, k_s is the physical roughness height. The value of ΔB varies depending on the relative size of the roughness height compared to the viscous sublayer thickness, δ (Cebeci, 2004).

Despite the inherent variability and uncertainty characterizing turbulent flow behavior, the k-ε model frequently selected as the preferred choice due to its robust capacity to manage and represent the complex interaction of variables inherent in turbulence (Spalding, 1974; Wilcox, 1998). Furthermore, the model's adaptability within the COMSOL Multiphysics platform (“COMSOL Multiphysics® v. 6.1.,” n.d.) enhances its appeal. This adaptability permits it to adjust or "tune" with wall functions and incorporate the effects of surface roughness.

The CFD model simulates a hollow cylindrical structure, as shown in Figure 4-18 (A). Figure 4-18 (B) shows the dimensions of the TES unit and the path of the HTF, in millimeters. The cylinder's body, made of concrete, serves as a solid-state storage material. Thus, the concrete cylinder functions as a TES medium, either absorbing or releasing thermal energy as the HTF circulates, depending on whether the system is in charging or discharging mode.

Here, the mesh of the CFD model is of critical importance due to the complex nature of Multiphysics. This is especially true at the boundary where the fluid interfaces with the solid material. In this region, the mesh in the fluid pass must be more refined to accurately capture the interactions that occur. A more detailed discussion of the mesh study will be presented further.

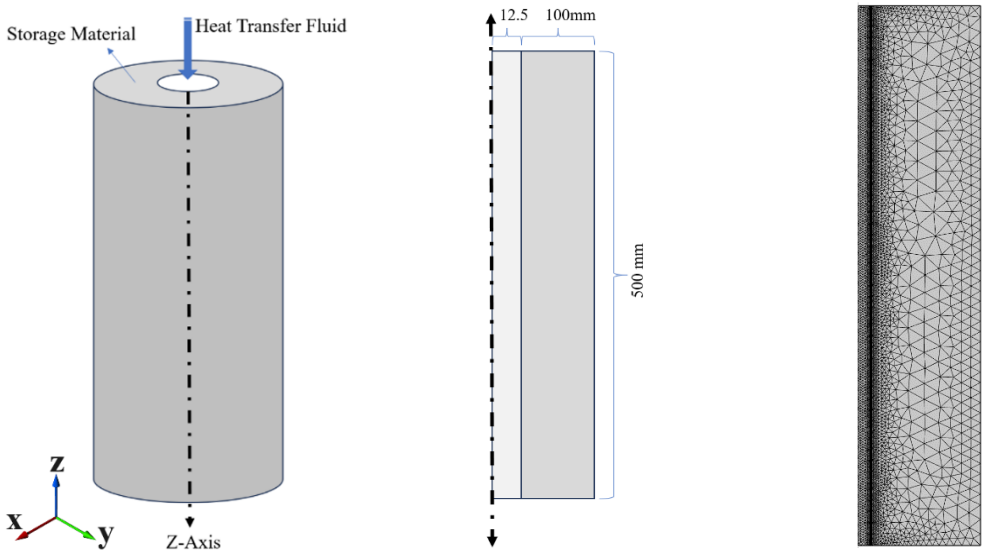

Figure 4-18. Numerical Model and Mesh for TES.

(A) Original Model, (B) 2D Axisymmetric, (C) Meshed Model

Modelling fluid flow and heat transfer processes under specific initial and boundary conditions, are outlined in Table 4-4. The initial conditions set the starting temperature and velocity of the air and storage material.

The boundary conditions define the temperature, pressure, and velocity of the air at the inlet and outlet, and also ensure no slippage of air along the walls. These conditions set the simulation's starting point (initial conditions) and establish the parameters on the system's boundary (boundary conditions (Figure 4-20).

Table 4-4. Initial and boundary conditions for TES.

Initial conditions	***At time = 0;*** $\boldsymbol{T_{\text{storage}} = T_0}$, $\boldsymbol{T_{\text{air}} = T_0}$, $\boldsymbol{\vec{v}_{\text{air}} = v_{inlet}}$
	At $time > 0$*;* $T_{\text{air}} = T_{\text{inlet}}$, $\vec{v}_{\text{air}} = v_{inlet}$
Boundary condition applicable to storage	*Adiabatic*: $k\frac{\partial T(z=0,L,t)}{\partial z} = 0$ $k\frac{\partial T(r=d_2/2,t)}{\partial z} = 0$
Boundary condition applicable to air	*At* $Z = 0$*; Inlet* $v(r = d_1, z, t) = v_{air}$, $T_{\text{air}}(r = d_1/2, z, t) = T_{\text{inlet}}$, $P(r = d_1/2, L, t) = P_{atmospheric}$
	At $Z = L$*; Outlet* $P = p_{\text{out}}$ *At* $r = d_1/2$*; No slip condition* $v(x,t) = 0$

In executing the CFD and numerical analysis, the following assumptions were established:

1. The concrete material utilized in the energy storage system is assumed to be homogeneous and isotropic, providing uniformity and consistency throughout.
2. The energy storage system module is considered to be thoroughly insulated, negating any significant heat losses to the surrounding environment.
3. The heat transfer fluid (HTF) flow was postulated to exhibit turbulent characteristics.

4. Additionally, the HTF considered incompressible and Newtonian, simplifying the analysis by ascribing it standard fluid properties.

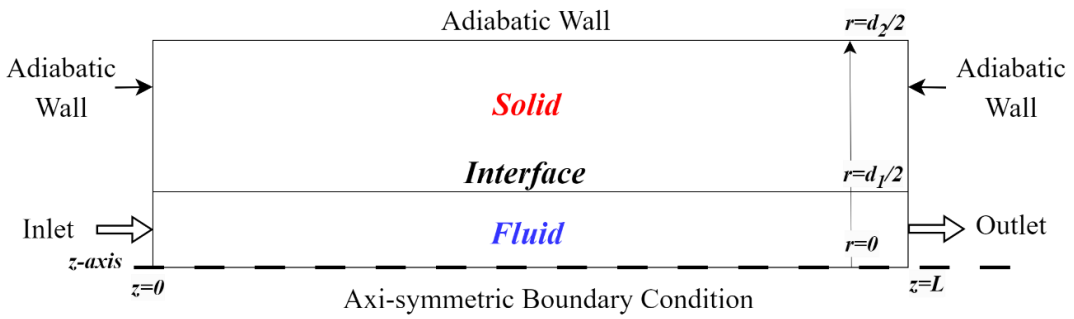

Figure 4-19. Schematic Diagram of the Two-Dimensional Axisymmetric Model with Associated Boundary Conditions.

In the selected simulation scenario, an air inflow with a specific inlet velocity of 20 m/s and pressure of 1 bar is considered. The diameter of the system's hollow core is 25 mm, leading to a Reynolds number of 7081.28. This Reynolds number exceeds the critical value for laminar flow, Moody Diagram of Figure 4-16, indicating the presence of turbulent flow.

As for simulation accuracy insurance, a parametric analysis of the mesh was conducted, focusing on a detailed mesh convergence analysis. The goal was to strike a balance between computational efficiency and solution accuracy. To achieve this, a study across six different meshes, as shown in Table 4-5, was conducted. This table presents the results of the parametric study, detailing the resolution of the computational mesh, defined by the number of vertices (simulation nodes) and elements (mesh cells).

The quality of the mesh elements is also evaluated, with higher quality meaning more uniform, regular cell shapes which yield more accurate solutions. The 'Average Element Quality' scores suggest that the quality of the elements generally improves as the mesh resolution increases, although the Ultra Fine mesh shows a slight dip in quality compared to the Finer mesh.

The transient analysis was conducted across all mesh types to assess their impact on the thermal system. This transient study spanned a duration from 0 to 90 seconds, examining only 100 mm of the cylinder to reduce computational costs. The starting temperature of the air inflow was set at 450 °C. Concurrently, the TES unit, embodied by the concrete body of the cylindrical system, sustained an initial temperature of 200 °C.

Table 4-5. Parameters and quality of each mesh type studied.

Mesh Resolution	Coarse	Moderate Coarse	Medium	Fine	Finer	Ultra Fine
Mesh Vertices	148	203	350	501	759	1774
Number of elements	196	285	524	784	1245	3024
Average Element Quality	0.777	0.8344	0.8407	0.8523	0.8493	0.8273

The mesh study examined parameters such as the absolute total heat flux and the average temperatures at both the contact line and the HTF exit, as illustrated in Figure 4-20. Table 4-6 compares the simulation results for different mesh resolutions. Results reveal that the Absolute Total Heat Flux, exhibit a high degree of similarity across all mesh resolutions. This indicates that variation in resolution does not substantially impact the model's overarching heat transfer characteristics. This is a promising outcome as it enables computational efficiency without significantly compromising the outlet heat flux accuracy.

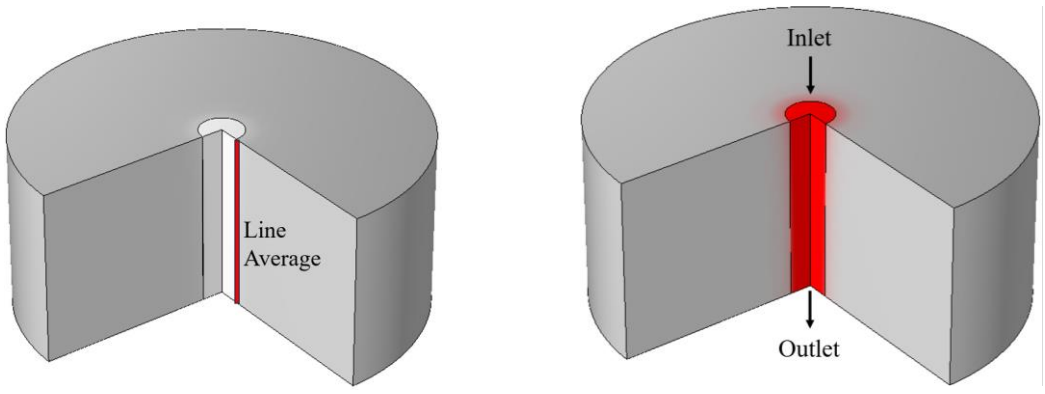

(A) (B)

Figure 4-20. (A) Average Temperature Line Evaluation (°C), and (B) Absolute total heat flux (W/m2) and Temperature (°C) at the exit of heat transfer fluid.

The flux values differ by only 0.83%, from 4.1693×10^5 W/m^2 at the 'Coarse' resolution to 4.1346×10^5 W/m^2 at the 'Ultra Fine' resolution.

The 'Contact Line Average Temperature (°C)' progressively increases as the mesh resolution refines, peaking at 316.43°C for the 'Finer' resolution before marginally decreasing to 316.36°C for the 'Ultra Fine' resolution. This shift represents a maximum variation of 0.96% from the 'Coarse' to the 'Finer' resolution. The 'Outlet HTF Temperature (°C)' remains notably consistent across all mesh resolutions, with negligible fluctuations. The temperature varies from 430.49°C at the 'Coarse' resolution to 430.42°C at the 'Ultra Fine' resolution, a variation of only 0.02%.

Table 4-6. Simulation results for mesh study (end of simulation = 90 seconds)

Mesh Resolution	Coarse	Moderate Coarse	Medium	Fine	Finer	Ultra Fine
Absolute total heat flux, z component (W/m^2), *10^5	4.1693	4.1693	4.1486	4.1455	4.1426	4.1346
Contact line average temperature (°C)	313.42	313.89	316.02	316.37	316.43	316.36
Outlet HTF temperature (°C)	430.49	430.49	430.52	430.52	430.51	430.42

The 'Fine' or 'Finer' mesh resolutions seem to offer the optimal balance between computational efficiency and solution accuracy. They offer high Average Element Quality; relatively low computational expenditure compared to the 'Ultra Fine' resolution and deliver precise readings for both heat flux and temperature metrics.

The selected mesh, 'Fine', was then used in examining the effect of timesteps. Timesteps of 0.1, 0.4, 0.7, and 1 second were evaluated to further optimize the model's accuracy and efficiency. Table 4-7 demonstrates the insignificant impact of varying timesteps on the simulation results. The 'Temperature (°C) Contact Line' values remain relatively constant, varying by a mere 0.02% from 316.37°C at timesteps of 0.1, 0.4, and 1 second to 316.31°C at a timestep of 0.7 seconds.

Similarly, the 'Temperature (°C) Outlet' demonstrates minor fluctuations, with a variation of less than 0.002% between the maximum temperature of 430.52°C (at timesteps of 0.1, 0.4, and 1 second) and the minimum temperature of 430.51°C (at a timestep of 0.7

seconds). The 'Heat Flux (W/m^2)' values also exhibit minimal variations across the differing timesteps. All timesteps display values around $4.1455x10^5$ W/m^2, with a slight decrease to $4.1449x10^5$ W/m^2 at a timestep of 0.7 seconds. This represents a negligible variation of approximately 0.01%. These results suggest that timesteps within the range of 0.1 to 1 second do not significantly impact the model's output metrics. Therefore, using a larger timestep such as 1 second can help to improve the computational efficiency of the model without significantly affecting its accuracy.

Table 4-7. Simulation results for timesteps effect (end of simulation = 90 seconds).

Mesh	Time steps (s)	Temperature (°C)		Heat Flux (W/m^2)·10^5
		Contact Line	Outlet	Outlet
Fine	0.1	316.37	430.52	4.1455
	0.4	316.37	430.52	4.1455
	0.7	316.31	430.51	4.1449
	1	316.37	430.52	4.1455

It is important to acknowledge that COMSOL Multiphysics' inherent capability to adjust and manage timesteps according to the problem's requirements can also influence the results. This feature can adaptively refine or coarsen the timestep depending on the problem's complexity, contributing to both the accuracy and computational efficiency of the simulation.

4.2.6 Numerical Results

In Table 4-8 the effect of surface roughness on fluid dynamic parameters after 10 hours of charging is presented. This table collates the average parameters recorded along the z-axis of the wall at the point of contact with the HTF, Figure 4-20 (A). These parameters are obtained from simulations conducted with five different roughness levels: 0 mm, 0.3 mm, 1 mm, 2 mm, and 3 mm, all under the same conditions discussed in the preceding sections. The simulation time for each was 600 minutes (10 hours) to charge the TES unit, maintaining an air velocity of 20 m/s and an inlet temperature of 450 °C. There, it can be seen that a distinct increase in friction velocity corresponds with an escalation in

surface roughness. For a smooth surface (0 mm roughness), the friction velocity is 1.1842 m/s. This value experiences a rise of roughly 30.2%, reaching 1.5635 m/s when the surface roughness is increased from 0.3 mm to 1 mm. Further adjustments in roughness to 2 mm and 3 mm yield smaller increases in friction velocity, of about 18.7% and 7.6% respectively. This pattern appears to present a diminishing return in terms of friction velocity, potentially due to the turbulent characteristics of the fluid flow at higher levels of roughness.

In contrast, both the shear rate and vorticity magnitude are seen to decline as surface roughness increases. The shear rate witnesses a decrease of approximately 33.5% with a transition in roughness from 1 mm to 2 mm, followed by a further decrease of 22.4% as roughness reaches 3 mm. A similar pattern is observed for the vorticity magnitude, with reductions of approximately 31.6% and 21.2% recorded when roughness increases from 1 mm to 2 mm, and 2 mm to 3 mm, respectively. Pressure, conversely, demonstrates a consistent increase as surface roughness elevates, with an approximate growth of 61.3%, 34%, and 15.3% when transitioning from 0.3 mm to 1 mm, 1 mm to 2 mm, and 2 mm to 3 mm in roughness, respectively.

Table 4-8. Effect of surface roughness on fluid dynamic parameters after 10 hours of charging the TES unit.

Roughness	Friction velocity	Shear rate	Vorticity magnitude	Wall roughness in viscous units	Pressure
(mm)	(m/s)	(1/s)	(1/s)	(1)	(Pa)
Smooth (0)	1.1842	5359.9	5358.3	0.00	41.326
0.3	1.2005	6015.6	6013.8	7.3348	46.964
1	1.5635	5996.6	5993.7	32.383	75.633
2	1.8559	4102.2	4099.1	76.327	101.34
3	1.9970	3179.9	3176.7	122.10	116.98

The no-slip condition sets the fluid velocity to zero at solid surfaces. So, the velocity will be at the minimum (zero) in the layer of elements directly adjacent to the wall boundary. Figure 4-22 shows the evolution in velocity along the flow pipe. Starting with a smooth surface, velocities fluctuate between 12.70 m/s near the wall to a maximum of 23.77 m/s in the central and downstream regions. Near the wall suggest the elements with

height up to around 2 mm from the boundary are significantly influenced by the no-slip condition before velocities increase rapidly away from the wall. A marginal roughness of 0.3 mm sees the velocity close to the wall slightly decrease to 11.96 m/s, while the maximum velocity in the central and downstream sections exhibits a minor increment to 24.23 m/s.

With a further increase in roughness to 1 mm, the wall-adjacent velocity drops by roughly 8.7% to 10.92 m/s. In contrast, the central and downstream maximum velocity records an increase of approximately 6.2%, reaching 25.74 m/s. When the roughness level is heightened to 2 mm, the velocity close to the wall experiences a roughly 10.9% increase to 12.11 m/s, and the maximum velocity elevates by a smaller rate of about 3.4%, amounting to 26.61 m/s.

For the maximum roughness level of 3 mm, the wall-adjacent velocity marks an approximate 7.9% increase to 13.07 m/s. However, the maximum velocity in the central and downstream regions sees only a marginal rise of about 0.3%, peaking at 26.7 m/s. The maximum velocity difference between the smooth surface and the 3 mm rough surface is 2.93 m/s, as depicted in Figure 4-21.

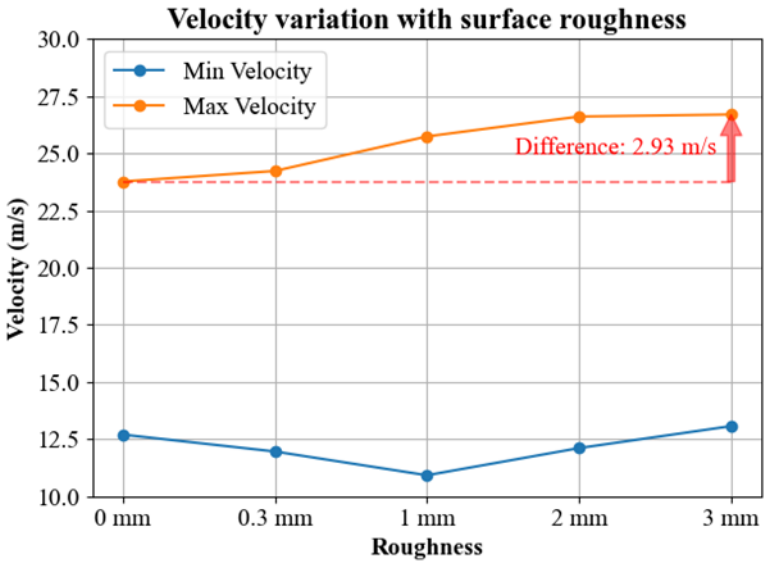

Figure 4-21. Minimum and maximum velocities observed along the flow pass.

These observations illustrate a consistent pattern where both the wall-adjacent minimum and central and downstream maximum velocities increase with the increase of surface roughness. Nevertheless, the increment rate exhibits a steady decline, suggesting that the impact of surface roughness on fluid flow velocity may follow a pattern of diminishing returns as roughness increases. Near the wall, the effect of roughness creates a buffer layer, increasing the local turbulence, and thus decreasing the near-wall velocity. As the flow moves away from the wall, the effects of wall roughness reduce, and the impact of turbulence becomes more prominent, enhancing momentum exchange and leading to increased velocity at the center and downstream, see Figure 4-22. The flow direction is indicated from left to right, and the different panels (A through E) show the impact of increasing roughness on the flow pattern within the pipe. Panel A represents an ideally smooth surface with no roughness, while panels B through E depict increasing roughness levels from 0.3 mm to 3 mm. As the roughness increases from panel B to E, we observe more disturbances in the flow, with the blue regions indicating higher velocities and the red regions indicating lower velocities due to the presence of turbulent eddies.

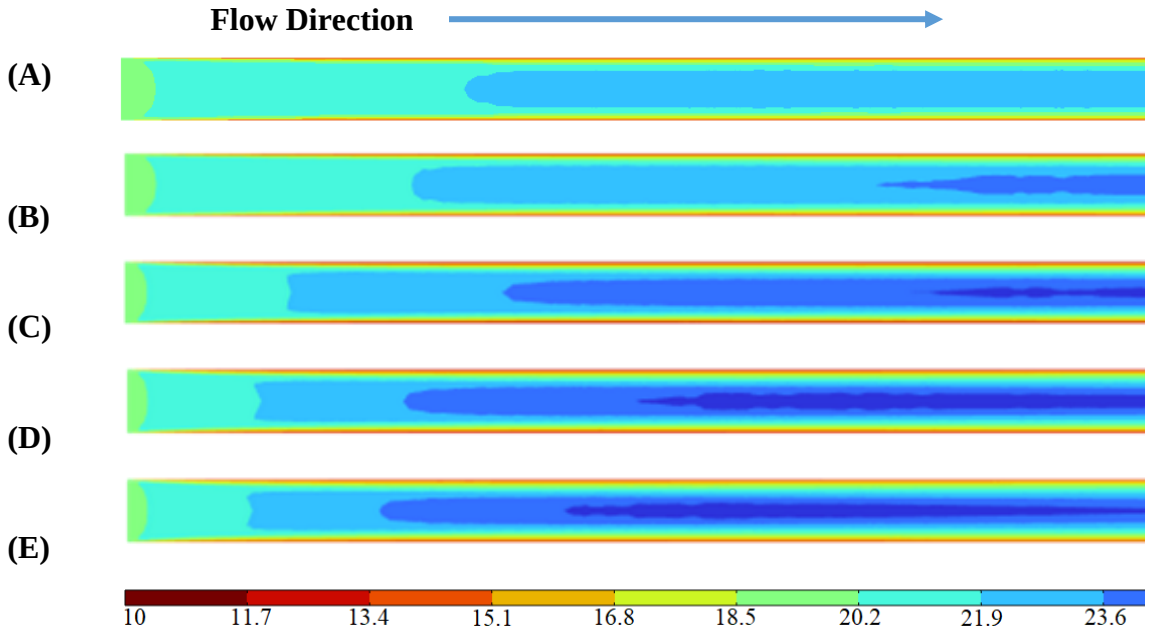

Figure 4-22. Velocity Streamlines for Different Levels of Surface Roughness.

.(Velocity unit: m/s) (A) Ideally smooth surface (0 mm roughness), (B) 0.3 mm, (C) 1 mm, (D) for 2 mm, (E) 3 mm .

The evaluation of pressure profiles in this study further substantiates the considerable effect of surface roughness on the pressure distribution within the system. In accordance with fluid dynamics principles, a higher degree of surface roughness contributes to increased friction losses, which manifest as an increase in pressure drop. For an ideally smooth surface (zero roughness), no pressure drop is observed due to the absence of friction losses.

Upon assessing other four distinct levels of surface roughness, a positive correlation between the surface roughness degree and the entrance pressure is revealed. This means, as surface roughness escalates, so does the entrance pressure, indicating a higher-pressure requisite to initiate and sustain fluid flow in the system. A lesser degree of increase is also observed in the outlet pressure with the rise in surface roughness. This minor increment suggests a potential gradual equalization of pressure as the fluid flows through the system and a diminishing effect of roughness near the outlet, possibly owing to a more stabilized flow.

To quantify the observed pressure drops, the following data is provided:

- A surface roughness of 0.3 mm incurs a pressure drop of 101.97 Pa.
- Expanding the surface roughness to 1.0 mm leads to a pressure drop rise by approximately 62%, reaching 163.26 Pa.
- Enhancing the surface roughness to 2.0 mm culminates in a further pressure drop to 214.03 Pa, denoting an increase of around 31% from the 1.0 mm case.
- At the maximum roughness level of 3.0 mm, the pressure drops peaks at 242.78 Pa, representing a relatively smaller increment of about 13.4% from the 2.0 mm roughness scenario.

There is a consistent trend of rising pressure drop with the escalation in roughness: from 101.97 Pa at 0.3 mm roughness to 242.78 Pa at 3.0 mm roughness. This denotes a substantial increase of nearly 138% equal to ~140 Pa.

The thermal consequences of surface roughness within the system are visually presented in Figure 4-23. This figure displays the HTF temperature along the centerline of the flow path for five distinct levels of surface roughness at the simulation's conclusion.

Starting with a smooth surface (0 mm roughness), the entrance temperature begins at 450 °C and ends with an outlet temperature of 441 °C. This equates to a ΔT of 9 °C, indicating a moderate heat transfer rate from the HTF to the system, predominantly to the concrete components of the thermal energy storage unit.

In the case of a slight roughness of 0.3 mm, the outlet temperature decreases marginally to 440.7 °C (ΔT of approximately 9.3 °C). When the roughness is further increased to 1 mm and 2 mm, the outlet temperatures are noted to be 439.4 °C and 437.5 °C, respectively. The maximum roughness level of 3 mm records the lowest outlet temperature of 436.3 °C, reflecting a larger ΔT of around 13.7 °C. This growing ΔT suggests a stronger temperature gradient between the HTF and the system surface with each increase in roughness. This intensified temperature gradient results in a more vigorous heat transfer from the HTF to the storage material.

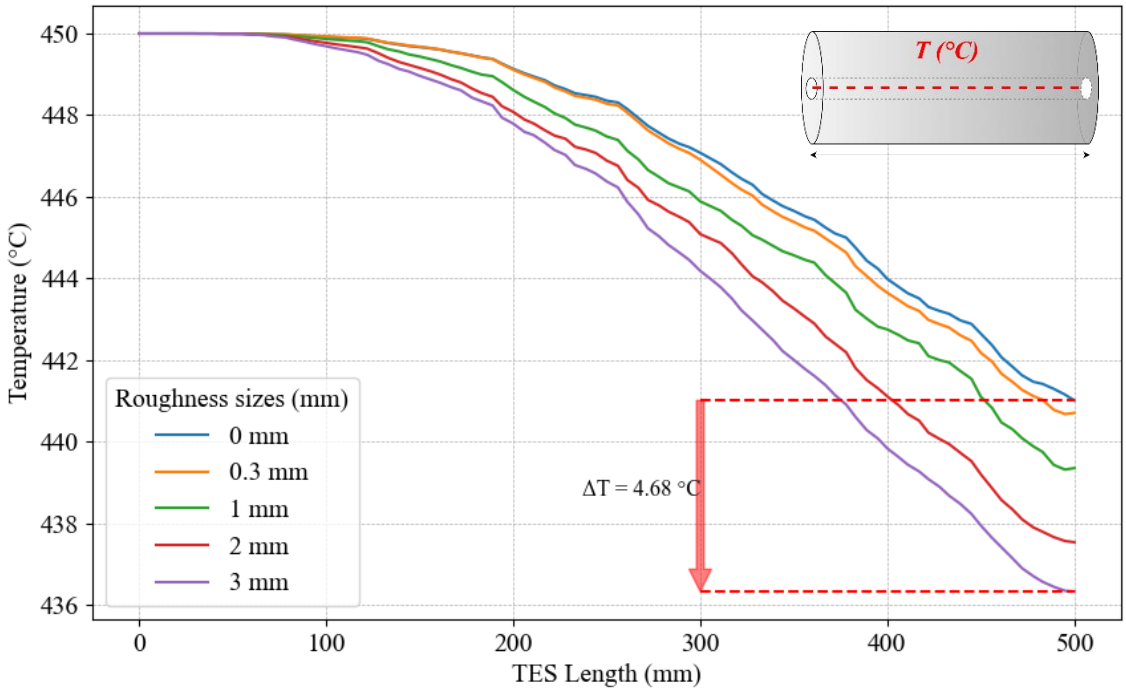

Figure 4-23. Variation of HTF temperature along the centerline flow path for different surface roughness conditions at the end of the simulation.

The temperature contours illustrated in Figure 4-24 provide an axi-symmetric view of the temperature distribution within the TES unit, further strengthening the insights gathered from previous observations. Notably, these contours highlight how changes in surface roughness influence the heat transfer dynamics within the TES system. In all cases, it is clear that the hollow, denoted by the highest temperature, illustrates distinct variations in heat distribution across different surface roughness conditions.

Evident in the contours, higher levels of surface roughness appear to enhance the heat dispersion throughout the system. This is likely due to an increase in surface area and turbulence that comes with increased roughness, amplifying the convective heat transfer between the HTF and the surrounding solid. As a result, a lower temperature gradient in the solid and a higher HTF input-output temperature difference are noted, reflecting a more effective and faster heat exchange.

In resume, higher surface roughness generally equates to a larger HTF input-output temperature difference, increased friction velocity and pressure drop. The results suggest that surface roughness can be used to optimize the thermal performance of TES systems. By understanding the complex relationship between surface roughness, velocity, pressure, and temperature, it is possible to manipulate these parameters to improve the system's efficiency.

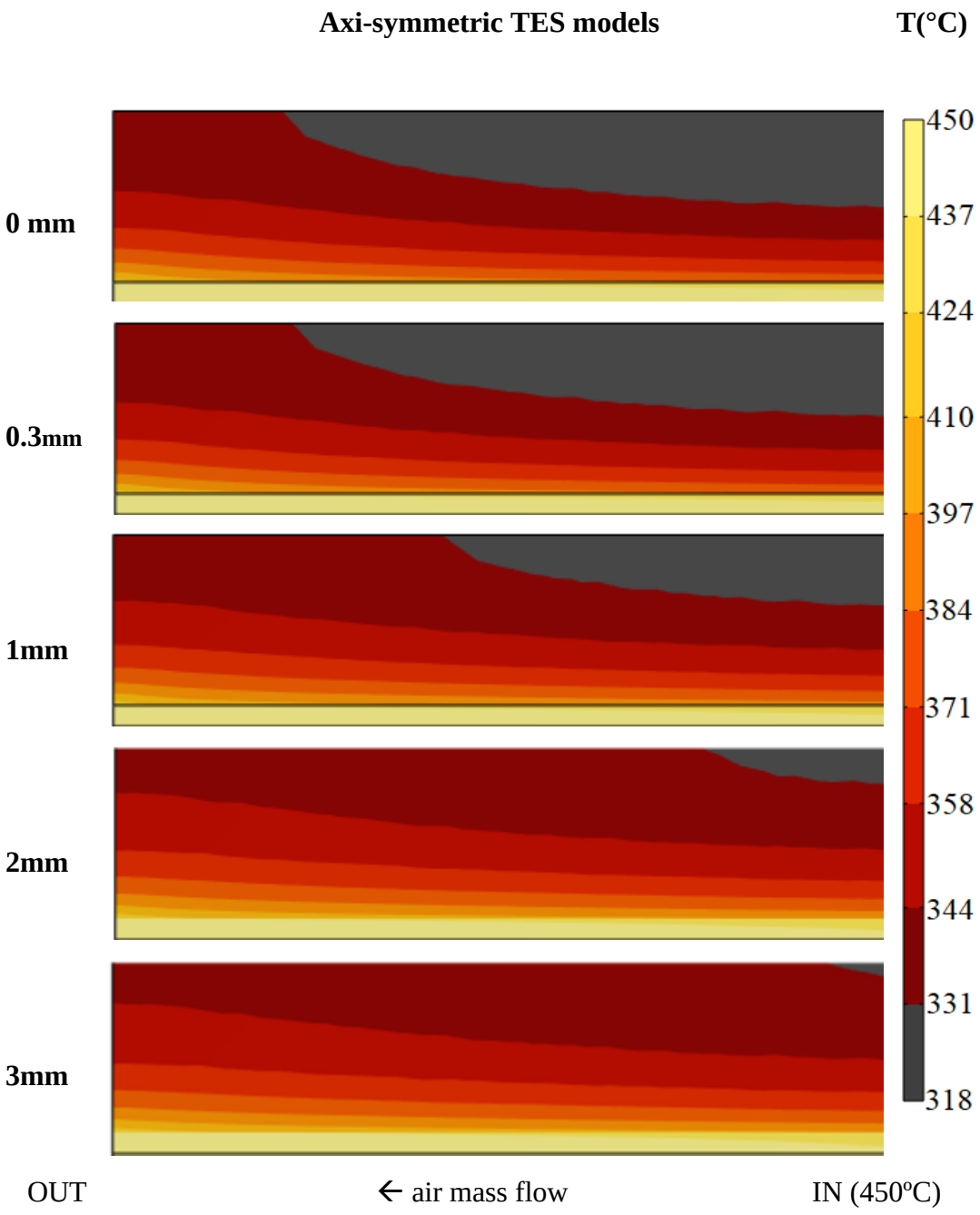

Figure 4-24. Axi-symmetric temperature distribution in the TES unit for different surface roughness conditions at the end of the simulation (10 hours)

Nonetheless, achieving an optimal balance between the pressure drop instigated by surface roughness and the escalated heat exchange rate is a focal aspect in practical application contexts. The calculated parameters such as charging efficiency, HTF outlet heat transfer rate, and energy stored during charging (as defined by equations 4-15 to 4-

17) indeed serve as benchmarks for optimization efforts. It is assumed that there are no thermal losses to ambience.

$$Q_{storage}(t) = \rho_S V_S C_{p,S}(< T_{TES}(t) > - T_{init}) \quad (4\text{-}15)$$

$$\dot{Q}_{storage}(t) = \dot{m} C_{p,F}\left(T_{F,avg}(t) - T_{inlet}\right) \quad (4\text{-}16)$$

$$\eta_{charge} = \frac{< T_{TES}(t) > - T_{init}}{T_{inlet} - T_{init}} \quad (4\text{-}17)$$

In these equations, the average temperature of the solid element, $<T_{TES}>$, is considered to be a representative of its temperature distribution performance. Symbols t, ρ, and Cp respectively refer to time, density, and the heat capacity of 'solid' and 'fluid', this last one as indicated by the subscript and 'F'.

From the data delineated in Table 4-9, the correlations between surface roughness and the performance metrics are apparent. With respect to charging efficiency, an upward trend can be observed as surface roughness escalates. The efficiency increases from 53.6% in the perfectly smooth case to 57.9% in the system with a surface roughness of 3 mm. This represents an approximate increase of 7.4% in efficiency. The HTF outlet heat transfer rate also manifests a similar ascending trend.

When the surface roughness is at its minimum, i.e., 0 mm, the heat transfer rate is 183.78 W. However, this value increases substantially with surface roughness, reaching up to 279.43 W when roughness is at its peak at 3 mm. This represents a notable increase of approximately 52.0% compared to the initial case, corroborating the earlier assertions that an increase in surface roughness enhances heat exchange due to increased turbulence.

Lastly, the trend in the energy stored during charging also rises with surface roughness. The energy stored ascends from 77.4 MJ in the case of zero roughness to 83.7 MJ at a 3 mm roughness, marking an increase of about 8.1%. These results mean that for storing the same amount of energy, it would be required a volume of a TES unit with 3mm roughness of around 92% lower than the TES unit having an ideal smooth surface.

Table 4-9. Charging Efficiency, HTF Outlet Heat Transfer Rate, and Energy Stored During Charging for Different Surface Roughness Conditions. (at the end of simulation)

Roughness	Charging Efficiency	HTF Outlet Heat Transfer Rate	Thermal Energy Stored
(mm)	(%)	(W)	(MJ)
0	53.6%	183.78	77.4
0.3	53.8%	190.00	77.8
1	55.7%	217.67	80.4
2	57.4%	254.80	83.0
3	57.9%	279.43	83.7

In conclusion, this study has tried and illustrated the influence of surface roughness on the fluid dynamic and thermal parameters within a TES system. As expected, the computational investigation revealed a clear relationship between surface roughness and the friction velocity, shear rate, vorticity magnitude, pressure, and temperature. The study has quantified how the increased surface roughness results in a rise in friction velocity and pressure, while leading to a decrease in shear rate and vorticity magnitude. Furthermore, the thermal analysis denotes an amplified heat transfer between the HTF and the system as the roughness increases.

The results underscore the potential to enhance thermal performance and overall efficiency of TES systems by manipulating surface roughness. However, to ensure an optimal balance, the pressure drop incurred due to enhanced roughness and the increased rate of heat exchange need to be carefully weighed. The need for more detailed studies to inform the design and operation of TES systems, considering the balance between pressure drop, heat transfer rate, and storage efficiency. Moreover, the derived parameters like charging efficiency, HTF outlet heat transfer rate, and energy stored during charging could be instrumental in future research to pinpoint an optimal surface roughness level, leading to the creation of more efficient TES systems. Through such data-driven visions, there is a compelling scope for refining system design and linking surface roughness as a tool to enhance performance in practical applications.

In situations where the TES material directly contacts the HTF, and both have relatively low thermal conductivities, the use of artificial surface modifications, such as indentations or fins, can be beneficial. These modifications not only increase surface roughness but also expand the effective surface area for heat transfer. The design and application of internal fin configurations is a well-established field in industrial applications(Shah and Sekulic, 2003). These configurations, each with its unique benefits and potential challenges, have been successfully implemented in areas from tubing to heat exchangers (Masliyah and Nandakumar, 1976; CARNAVOS, 1980; Zhang and Faghri, 1996; Xie et al., 2008). It is suggested that these established practices be studied for their potential application in TES systems where material and HTF are in direct contact.

As the optimization study in Chapter IV concludes, it provides a comprehensive understanding of the influential parameters and optimal configurations that could enhance the efficiency of TES systems. These insights represent a significant milestone in the research and form a solid foundation for the subsequent chapter, which will utilize machine learning techniques. This transition from conventional optimization methods to machine learning approaches represents an evolutionary step in TES design optimization.

Chapter V.

Machine Learning Approaches for TES Design

Starting with, the research introduces machine learning, ML, techniques to the field of thermal energy storage design. Capitalizing on the knowledge and insights gathered from the preceding chapters—from the role of cementitious materials in TES, to the potential of geopolymer concrete, and through to the stages of prototype development, experimental validation, and system optimization—the objective of this chapter is to significantly enhance the efficiency and accuracy of TES design. This chapter begins with a detailed overview of machine learning in the context of TES, followed by an application of a proposed machine learning algorithm, and ultimately culminates in the optimization of TES design through the use of advanced machine learning methodologies. The ML model, once trained, has the capacity to oversee a significantly larger array of combinations of parameters for TES design.

5.1 Introduction to Machine Learning in TES

Artificial Intelligence (AI), at its core, emulates human cognitive abilities through computational processes, including learning, reasoning, and self-correction (Abdalla et al., 2021; Senior et al., 2020). Nested within AI is a subset called Machine Learning, which uses empirical data to enhance performance on tasks without the need for explicit programming (Abualigah et al., 2022; Benti et al., 2023; Lai et al., 2020). A more refined subclass, Deep Learning, utilizes intricate neural networks to tackle complex data interpretation tasks, such as image recognition, speech recognition, and natural language processing (Abdalla et al., 2021; Graves et al., 2013; Senior et al., 2020; Wang et al., 2019). Particularly in the renewable energy sector, Deep Learning has notably outclassed traditional approaches in forecasting accuracy (Benti et al., 2023).

Furthermore, the application of Multi-Criteria Decision Analysis (MCDA) and Multi-Objective Optimization (MOO) techniques allows for the handling of conflicting criteria and simultaneous optimization of multiple factors, respectively (Paradowski and Sałabun, 2021), (Deb, 2011). Specifically, within the framework of MCDA and MOO, Evolutionary Multi-Objective Optimization (EMO) emerges as a potent technique for evaluating options such as Concentrated Solar Power systems against various performance measures (Klein, 2013).

Expanding our focus to the renewable energy sector, we see AI and ML assuming vital roles in addressing myriad challenges, from integration and control to stability assessment and system optimization (Bose, 2017; Chen et al., 2021; Rahman et al., 2020), (Perera et al., 2014). Coupled with MCDA and MOO techniques, they aid in crucial processes such as materials selection for thermal energy storage and optimal system design (Paradowski and Sałabun, 2021). These technologies prove instrumental for functions like power prediction, grid management, and optimal sizing (Perera et al., 2014). They also enhance forecasting accuracy for wind farm production (Malakouti, 2023), solar irradiation (Voyant et al., 2017), and revenue predictions for integrated energy systems (Lin et al., 2022), thereby facilitating optimal utilization of renewable energy resources.

ML techniques have found significant application in TES systems by automating tasks, enhancing decision-making processes, and optimizing system performance (Borri et al., 2021; He et al., 2022; Lee et al., 2022; Olabi et al., 2023). These technologies have been integral in optimizing TES performance (Olabi et al., 2023), augmenting system efficiency under diverse loads (Lee et al., 2022), and elevating the stability of thermal energy storage (Chandan et al., 2022). Of particular note is their proficiency in enhancing the reliability and efficiency of phase change material-based TES systems (Ren et al., 2022; Shettigar et al., 2020). Nevertheless, ongoing research efforts are necessary to continually innovate and address existing limitations in these technologies.

In this vein, the current study introduces an innovative framework that brings together ML with MCDA for the design and optimization of solid-based sensible TES units. It's a versatile approach that can be applied across both non-renewable and renewable sectors, including Concentrated Solar Power plants, Solar Process Heat (SPH) (Famiglietti et al., 2020), and Industrial Waste Heat (IWH).

This proposed framework expands upon previous researches focused on introducing TES material, conducting thermal assessments, performing experiments, and developing as well as validating numerical models for a TES module based on geopolymer concrete (Rahjoo et al., 2023, 2022b, 2022a). Utilizing an EMO, generating a set of Pareto-optimal solutions, which are evaluated using an ML-based Decision Support System (DSS). The DSS incorporates decision tree ML algorithms (Breiman, 2017; SONG and LU, 2015) to classify and assess the suitability of these solutions.

The decision tree model's viability lies in its simplicity, interpretability, and computational efficiency. It provides a framework that encapsulates evolved, non-linear decision-making, closely resembling human reasoning. As such, it has wide applicability in numerous domains where complex relationships need to be learned, understood, and explained (Fürnkranz, 2010; Kotsiantis, 2013; SONG and LU, 2015). The effectiveness of the proposed framework is then going to be demonstrated through its application to a TES system tied to a parabolic trough CSP plant in Morocco (Zanganeh, 2014). Finally, the optimized design parameters are going to be validated through simulations conducted with COMSOL software (Multiphysics, 2022), resulting in a scalable design proposal for a TES unit fitting the plant's specifications (Zanganeh, 2014).

5.2 Application of Proposed ML Algorithm

The approach comprises several stages, as depicted in Figure 5-1. The process initiates with laboratory investigations to gather empirical data relevant to the TES system's functioning from previous chapters. Subsequently, a representative numerical model of the TES system is developed and validated. The approved numerical model becomes instrumental in generating diverse datasets, which are subject to intensive data mining. This aids in unearthing patterns and connections between the input variables and the corresponding outputs. Data normalization and pre-processing steps are then undertaken to standardize the dataset and prime it for application into a decision tree model.

The decision tree model is built with the aim of forecasting the performance metrics of the TES system using the pre-processed data. For ensuring predictions, the dataset is partitioned into a training set for model construction and a testing set for validating the model's accuracy. Further, to minimize overfitting, the decision tree model is pruned and its hyperparameters are optimized to deliver performance on the testing set. The model's performance is gauged using diverse metrics, and its accuracy is corroborated by juxtaposing its predictions with the testing dataset.

Following the model validation, multi-objective optimization and multi-criteria decision analysis techniques are deployed to pinpoint favorable design parameters and operating conditions based on defined targets. These findings are contrasted with the results of a specific Computational Fluid Dynamics simulation, where the optimized design configuration and operating conditions are implemented (designated as 'COMSOL Validation'). Given the resemblance in outcomes from both methods, the validation of the MOO and MCDA techniques can be confirmed.

The project culminates with an upscale evaluation that aims to design an entire TES system. This design hinges on the optimized module design paired with the refined operating conditions, cumulating in a pragmatic 'TES Heat Exchanger Design'.

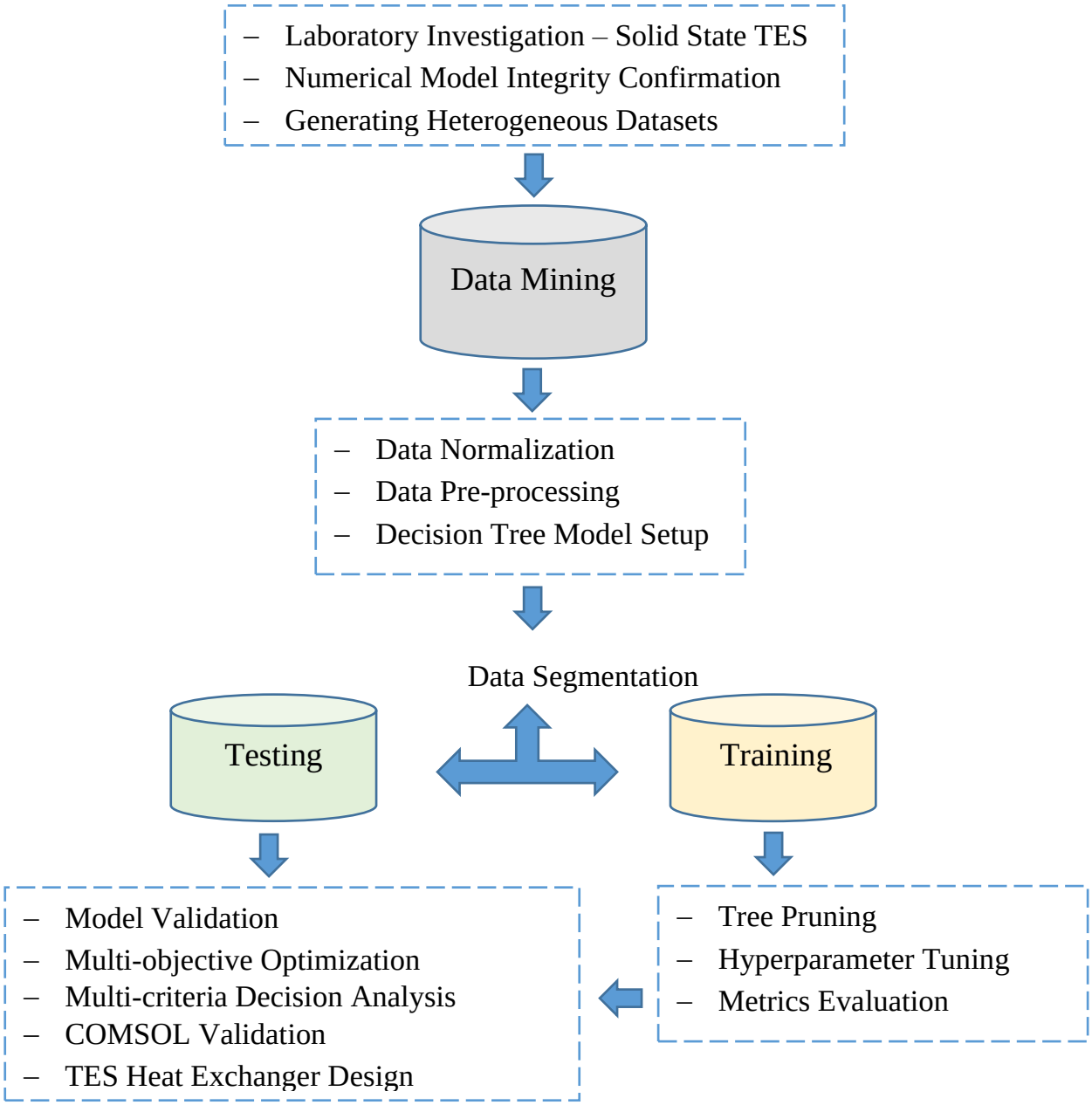

Figure 5-1. Overview of the machine learning methodology for solid TES system optimization

5.2.1 Decision Tree ML Model

Decision Tree (DT) Models are a type of supervised machine learning algorithm that have been widely used to build classification models (Fürnkranz, 2010; Kotsiantis, 2013; SONG and LU, 2015). These models closely resemble human reasoning and are easy to understand. They are efficient and can be induced from data (Fürnkranz, 2010). The induction of decision trees is one of the oldest and most popular techniques for learning discriminatory models (Fürnkranz, 2010). DT models create a hierarchical structure, resembling a tree, where every node signifies a decision, and each terminal leaf node signifies an ultimate outcome. These models are trained through a recursive process of partitioning the training data into progressively smaller subsets, guided by the input feature values. During each partition, the algorithm selects the feature that most effectively segregates the data into two distinct groups. This recursive process continues until each node contains sufficiently homogeneous data (Fürnkranz, 2010; Kotsiantis, 2013; SONG and LU, 2015). The algorithm's inherent parallelizability, coupled with its streamlined prediction process of navigating the tree structure, results in exceptional computational efficiency. In the present work, it is employed a decision tree model to predict key performance parameters of solid TES units, even though there are other models such as Support Vector Machines (SVM) (Noble, 2006), Random Forests (Breiman, 2001), and Neural Networks (YEGNANARAYANA, 2009). The focus of what is presented here is not on a comparative study of these models. Rather, the emphasis is on assessing the feasibility and effectiveness of the decision tree model in this specific context.

As shown in Figure 5-2, the tree evolves from the root node, that initially holds all the examples, and rows out through a recursive, divide-and-conquer strategy. This strategy results in partitioning the entire dataset into smaller, increasingly pure subsets. The root node, at the highest level, comprises the entire dataset. The decision nodes, depicted at subsequent levels, represent the points where the tree splits based on the value of a particular attribute. The selection of this attribute is crucial and governed by an objective function. This process of progressive partitioning continues until the remaining examples in a leaf node are of the same class, or the remaining examples can no longer be split. At this point, the leaf node, depicted at the lowest level of Figure 2, represents the final outcome or decision made by the model.

In this work, a DT Model is implemented as part of a machine learning methodology for designing and optimizing solid-state TES units. The implementation process involves several steps, as outlined in the earlier section of the work. The Decision Tree Model is constructed to forecast key performance metrics of the TES system using pre-processed data. Scikit-learn library (Pedregosa et al., 2011)has been used to implement the decision tree model.

They initialize the model with the *DecisionTreeRegressor* class, setting the *random_state* hyperparameter to ensure reproducibility. To find the best hyperparameters for the DT model, the *GridSearchCV* class has been used. This class performs grid search with cross-validation to evaluate different combinations of hyperparameters and select the best-performing model. Later, by evaluating the performance of the decision tree model on the testing data, the feature importance study was done to understand the significance of each feature in making predictions.

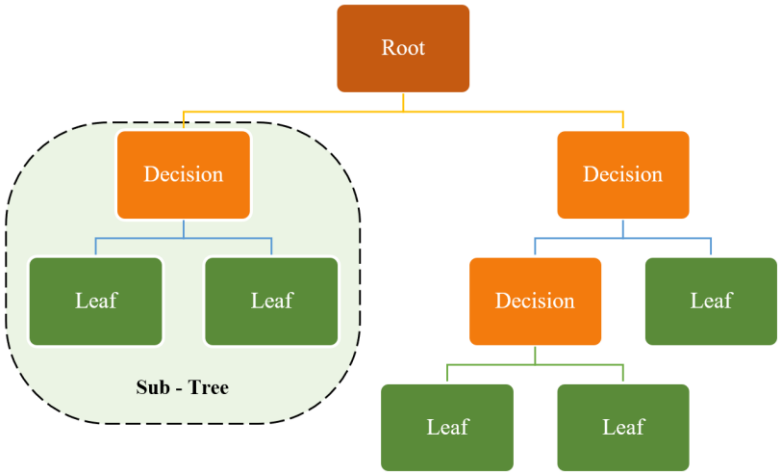

Figure 5-2. Schematic representation of a decision tree model.

To facilitate the training of the decision tree model, a comprehensive dataset was curated from an extensive array of simulation runs, encompassing 675 different charging scenarios. Each charging scenario was characterized by a specific set of design parameters, including initial TES module temperature (T_0), inlet air temperature (T_{inlet}), tube radius (R), module size (S), heat transfer fluid (HTF) velocity (v), and charging time (t_{charge}). The parameter value ranges are detailed in Table 5-1.

These simulations were conducted utilizing a computational fluid dynamics model developed within COMSOL Multiphysics (Multiphysics, 2022). As discussed in previous chapters, the CFD model underwent thorough validation against experimental findings to ascertain its accuracy and dependability.

Table 5-1. Design Parameters for solid TES module simulations.

Design Parameter	Values	Units
Initial temperature (T_0)	215, 265, 315	°C
Inlet air temperature (T_{inlet})	400, 450, 500, 550, 600	°C
Tube radius (R)	1/2, 3/4, 1	Inch
Module size (S)	100, 150, 200, 250, 300	mm
HTF (Air) velocity (v)	3, 6, 9	m/s
Charging time (t_{charge})	2, 4, 6, 7.5, 8, 10	hour

The tube radius values are given in inches, since this unit is technically the most widely one used and not SI units, so it is clearly identified which size of tubes the work refers to.

The selection of parameter values sought to encompass an extensive spectrum of operational conditions. This broad coverage was designed to equip the machine learning model with the capability to adapt and extrapolate to novel scenarios. The chosen design and performance parameters draw upon the comprehensive research and metrics provided by previous studies, thereby ensuring that the design and performance parameters are grounded in rigorously examined scientific theory (Cabeza et al., 2022c; Mikkelson and Doster, 2022; Tamme et al., 2004b; Meseret Tesfay, 2014). The objective of the machine learning model is to forecast following six key performance metrics for the TES unit:

- Heat transfer fluid outlet temperature ($T_{HTF\_out,}$ in ºC)
- Heat transfer fluid pressure drop (ΔP in Pa)
- Solid TES bulk average temperature ($<T_{TES}>$ in ºC)
- Solid TES bulk thermal storage capacity (Q_{st} in J)
- Heat transfer fluid output heat rate ($\dot{Q}_{storage}$ in W)
- Charging efficiency (η_{charge} non-dimensional)

The first three targets are directly derived from the CFD simulation results, while the latter three are computed using Equations 4-15 to 4-17 presented in previous chapter. The average temperature of the solid element, $<T_{TES}>$, is deemed representative of its temperature distribution performance.

5.2.2 Model Accuracy

The decision tree model was trained using the resulting data, with the objective of forecasting key performance parameters of the solid TES model based on the aforementioned design parameters. The model's efficacy in predicting the six targets was assessed, and hyperparameter tuning was executed to improve the model's performance. A grid search, accompanied by cross-validation, was employed to identify the optimal estimator for each target. Also, a thorough evaluation of the model's performance was conducted by comparing its predictions to the experimental and simulation results.

The evaluation metrics included R-squared value (R^2), mean absolute error (MAE), mean squared error (MSE), root mean squared error (RMSE), explained variance score (EVS), and mean absolute percentage error (MAPE), which are commonly used to assess the accuracy and robustness of machine learning models (Pedregosa et al., 2011; Raschka and Mirjalili, 2019). Metrics used are presented in Eqs. 5-1 to 5-6 where, y_i refers to the actual value of the target variable, $\hat{y}_i$ denotes the predicted value, and $\bar{y}$ represents the mean of the observed values.

R-squared

$$R^2 = 1 - \frac{\sum_{i=1}^{n} (y_i - \hat{y}_i)^2}{\sum_{i=1}^{n} (y_i - \bar{y})^2} \quad (5\text{-}1)$$

Mean absolute error

$$MAE = \frac{1}{n}\sum_{i=1}^{n} |y_i - \hat{y}_i| \quad (5\text{-}2)$$

Mean squared error

$$MSE = \frac{1}{n}\sum_{i=1}^{n} (y_i - \hat{y}_i)^2 \quad (5\text{-}3)$$

Root mean squared error

$$RMSE = \sqrt{\frac{1}{n}\sum_{i=1}^{n} (y_i - \hat{y}_i)^2} \quad (5\text{-}4)$$

Explained variance score

$$EVS = 1 - \frac{Var(y_i - \hat{y}_i)}{Var(y_i)} \quad (5\text{-}5)$$

Mean absolute percentage error

$$MAPE = \frac{1}{n}\sum_{i=1}^{n} \left|\frac{y_i - \hat{y}_i}{y_i}\right| \times 100 \quad (5\text{-}6)$$

The mean absolute error (Equation 5-1) and mean squared error (Equation 5-2) were utilized to measure the average magnitude of errors between predicted and actual values. Additionally, the root mean squared error (Equation 5-3) was employed to gauge the magnitude of errors while maintaining the same scale as the target variable. The explained variance score (Equation 5-4) was used to measure the proportion of variance in the target variable that the model explained while accounting for the baseline variance. Lastly, the mean absolute percentage error (Equation 5-6) was used to measure the percentage difference between predicted and actual values, proving useful for understanding the relative magnitude of errors irrespective of scale.

The accuracy of the model in predicting several critical metrics for the TES system was notable. Table 5-2 provides precise metrics for the model's accuracy in predicting key variables for the TES system. High R-squared values (>0.9) indicate strong precision, while low MAE and MSE values (<15 and <300, respectively) reflect minimal prediction errors.

Table 5-2. ML Model Evaluation Metrics

Metrics/ targets	R^2	MAE	MSE	RMSE	EVS	MAPE
T_{HTF_out}	0.9086	12.1396	282.1680	16.7979	0.9104	0.0307
ΔP	0.9999	0.0429	0.0421	0.2052	0.9999	0.0014
$<T_{TES}>$	0.9373	13.1174	257.5234	16.0475	0.9375	0.0381
$Q_{storage}$	0.9803	0.3637	0.3210	0.5666	0.9805	0.0672
$\dot{Q}_{storage}$	0.9572	14.2906	386.7021	19.6647	0.9577	0.0920
η_{charge}	0.9816	0.0170	0.0009	0.0307	0.9817	0.0974

The ML model's quality was further evaluated by plotting the predicted values against the actual values for each target variable. Figure 5-3 displays the plots for each target variable, with the x-axis representing the actual values and the y-axis representing the predicted values after training. The plots exhibit the correlation between the predicted and actual values, as most data points are situated close to the diagonal line.

This proximity signifies that the model has satisfactory prediction control between the predicted and actual values.

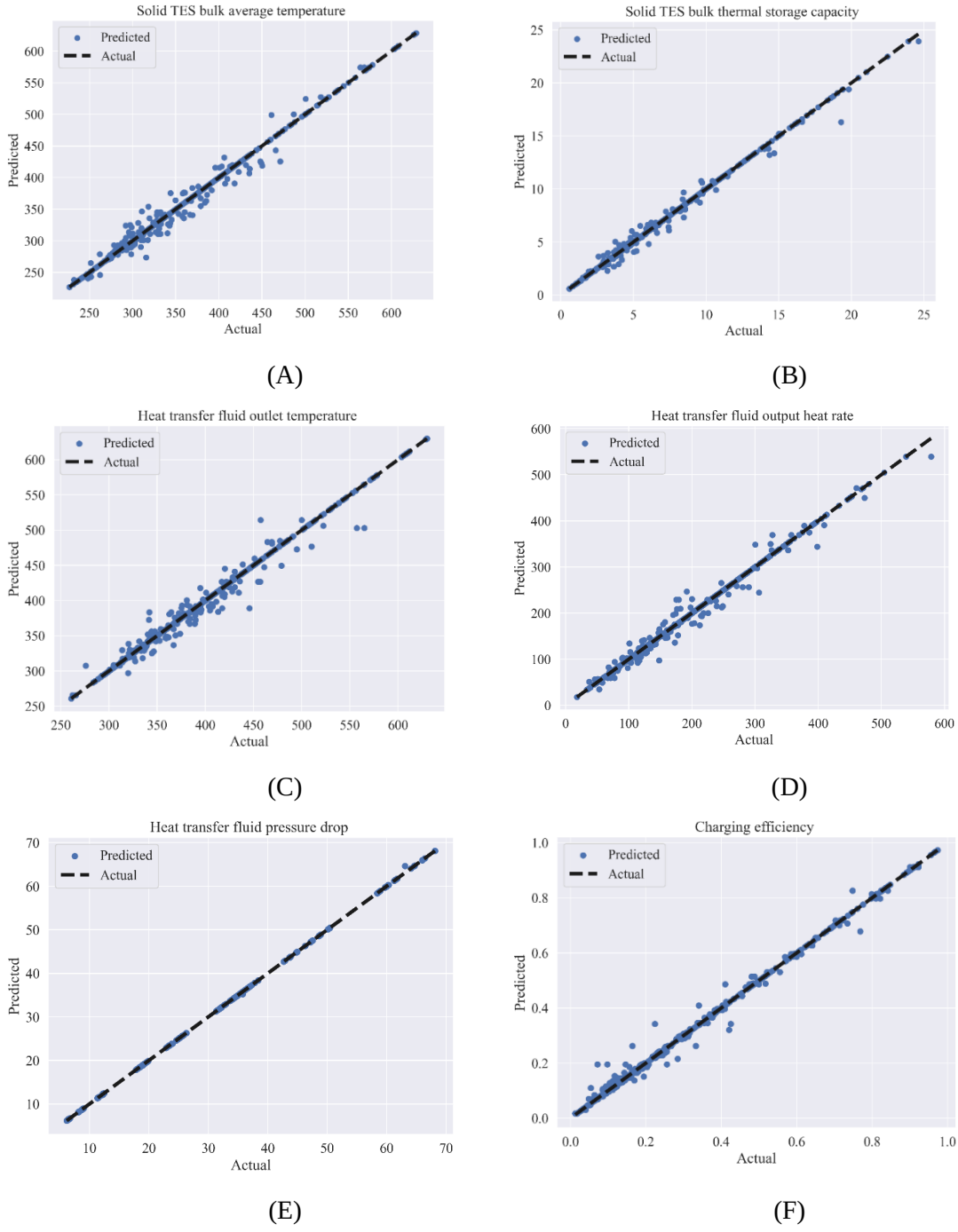

Figure 5-3. Predicted values trained by machine learning.

(A) $<T_{TES}>$, (B) $Q_{storage}$, (C) T_{HTF_out} , (D) $\dot{Q}_{storage}$, (E) ΔP and (F) η_{charge}.

Table 5-3 summarizes the performance of six decision-tree regression models, each trained on a different target variable. The models were trained with a random state of 42,

which ensures that the results are reproducible. The appropriate models were identified based on the criteria of max_depth and min_samples_split, with the optimal depth being generally between 15 to 17. The tree node count, signifying the complexity of the model, varied from 587 for the ' ΔP ' model to 1079 for the ' T_{HTF_out} ', '$<T_{TES}>$' models, demonstrating the variety in the models' structures.

Computational time, RAM, and CPU are essential for evaluating the practicality of a model, particularly in real-time applications where speed and resource utilization are critical. Interestingly, ' ΔP' and ' η_{charge}' models performed well not only in accuracy metrics, Table 5-3, but also have relatively lower computational times.

Table 5-3. Decision Tree Regression Model Performance (random_state=42)

Metric	Unit	T_{HTF_out}	ΔP	$<T_{TES}>$	$Q_{storage}$	$\dot{Q}_{storage}$	η_{charge}
DT Model (max_depth)	-	16	17	15	16	15	15
Tree Node Count	-	1079	587	1079	1077	1051	1057
Tree Max Depth	-	16	13	15	16	15	15
Computational Time	s	2.6	2.08	2.21	3.10	3.52	2.10
RAM Usage	bytes	351868	351868	351868	351868	351868	351868
CPU Usage	CPU-s	155.59	157.67	159.87	162.94	165.93	168.03

5.2.3 Model Sensitivity Analysis

The significance of specific features in predicting target values has been scrutinized using the *feature_importances_* attribute through the scikit-learn package (Pedregosa et al., 2011). Employing a feature importance metric provides quantifiable data regarding the relative contribution of each input feature in a machine learning model's prediction of the target variable.

When dealing with Decision Trees, the importance of a feature is typically gauged by the resultant decrease in impurity (such as Gini impurity) from partitioning the data on the basis of that particular feature (Breiman, 2017; SONG and LU, 2015).

This method quantifies the importance of each feature as the aggregate over the number of splits (across all trees) comprising the feature, proportionally accounting for the number of samples it divides. A higher importance score for a feature indicates that it plays a more significant role in predicting the target variable. The relevant general formula for the Gini Importance equation is detailed in ("1.10. Decision Trees," n.d.).

Furthermore, the *PolynomialFeatures* (Pedregosa et al., 2011) function was then used to create a polynomial equation for each target value, which facilitated in clarifying the relationship between the design parameters and the performance metrics of the TES module. The equation format of a fitted regression model using "PolynomialFeatures" in scikit-learn is given as follow:

$$y = \beta_0 + \beta_1 x_1 + \beta_2 x_2 + \cdots + \beta_n x_n + \beta_{n+1} x_1^2 + \beta_{n+2} x_1 x_2 + \cdots + \beta_{2n} x_n^2 + \epsilon \qquad (5\text{-}7)$$

Where y is the target values, $x_{1,2,\ldots,n}$ are design parameters, $\beta_{1,2,\ldots\ldots,n}$ are the coefficients of the model, and ϵ is the error term. The first part of the equation represents the linear relationship between the independent and dependent variables, while the second part represents the nonlinear relationships captured by the polynomial terms. PolynomialFeatures generates a new feature matrix consisting of all polynomial combinations of the original features up to a specified degree. By doing so, it can provide a more accurate representation of the relationships between the variables, capturing nonlinearities in the data. The transformed feature matrix is then used to fit a regression model to the data, allowing for the calculation of equations that can be used to predict the values of the target variables. The regression equations derived from the feature importance and equation 5-7 are presented in Table 5-4.

Figure 5-4 integrates dual graphical illustrations to elucidate the role of design parameters' feature importance in the system under study. The inaugural visual, denoted as a heatmap (A), color codes the varying levels of importance among the design parameters based on their relative significance. In contrast, the Sankey diagram offers a visually intuitive representation of the impactful design parameters on the system's performance, demonstrating how they intricately interweave. The dimension of the arrows within the Sankey flow diagram serves as a symbol of the magnitude of each design parameter's

influence on the output. The most important parameters for each target variable are as follows:

1. For HTF outlet temperature, $T_{HTF\_out,}$ the most important parameter is inlet air temperature, $T_{inlet,}$ followed by module size, S, and HTF velocity, v.
2. For HTF pressure drop, ΔP ,the most important parameter is HTF velocity, v, followed by tube radius, R, and initial temperature, T_0.
3. For solid TES module bulk average temperature, $<T_{TES}>$, the most important parameter is module size, S, followed by inlet air temperature, $T_{inlet,}$ and tube radius, R.
4. For concrete TES module bulk thermal storage capacity, $Q_{storage}$, the most important parameter is inlet air temperature, $T_{inlet,}$ followed by initial temperature and tube radius.
5. For HTF output heat rate, $\dot{Q}_{storage,}$ the most important parameter is module size, S, followed by HTF velocity, v, and inlet air temperature, $T_{inlet,}$
6. For charging efficiency, $\eta_{charge,}$ the most important parameter is module size, S, followed by initial temperature, $T_{0,}$ and inlet air temperature, $T_{inlet,}$

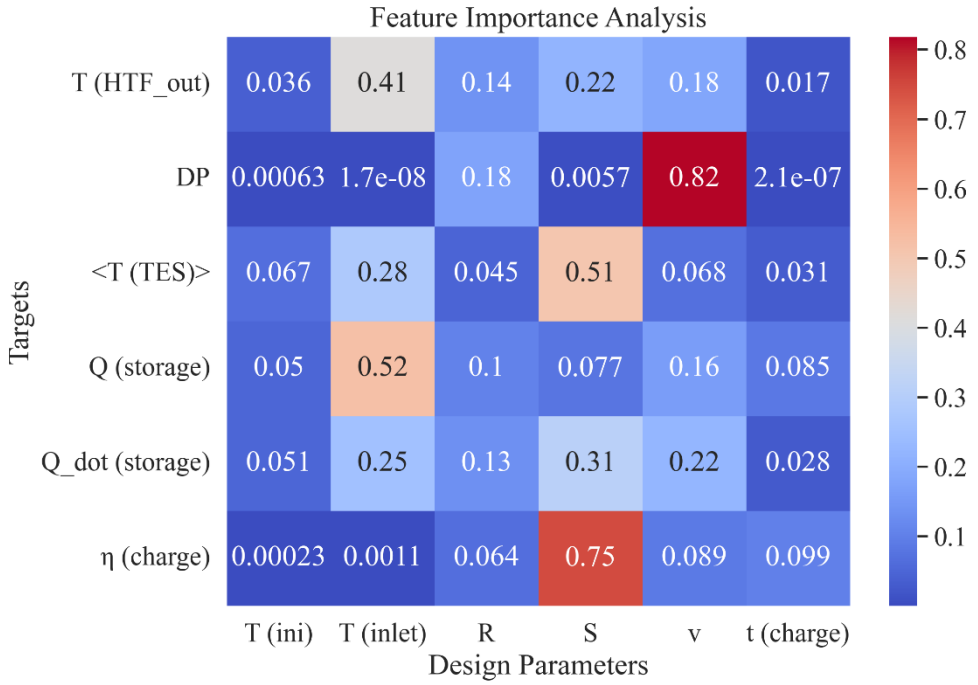

(A)

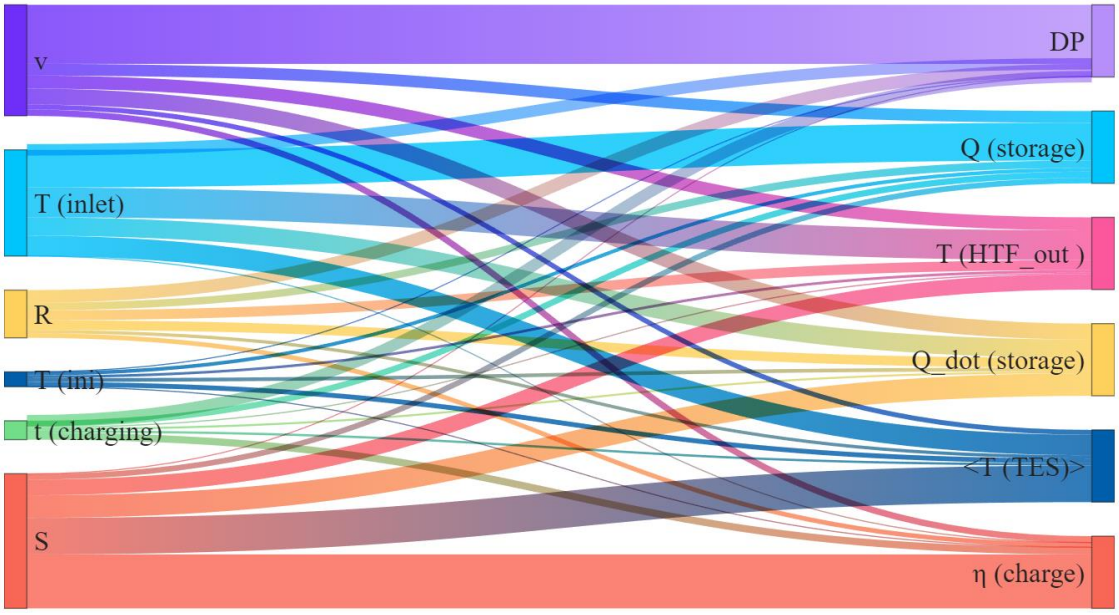

(B)

Figure 5-4. Design Parameter Importance Visualization.

In essence, the feature importance analysis implies that the inlet air temperature (T_{inlet}) and module size (S) are key design parameters when it comes to predicting most target values. However, the proportional significance of each parameter varies depending on the specific target value in question. It is therefore crucial to meticulously assess their individual and collective effects to enhance system performance optimization. Additionally, understanding which design parameters are not as influential is equally vital. This knowledge enables their final values to be dictated by other technical constraints, such as ease of manufacturing. In clearer terms, the less impactful parameters can be adjusted to meet other technical considerations without significantly affecting the system's performance.

The results from Table 5-4, which showcases the regression coefficients for design parameters, can be compared and contrasted with the feature importance analysis.

Table 5-4. regression coefficient table for design parameters.

Coefficients	T_{HTF_out}	ΔP	$\langle T_{TES} \rangle$	$Q_{storage}$	$\dot{Q}_{storage}$	η_{charge}
intercept	1,09E+18	3,88E+10	-5,27E+10	-1,30E+17	4,57E+10	7,81E+07
T_0	-4,10E+15	-1,39E+07	6,81E+08	4,89E+14	3,90E+08	-5,00E+05
T_{inlet}	9,05E+15	-9,00E+04	3,51E+08	-1,08E+15	-3,57E+08	7,10E+05
R	1,32E+10	-6,61E+09	7,41E+09	-5,45E+08	8,76E+08	5,06E+07
S	-5,51E+08	-3,39E+07	-5,70E+08	-1,31E+07	-3,37E+08	-5,01E+06
v	1,48E+10	1,21E+10	1,01E+10	-6,20E+08	1,98E+09	6,70E+07
$t_{charging}$	-6,88E+17	8,00E+04	5,70E+05	8,21E+16	-6,85E+06	1,00E+04
$T_0 \times T_{inlet}$	0	0	-4,12E+05	4,08E+12	-4,50E+04	0
$T_0 \times R$	-3,69E+07	6,90E+05	1,05E+08	-2,40E+06	0	-1,00E+03
$T_0 \times S$	1,77E+06	-3,63E+06	3,22E+06	-6,00E+04	-3,17E+06	0
$T_0 \times v$	0	-4,14E+06	-3,18E+07	-3,10E+06	3,05E+07	-1,00E+04
$T_0 \times t_{charge}$	2,59E+15	0	1,62E+06	-3,10E+14	4,61E+07	2,50E+05
$T_{inlet} \times R$	3,89E+07	0	2,34E+07	2,16E+06	4,62E+07	0
$T_{inlet} \times S$	-1,66E+06	-1,00E+04	-2,84E+06	5,00E+04	2,28E+06	0
$T_{inlet} \times v$	4,55E+07	1,00E+04	2,88E+07	2,75E+06	6,05E+07	0
$T_{inlet} \times t_{charge}$	1,95E+07	-1,39E+04	2,72E+07	2,53E+06	-2,57E+07	1,00E+04
$R \times S$	-9,18E+06	2,12E+06	0	0	9,53E+07	-1,40E+05
$R \times v$	-1,57E+08	-5,72E+08	0	0	9,80E+07	4,70E+04
$R \times t_{charge}$	7,29E+07	6,00E+04	3,26E+08	3,79E+07	-1,17E+09	1,66E+06
$S \times v$	-1,50E+07	-3,63E+06	-4,12E+07	0	1,15E+08	-1,70E+05
$S \times t_{charge}$	-3,47E+07	0	-4,97E+07	1,67E+06	6,05E+07	-2,60E+05
$v \times t_{charge}$	1,62E+08	1,70E+05	4,27E+08	5,07E+07	-1,46E+09	2,18E+06
T_0^2	-4,00E+04	2,00E+04	1,50E+05	2,00E+01	1,30E+05	0
T_0^2	-2,60E+05	0	-5,00E+04	0	-2,30E+05	-1,00E+01
R^2	-4,26E+08	2,53E+08	-1,40E+08	-8,70E+06	-4,44E+08	-5,50E+05
S^2	2,63E+06	2,00E+04	3,87E+06	-9,00E+01	-4,50E+06	2,00E+01
v^2	-9,79E+08	3,36E+08	-5,12E+08	-3,80E+07	-1,27E+09	-2,04E+06
t_{charge}^2	-1,52E+08	3,00E+05	-2,81E+08	-1,37E+07	3,64E+08	-1,52E+06

Comparatively, for the HTF outlet temperature (T_{HTF_out}), the regression table suggests that T_{inlet}, S, and HTF velocity (v) significantly impact the outcome, corroborating the feature importance analysis. For the HTF pressure drop (ΔP), the regression coefficients for v, tube radius (R), and initial temperature (T_0), are significant, aligning with the feature importance findings. In the case of the solid TES module bulk average temperature ($\langle T_{TES} \rangle$), module size (S) is singled out in both analyses as a prominent factor. Similarly, for the concrete TES module bulk thermal storage capacity (Q_{st}), both analyses highlight

T_{inlet} as a key player. In terms of charging efficiency (η_{charge}), S and T_{inlet} are consistent influencers in both analyses, although the regression coefficients suggest a nuanced picture of their specific impacts.

In general, these findings emphasize the complex interplay between design parameters and target values, reiterating the need for individual and combined impact assessments to optimize performance.

5.3 Optimization of a TES system using ML

Building upon the findings of the previous section, this section aims to provide an in-depth analysis of the TES design parameters by employing a multi-objective optimization approach. To address the inherent complexity of the problem, characterized by a high-dimensional search space and multiple performance criteria, the Tree-structured Parzen Estimator (TPE) algorithm from the Optuna package (Akiba et al., 2019) is utilized for optimization. The TPE algorithm demonstrates a strong capacity for efficiently managing high-dimensional and non-convex optimization problems ("Optimization Problem Types - Convex Optimization," 2011). The TPE algorithm's core functionality lies in its ability to learn the joint distribution of hyperparameters and objective function values while striking a balance between exploration and exploitation during the search for an optimal solution.

Incorporating the TPE algorithm into a practical scenario, this paragraph focuses on the Ait Baha parabolic trough concentrated solar power (CSP) plant in Morocco (Zanganeh, 2014) as a case study to optimize the design of its TES unit combining Ml and MCDA algorithm. The Ait Baha CSP plant, Table 5-5, employs parabolic trough technology to harness solar energy, which is concentrated onto air and then directed through a packed bed of rocks that make up the TES system. This system possesses a capacity of 100 MWh_{th}. During the 10-hour charging phase, the working fluid enters the TES module at an inlet temperature of 640 ºC and cools down to 280 ºC at the outlet. Subsequently, the TES system discharges over a period of 4.5 hours at a flow rate of 4.058

kg/s, conveying the energy to the power block for electricity generation. The plant exhibits an annual electricity generation capacity of 2.39 GWh_e.

Table 5-5. Ait Baha Parabolic trough plant specification (Zanganeh, 2014)

Location	**Ait Baha, Morocco**
CSP Technology	Parabolic trough
TES Technology	packed bed of rocks
TES Capacity	100 $MWh_{thermal}$
Annual electricity generation	2.39 GWh
Working Fluid	Air
HTF inlet temperature	640 ºC
HTF outlet temperature	280 ºC
Ambient condition	20 ºC
Charging time	10 h
Charging flow rate	1.716 kg/s

5.3.1 Objective Function

The *objective* function serves as the core of the Optuna optimization workflow, representing the multi-objective optimization problem at hand. This function receives a *trial* object that facilitates the suggestion of hyperparameters. The parameters are either varied within their respective ranges or fixed. These variables collectively form a feature vector, utilized in conjunction with pre-trained Decision Tree models to generate predictions. The function returns these objectives, which in this analysis has been fixed to minimize the heat transfer fluid pressure drop (ΔP) and maximize the charging efficiency (η_{charge}) of the TES unit. The multi-objective optimization process incorporated the following steps:

(A) Defining the input parameters range for MCDA, for the already defined design parameters (T_0, T_{inlet}, R, S, v and t_{charge}), Figure 5-5.

(B) Constraining the range T_{inlet} at 640 ºC and t_{charge} at 10 hours based on the case study specification shown in Table 5-4.

(C) Utilization of a categorical distribution for hyperparameter selection during each trial.

(D) Identification of the best hyperparameters based on the maximum value of the objective function, encompassing both primary criteria: ΔP and η_{charge}.

(E) Creation of an optimization study object with the 'directions' set to ['minimize', 'maximize'], accommodating the dual nature of the optimization criteria.

(F) Acquisition of the optimized values for the design parameters (T_0, T_{inlet}, R, S, v, and t_{charge}) along with their corresponding ΔP and η_{charge} values using the established workflow.

(G) Iterative execution of the optimization process to ensure result consistency.

Optuna implements a form of automated hyperparameter tuning known as Sequential Model-based Global Optimization (SMBO). It generates a study object, which is subject to optimization using the *objective* function. The *study.optimize* method iteratively selects the next set of hyperparameters in a sequence of trials, guided by a sampler which utilizes past outcomes to suggest the next set of parameters. This intelligent search process, significantly more efficient than exhaustive search, focuses on exploring promising areas while limiting unnecessary trials in less promising areas. By iterating over such trials, Optuna effectively explores the parameter space and identifies Pareto-optimal solutions representing the optimal trade-offs between the objectives.

The Pareto optimal solutions embody a set of trade-offs between the two criteria and are presented in Table 6-6. The Pareto solutions reveal that by maintaining T_{inlet} at 640ºC and t_{charge} at 10 hours, the workflow has pinpointed a set of configurations that achieve the optimal balance between the competing criteria, $\max(\eta_{charge})$ and $\min(\Delta P)$.

Table 5-6. Pareto solutions observed for the two main criteria.

η_{charge}	ΔP	T_0	T_{inlet}	R	S	v	t_{charge}
0.196	6.171	300	640	20	250	3	10
0.111	6.265	300	640	25	450	4	10
0.083	8.115	300	640	15	350	4	10
0.059	11.330	300	640	10	400	3	10

The Optuna package derived a systematic and iterative approach. This analysis anchored its primary objective to maximize the charging efficiency (η_{charge}) and minimize the heat transfer fluid pressure drop (ΔP) of the TES unit. A zenith in charging efficiency (η_{charge}) of 0.196, coinciding with a HTF pressure drop (ΔP) of 6.171 Pa, is achieved when T_0 is 300 ºC, R is 20 mm, S is 250 mm, and v is 3 m/s. Figure 4 underscores that the velocity (v) and module size (S) are the chief objectives for the Multi-Objective Optimization, highlighting the concentration on performance optimization vis-à-vis these parameters.

For design parameter values, the selection of the lowest velocity is rational, as this aligns with the priority of curbing the detrimental consequences tied to ΔP, one of the pivotal criteria. Figure 5-5 visualizes the extracted Pareto solutions and the prescribed range for each parameter, providing a graphical account of the data furnished in Table 6. Based on the highest charging efficiency, the final Pareto solution proffers an η_{charge} of 0.196 and a ΔP of 6.171 Pa.

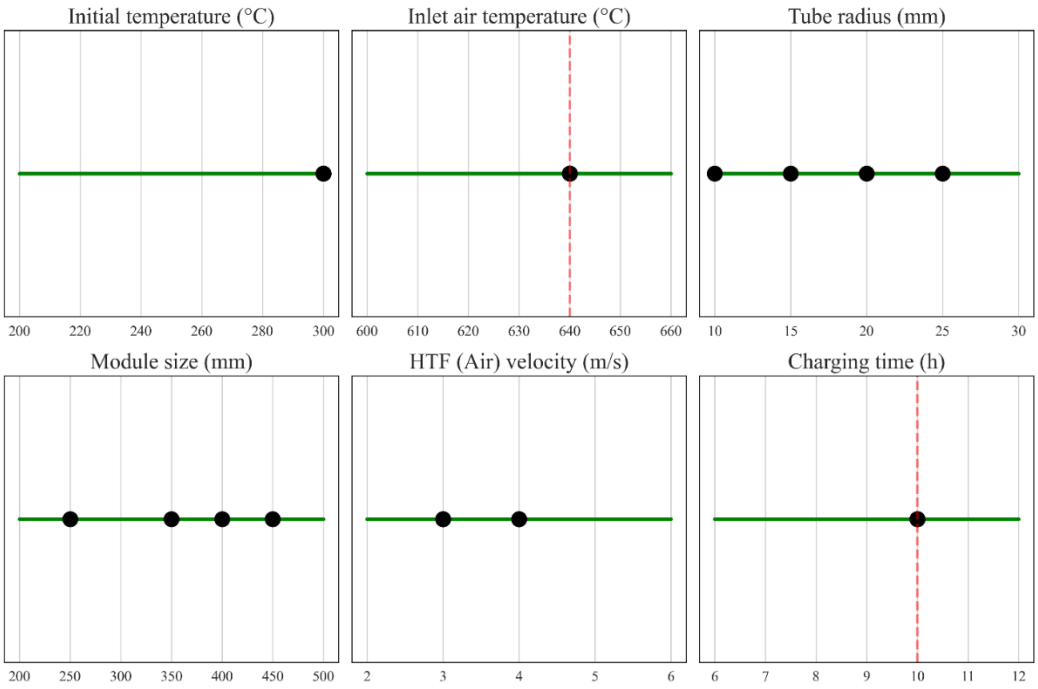

Figure 5-5. Achieved Pareto-optimal Solutions in the range of study for each design parameter. Constraint applied to Inlet air temperature and Charging time for the MCDA domain search.

In an effort to validate and affirm the precision and trustworthiness of the optimized design gleaned from the preceding sections, an analytical juxtaposition was performed with developed numerical model in previous chapters and within COMSOL Multiphysics (Multiphysics, 2022). These simulations were executed under a specific set of initial and boundary conditions, as follows:

- The module was assumed to have a uniform temperature at the beginning, with the average temperature being equal to the initial temperature:
  - $T_{avg}(x, y, z, t=0) = T_0$
- The external boundaries were considered to be adiabatic, implying no exchange of heat through the boundary, and therefore, the temperature gradient was zero:
  - $k\frac{\partial T(x=0,L,t)}{\partial x} = 0$; $k\frac{\partial T(y=0,L,t)}{\partial y} = 0$;$k\frac{\partial T(z=0,L,t)}{\partial z} = 0$
- The velocity and temperature of the fluid (air) at the inlet (z=0) were specified:
  - $v(r, \theta, z = 0, t) = v_{air}$ and $T_{air}\ (r, \theta, z = 0, t) = T_{inlet}$

- At the air outlet, (z=L), the normal heat flux was taken as zero and the pressure was assumed to be atmospheric. At $z = L; \vec{n}(k_{"air}" \nabla T_{"air}") = 0$ and $P(r, \theta, L, l) = P_{atmospheric}$
- No slip condition, i.e., there is no fluid motion at the solid interphase. At $v \ (r = d_l/2, \theta, z, t) = 0$

Table 5-7 presents the results of the key performance parameters with MCDA using ML and with the COMSOL simulations. This juxtaposition serves as a verification tool, confirming the congruity between the optimized design parameters furnished by the Machine Learning model and the outcomes derived from the numerical simulations.

Table 5-7 - Comparison of results obtained from MCDA and COMSOL (for a module 1 m long)

Model	T_{HTF_out}	ΔP	$<T_{TES}>$	Q_s	$\dot{Q}_{storage}$	η_{charge}
	Heat transfer fluid outlet temperature	Heat transfer fluid pressure drop	Concrete TES module bulk average temperature	Concrete TES module bulk thermal storage capacity	Heat transfer fluid output heat rate	Charging efficiency
	°C	Pa	°C	MJ	W	-
MCDA	437.02	6.17	366.7	11.805	328.89	0.196
COMSOL	458	5.01	367.9	12.018	294.89	0.20
Deviation	20.98	1.16	1.2	0.213	34	~0
	4.69 %	20.75 %	0.3 %	1.79 %	10.9 %	0.004 %

The optimized design parameters derived from the ML model exhibit only minor deviations from the results obtained through numerical simulations, indicating an elevated level of consistency between the two approaches. This consistency lends credibility to the optimization process and the chosen TES module design, thus validating the effectiveness of the proposed methodology. Without employing the workflow described, finding the optimal solution would have required thousands of simulations runs depending on the range of study for each design parameter. This extensive search would have incurred

significant computational costs and time. Therefore, the proposed methodology is not only more efficient but also more practical for optimizing the TES module design.

5.3.2 TES Design and Scale-up

Since trained data are obtained with a module length of 1 meter, a parametric study of various TES lengths was conducted in COMSOL to determine the required length to achieve an HTF outlet temperature, $T_{HTF\_out,}$ of 280 ºC as fixed by the case study (Table 5-4). The parametric study has been done assuming T_0=250 °C, resulting that a module length of 4 m is required to attain such an HTF outlet temperature of 280 ºC.

Figure 5-6 provides a clear representation of the outlet temperature evolution during the charging process over a 10-hour duration. The total pressure drop along the tube was estimated at 17.46 Pa.

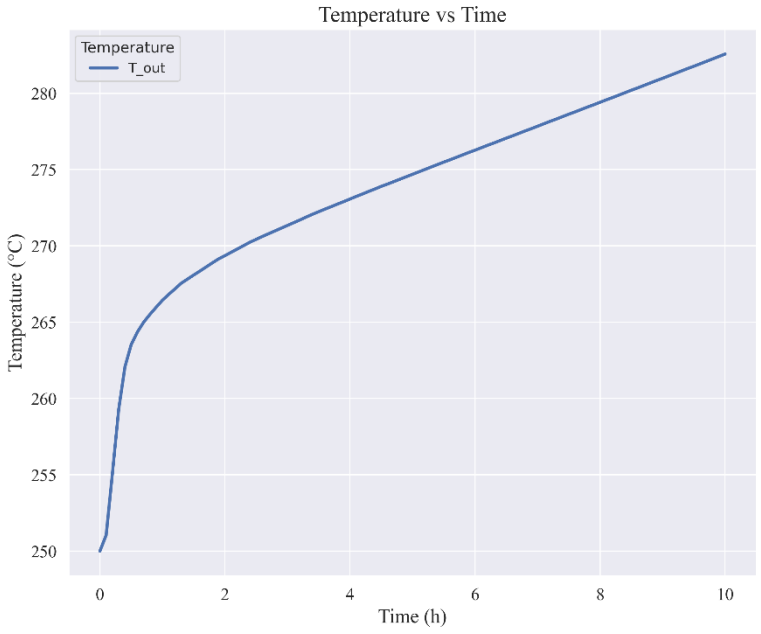

Figure 5-6. HTF Outlet Temperature, THTF_out, along 10-hour Charging Process.

Figure 5-7 illustrates the geometry of the simulated module, displaying both a full and quarter-section perspective (A), (B), and an upper view (C) with dimensions provided in millimeters. The quarter-section perspective (B) reveals the intricacies of the module's structure, demonstrating how the axisymmetric design lends itself to computational simplification. The upper view (C) further elucidates the module's geometric features and spatial relationships, enabling a comprehensive understanding of the dimensions and layout. Due to the axisymmetric of the solid module, only a quarter-section of the concrete TES module was modeled. This streamlined approach effectively captures the essential design characteristics while optimizing computational efficiency, ultimately facilitating a robust and reliable analysis of the module's performance.

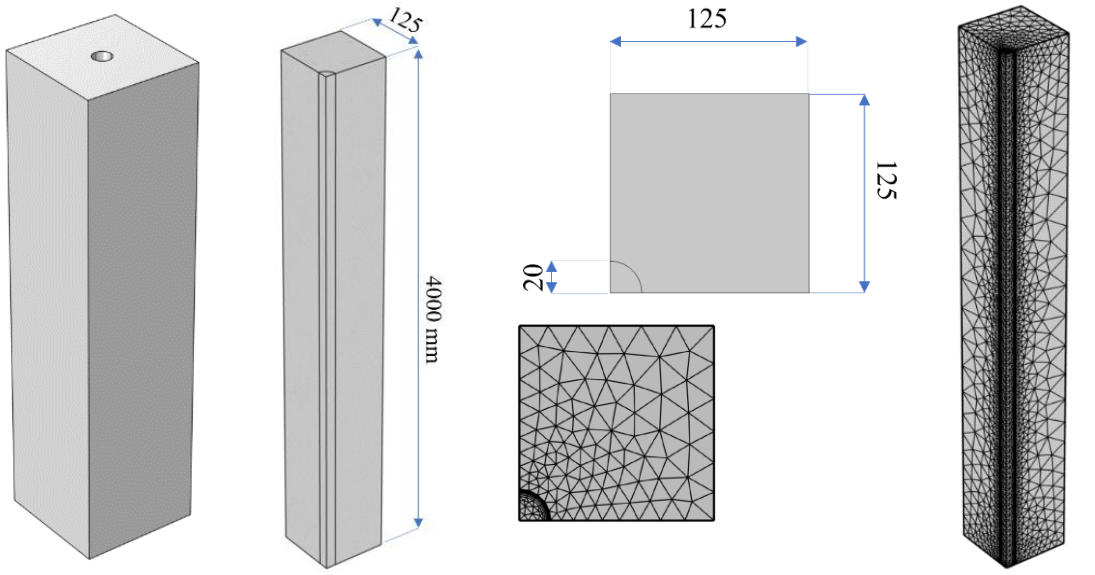

Figure 5-7. Geometry of simulated module.

(A) isometric view of full module, (B) ¼ perspective view with dimensions in mm, (C) upper view with dimensions in mm and (D) meshed geometry.

The mesh generation incorporated both tetrahedral and quadratic elements, with a refined resolution proximate to the boundaries, while maintaining coarser discretization in other regions. This strategic meshing approach ensures a balance between computational efficiency and solution accuracy, particularly near critical boundary regions where flow

phenomena necessitate higher fidelity representations, Fig. 5-7 (D). Figure 5-8 presents the heat distribution within a 1/3 inlet section of the TES module over various time steps, from the beginning (at 0h) to 10h, which is the final charging time. This time-dependent visualization highlights the progressive evolution of thermal gradients and the transient behavior of the system.

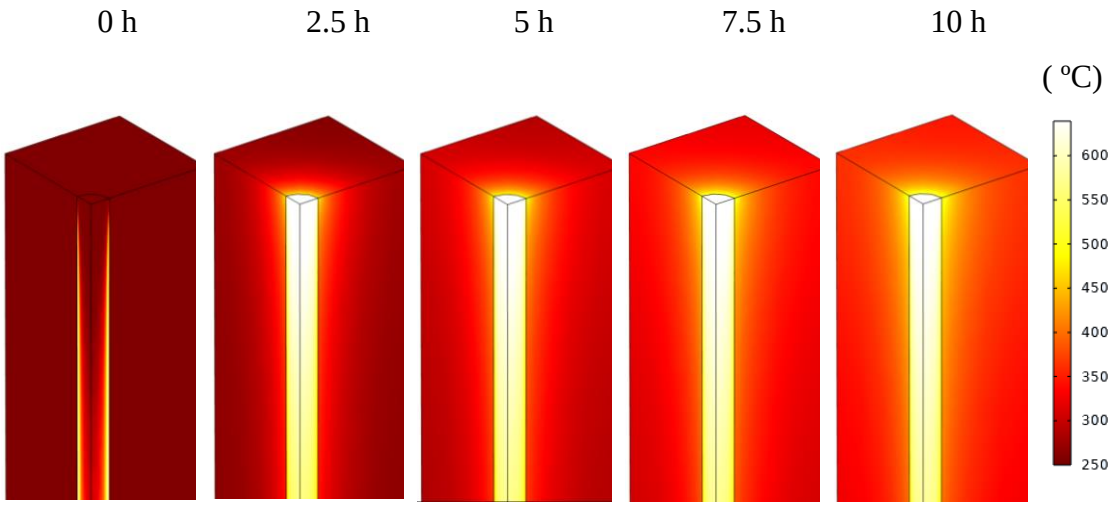

Figure 5-8. Temporal Evolution of Heat Distribution within 1/3 Inlet Section of TES Module.

It is clear from a comparison of results obtained from MCDA and COMSOL that employing a data-driven and machine learning-enabled design and optimization method significantly reduces the number of simulations required. As shown in table 5-7, out of the potential 2,700 combinations, only 675 were simulated and used to train DT model. This represents just 25% of the total possible combinations. In numerical terms, this approach, as a minimum, saves the need to run 2,025 simulations (2,700 - 675) which would have incurred significant computational resources and time.

More so, the trained ML algorithm applied to an even much more number of combinations, Figure 5-5. Its flexibility to oversee different inputs makes it capable of running tens of thousands of simulations, a feat which would be virtually impossible or at least highly impractical and resource-intensive using traditional methods. To ensure the

best results, the model should be regularly evaluated, validated, and fine-tuned based on new data and changing parameters.

Based on the MCDA, each optimized module exhibits a mass flow rate of 0.00144kg/s. In order to achieve the required mass flow rate in the case study (1.716 kg/s, see Table 5-5), it is necessary to combine and arrange multiple modules in a square/rectangular grid configuration.

Approximately 1192 modules are needed to achieve the required design flow rate. Let n represent the number of modules in each row and column; the total number of modules can then be expressed as $n \times n = n^2$. Taking the square root of both sides yields $n \sim 34.5$. Given that a fractional number of modules is infeasible, the nearest integer value is chosen, resulting in the need for 35 modules in each direction. This configuration enables the arrangement of a total of 1192 modules in a square matrix, effectively satisfying the plant's design flow rate requirements.

Incorporating 35 modules in each direction results in 33 extra modules, necessitating an alternative approach for a more efficient arrangement. One potential solution is to increase the number of modules in the horizontal direction while reducing the vertical module count, ultimately leading to a lower overall height. This configuration can be beneficial as it minimizes the structure's height, potentially reducing construction costs and complexity. By fixing the horizontal module count at 40, the equation to determine the number of vertical modules can be represented as $40 \times n = 1192$. Solving for n yields n = 29.8, which approximates to 30 vertical modules. This adjusted arrangement, consisting of 40 horizontal and 30 vertical modules, provides a more streamlined design while still achieving the desired flow rate for the plant.

In Figure 5-9, a parallel scheme is depicted, which entails dividing the mass flow rate proportionally across each branch. Integrating a parallel design with the modular TES system offers several benefits. Firstly, the parallel configuration allows for greater flexibility in managing the flow rates, as it is possible to adjust the distribution of the mass flow rate across different rows according to the solar filed yield. Secondly, the scheme facilitates easier expansion and scalability of the TES system. As the energy storage demand grows or the site requirements change, additional modules can be incorporated into the existing parallel rows or new rows can be added without significantly disrupting

the system's operation. Lastly, the combination of parallel design and modular TES system improves the system's reliability and maintainability. With multiple rows operating simultaneously, the failure of a single module or branch would have a lower impact on the overall system performance. Moreover, maintenance tasks can be conducted on individual rows without the need to shut down the entire TES system, minimizing downtime and ensuring continuous operation.

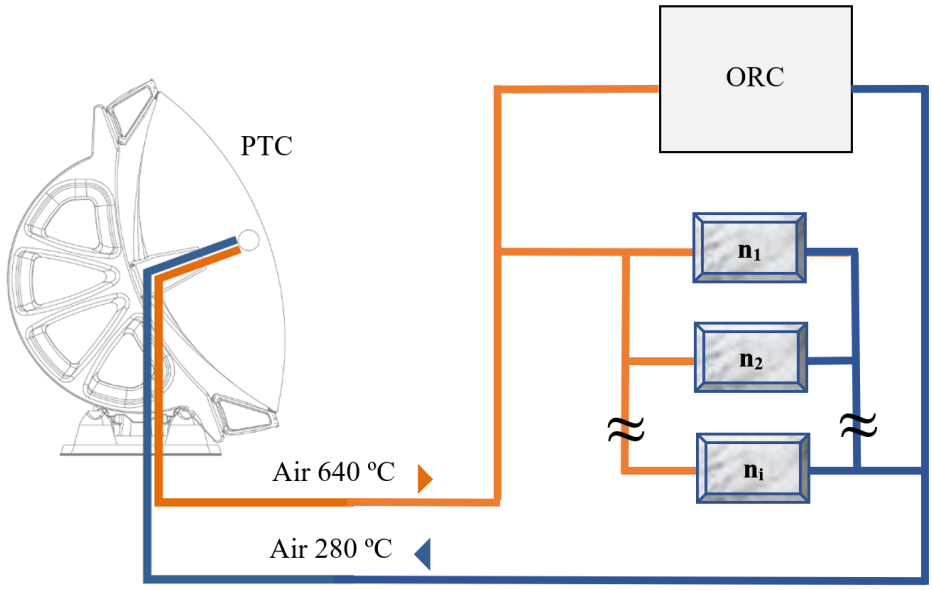

Figure 5-9. Up-scaled scheme of parallel TES module rows, PTC (Parabolic Trough Collector) and ORC (Organic Rankine Cycle).

The optimized arrangement comprises 1200 modules, each with a length of 4 m, and has a nominal capacity of 36.58 MWh_{th} and an energy density of 1791.8 MJ/m^3. In comparison, the Ait Baha plant's TES capacity is 100 MWh_{th} and has an energy density of 944.4 MJ/m^3. The energy densities are based on the total volumes of the respective systems: 73.5 m^3 for the concrete modules and 381.2 m^3 for the packed bed of rocks. The mentioned capacity was determined using a nominal ambient temperature to HTF inlet temperature method. The solid TES system demonstrates a higher energy density in terms of MJ/m^3, which makes it more efficient in terms of storing thermal energy per unit volume. This advantage in energy density could be attributed to the material properties here considered and, to a lesser extent, the modular design of the concrete block TES system.

However, it is essential to note that while the energy density is a principal factor, it may not be the only criterion to consider when comparing these TES systems. Each system has its unique set of advantages and limitations, and what may be of importance in a case may not be the same with another application, site conditions, or performance requirements.

In resume, the study highlights the transformative potential of integrating ML and MOO techniques for enhancing solid-state TES units. The decision tree model employed in the study accurately predicts essential performance parameters of TES units, demonstrating robustness and high predictive accuracy. The combination of ML and MCDA enables the identification of optimized design parameters and operational conditions. The TPE algorithm for MOO facilitates concurrent optimization of multiple performance metrics, leading to Pareto optimal solutions that balance conflicting objectives. Numerical simulations further validate the ML- and MCDA-derived optimized design parameters. The trained ML algorithm exhibits flexibility and scalability, enabling the processing of vast amounts of data and managing a wider range of design configurations. The modular design and parallel setup of TES units contribute to system scalability, flexibility, and ease of maintenance. The optimized arrangement of 1200 modules demonstrate superior performance, with a capacity of 36.58 MWhthermal and an energy density of 1791.8 MJ/m3. The findings underscore the promising role of AI, ML, and MOO in enhancing TES technology, with the potential to improve performance, reduce costs, and mitigate environmental impact.

Conclusion : Summary, Implications, and Future Work

This research sets out to develop and optimize thermal energy storage (TES) solutions that use geopolymer (GEO) concrete, an alternative to ordinary Portland cement (OPC) in terms of sustainability and performance. With the successful use of thermal modeling and experimental validation, the potential of GEO concrete as a more efficient TES material is clearly evidenced, especially for higher temperature applications (>400ºC).

In **Chapter II**, the study put forth GEO concrete as an alternative to OPC for TES applications by means of numerical simulation.

1. Prepared GEO concrete samples by mixing fly ash, blast furnace slag, alkaline wastewater, and 20% Portland cement. Cast cylindrical samples.
2. Experimentally measured specific heat capacity of GEO samples up to 400°C using differential scanning calorimetry.
3. Experimentally measured thermal diffusivity of GEO samples using laser flash analysis. Normalized values using reference OPC sample.
4. Defined properties of two hypothetical OPC concretes (OPC-1 and OPC-2) by extrapolating literature data on OPC beyond 400°C.
5. Developed 2D finite element model (FEM) of concrete block with embedded tube to simulate heat transfer. Used measured GEO properties.
6. Simulated and compared thermal performance of GEO, OPC-1 and OPC-2 concrete blocks for various initial temperatures and inlet temperatures. Calculated average temperature and stored energy over time.
7. Simulated performance over repeated charge/discharge cycles between 290-565°C and 290-700°C. Compared temperature differences and storage capacity between materials.
8. Modeled transient heat transfer at different points inside the numerical concrete blocks during charging and discharging to analyze temperature distribution.

9. The model results serve as a proof of concept. Experimental testing of OPC and geopolymer concrete TES prototypes is also planned.

Chapter III covered the experimental validation of the prototypes.

1. Prepared 10cm cube samples of GEO concrete and OPC concrete. GEO used a specific cement blend with steel slag aggregate while OPC used a standard formulation.
2. Cured samples for 90 days to ensure adequate strength development. Assessed compressive strength.
3. Fabricated steel pipe test modules with concrete samples cast around them. Added temperature probes in the concrete to monitor temperature.
4. Developed test facility with air heater and circulation pump to deliver hot air through the pipe and concrete modules. Insulated prototypes to prevent heat loss.
5. Conducted tests with two temperature ranges:
   - Low (200-450°C)
   - High (200-600°C)
6. Ran startup preheating for 10 hours up to 120°C to prevent thermal shock. Increased to test temperatures gradually over hours.
7. Performed 4 full thermal cycles for each temperature range, monitoring concrete temperatures. Each cycle was ~24 hours of charging and discharging.
8. Analyzed performance metrics like temperature profiles, maximum temperatures attained, and thermal storage capacity.
9. Compared GEO and OPC concrete metrics to evaluate relative performance. GEO showed 30-40°C higher temperatures and 2-3.5x higher storage capacity.

In **Chapter IV**, a comprehensive 3D computational model was developed to simulate the performance of geopolymer-based TES systems. It provided an effective tool for design optimization, scalability assessments, and performance prediction.

1. Developed a 3D computational model using COMSOL Multiphysics to simulate the performance of geopolymer-based thermal energy storage (TES) systems. Validated the model against experimental data.
2. Conducted a parametric study evaluating the effects of various design parameters (air velocity, tube diameter, module size, shape configuration.) on TES system performance, both with and without metallic tubes.
3. Compared modular TES designs with and without metallic tubes to determine which configuration provided better heat transfer and storage capacity. Found the tubeless design performed better.
4. Analyzed the effect of concrete surface roughness on turbulent air flow and heat transfer using the sand-grain method. Simulated different roughness heights to study their impact.
5. Used optimization techniques and Pearson's correlation analysis to identify the most influential parameters and optimal configurations to maximize TES system efficiency and storage capacity.

The developed model enables systematic evaluation of design choices and operating parameters to maximize the performance of not only concrete based but also any solid based TES systems.

Finally, **Chapter V** explored the effective combination of machine learning and multi-objective optimization for the up scaled design and optimizations of the TES system. The workaround was introduced as an approach for TES design and optimization as a general practice.

1. Using laboratory investigations and developed numerical model in Chapter IV to gather data on the thermal energy storage (TES) system's performance.
2. Developed and validated a numerical model of the TES system using COMSOL Multiphysics.
3. Used the validated model to generate datasets with diverse combinations of design parameters and operating conditions.
4. Preprocessed the heterogeneous datasets and used them to train a decision tree machine learning (ML) model to predict TES performance metrics.

5. Evaluated the ML model's accuracy using metrics like R-squared, MSE, MAE etc. and tuned hyperparameters.
6. Employed multi-objective optimization using the Tree-Structured Parzen Estimator (TPE) algorithm to identify Pareto optimal solutions balancing objectives like efficiency and pressure drop.
7. Validated the optimized design parameters through comparison with numerical simulation results in COMSOL.
8. Proposed a modular and parallel arrangement of 1200 concrete TES modules for the case study CSP plant, with superior capacity and energy density compared to already installed TES system.

The integrated ML and multi-objective optimization methodology demonstrates promise for improving TES technology performance, reducing costs, lowering environmental impact, and enhancing integration with renewable energy systems. The framework's flexibility, scalability and validation through simulations make a compelling case for its effectiveness. Further testing across diverse operating conditions and plant configurations would strengthen confidence. In conclusion, this research offers original contributions to the field of thermal energy storage by introducing and evaluating a new material, geopolymer concrete.

The research did an effort and charted new paths in TES technology, laying the groundwork for continued exploration, especially for high-temperature applications (>400ºC). Some potential real-world applications of the **research findings** include:

1. Using geopolymer concrete for thermal energy storage systems in concentrated solar power plants. The improved heat storage capacity and thermal stability demonstrated could allow CSP plants to operate more efficiently.

2. Applying geopolymer concrete thermal energy storage for industrial waste heat recovery and reuse. Many industrial processes produce excess low-grade heat that could be stored and reutilized.

3. Integration of geopolymer concrete thermal storage into combined heating and power (CHP) systems to balance electric and thermal loads. The stored heat could be used for district heating applications when electricity demand is low.

4. Employing machine learning techniques like those developed in the study to optimize configurations of thermal energy storage systems using phase change materials, thermochemical materials, etc. beyond geopolymers.

5. Replacing ordinary Portland cement concrete with geopolymer concrete for applications like steam accumulator vessels, thermal reservoirs, and containment structures that involve high temperatures and pressures.

There are several **key implications**:

1. Geopolymer concrete has the potential to replace conventional concrete as the material of choice for high-temperature TES systems. This could significantly improve the efficiency and sustainability of concentrated solar power plants, industrial waste heat recovery systems, and other technologies relying on TES.

2. Further research and pilot projects should focus on continued optimization and real-world testing of geopolymer TES systems for different use cases. The promising lab results warrant further validation and refinement.

3. If implemented at scale, geopolymer TES could provide environmental benefits by reducing reliance on Portland cement concrete, which has a high carbon footprint. This aligns with global decarbonization efforts.

4. The machine learning techniques developed could be applied to optimize other novel TES designs and configurations using different phase change or thermochemical materials beyond geopolymers. This demonstrates a methodology for accelerating sustainable energy technology development.

5. There is potential for expanded applications of geopolymer concrete in general construction and infrastructure projects requiring high temperature and pressure stability. The TES use case highlights the overall capabilities of this material.

Some **potential future research** directions:

1. Test scaled-up geopolymer concrete TES systems in real-world conditions - The current study was limited to lab prototypes. Evaluating performance in pilot demonstrations is an important next step.

2. Explore additional geopolymer formulations and compositions - Only one mix was evaluated here. Further optimizing the concrete properties could enhance TES performance.

3. Long-duration testing over months/years - The current study was relatively short-term. Understanding durability and cyclic behavior over extended operation is critical.

4. Techno-economic analysis and life cycle assessment - Evaluating the practical viability and environmental impact of full-scale systems will inform adoption.

5. Physical testing of machine learning optimized designs - The ML results provide theoretical configurations that should be physically validated.

6. Incorporate additional parameters into ML model - Expanding beyond current factors could improve predictions and reveal new optimization opportunities.

7. Apply techniques to optimize novel TES materials - The methods could inform development of other storage options beyond geopolymers.

Appendix A

Grid Independence Test for Numerical GEO Model

This appendix provides an analysis of the grid independence of the numerical model presented in Section 2.4 of the thesis "Geopolymer as TES Material". The goal of this analysis is to determine the minimum mesh element size required for the model to produce reliable and accurate results.

A triangular quadratic mesh was employed in the numerical model. To assess the dependency of numerical outcomes on the mesh element size, a simulation was conducted under the assumption that the module initially maintains a temperature of 200 °C while the inlet temperature (T_{inlet}) equals 700 °C. After a six-hour period, the average temperature of three different materials was calculated. Subsequently, the average temperature ($T_{average}$) was compared for various element sizes and runs. The A-1 formula calculates the difference in temperature between subsequent iterations of the numerical model.

$$Difference = \frac{T_{average,n+1} - T_{average,n}}{n} \quad \text{(A-1)}$$

Figure A-1 below demonstrates that for a range of 40,000 to 50,000 elements, the difference between $T_{average}$ values from different runs (different element numbers) is less than 0.1%. This implies that a numerical model with this range of element sizes can produce reliable and accurate results.

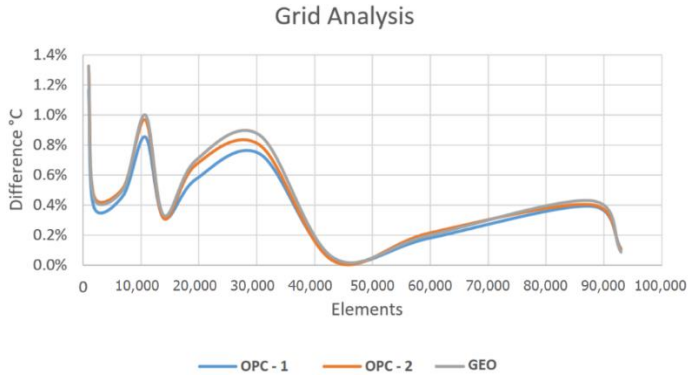

Figure A-1. Grid Dependency Analysis

To assess the shape quality of the mesh elements, the aspect ratio of the elements (the ratio of the smallest to the largest dimension of an element) was calculated and plotted against the element size (Figure A-2). The aspect ratio was found to approach a value of 1 as the element size increased, indicating that the mesh elements were becoming more equilateral. This improvement in shape quality is reflected in the average element shape quality, which also approached a value of 1 as the element size increased.

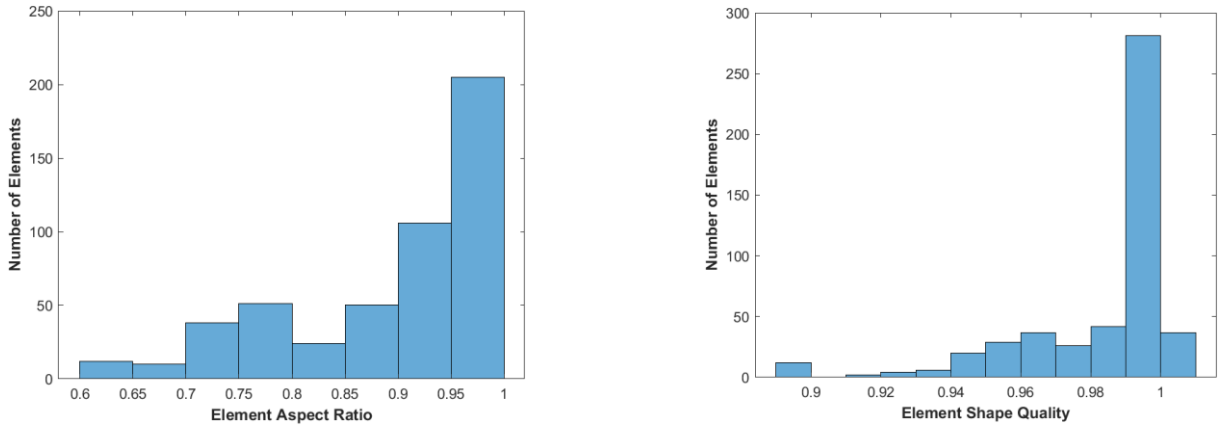

(A) Aspect Ratio (B) Shape Quality

Figure A-2. Element Quality Assessments.

(A) Aspect Ratio (ratio of minimal to maximal dimensions of an element) observed based on geometry and element size growth. (B) Element shape quality for mesh with 6924 elements. The quality values are numbers from 0 through 1, where 1 corresponds to the optimal shape of the element.

Based on these results, it is concluded that a mesh with approximately 40,000 to 50,000 triangular quadratic elements is sufficient for the numerical model to produce reliable and accurate results. Simulation used 45,000 triangular quadratic elements yields results with deviations less than 0.1% according to Figure A-1. However, the meshing process should also consider factors such as CPU usage time and computational efficiency.

References

1.10. Decision Trees [WWW Document], n.d. . Scikit-Learn. URL https://scikit-learn/stable/modules/tree.html (accessed 1.22.23).

Abdalla, A.N., Nazir, M.S., Tao, H., Cao, S., Ji, R., Jiang, M., Yao, L., 2021. Integration of energy storage system and renewable energy sources based on artificial intelligence: An overview. J. Energy Storage 40, 102811. https://doi.org/10.1016/j.est.2021.102811

Abualigah, L., Zitar, R.A., Almotairi, K.H., Hussein, A.M., Abd Elaziz, M., Nikoo, M.R., Gandomi, A.H., 2022. Wind, Solar, and Photovoltaic Renewable Energy Systems with and without Energy Storage Optimization: A Survey of Advanced Machine Learning and Deep Learning Techniques. Energies 15, 578. https://doi.org/10.3390/en15020578

Achenbach, E., 1977. The effect of surface roughness on the heat transfer from a circular cylinder to the cross flow of air. Int. J. Heat Mass Transf. 20, 359–369. https://doi.org/10.1016/0017-9310(77)90157-0

Akiba, T., Sano, S., Yanase, T., Ohta, T., Koyama, M., 2019. Optuna: A Next-generation Hyperparameter Optimization Framework, in: Proceedings of the 25th ACM SIGKDD International Conference on Knowledge Discovery & Data Mining, KDD '19. Association for Computing Machinery, New York, NY, USA, pp. 2623–2631. https://doi.org/10.1145/3292500.3330701

Allen, A.J., Thomas, J.J., Jennings, H.M., 2007. Composition and density of nanoscale calcium–silicate–hydrate in cement. Nat. Mater. 6, 311–316. https://doi.org/10.1038/nmat1871

Alonso, M.C., Vera-Agullo, J., Guerreiro, L., Flor-Laguna, V., Sanchez, M., Collares-Pereira, M., 2016. Calcium aluminate based cement for concrete to be used as thermal energy storage in solar thermal electricity plants. Cem. Concr. Res. 82, 74–86. https://doi.org/10.1016/j.cemconres.2015.12.013

Alva, G., Liu, L., Huang, X., Fang, G., 2017. Thermal energy storage materials and systems for solar energy applications. Renew. Sustain. Energy Rev. 68, 693–706. https://doi.org/10.1016/j.rser.2016.10.021

Andic, O., Copuroglu, O., Ramyar, K., 2008. Effect of high temperature on mechanical and microstructural properties of cement mortar. 11th Conf. Durab. Build. Mater. Compon. 527–533.

ANSYS Fluent, n.d.

Aupoix, B., 2015. Improved heat transfer predictions on rough surfaces. Int. J. Heat Fluid Flow 56, 160–171. https://doi.org/10.1016/j.ijheatfluidflow.2015.07.007

Bajpai, R., Choudhary, K., Srivastava, A., Sangwan, K.S., Singh, M., 2020. Environmental impact assessment of fly ash and silica fume based geopolymer concrete. J. Clean. Prod. 254, 120147. https://doi.org/10.1016/j.jclepro.2020.120147

Barzegar, M., Goracci, G., Martauz, P., Dolado, J.S., 2024. Sustainable geopolymer concrete for thermoelectric energy harvesting. Constr. Build. Mater. 411, 134398. https://doi.org/10.1016/j.conbuildmat.2023.134398

Bauer, T., Steinmann, W.-D., Laing, D., Tamme, R., 2012. THERMAL ENERGY STORAGE MATERIALS AND SYSTEMS. Annu. Rev. Heat Transf. 15, 131–177. https://doi.org/10.1615/AnnualRevHeatTransfer.2012004651

Becattini, V., Motmans, T., Zappone, A., Madonna, C., Haselbacher, A., Steinfeld, A., 2017. Experimental investigation of the thermal and mechanical stability of rocks for high-temperature thermal-energy storage. Appl. Energy 203, 373–389. https://doi.org/10.1016/j.apenergy.2017.06.025

Beine, B., Bitterlich, W., Dinter, F., 1989. Feasibility study for the concepts of a 200 MWh thermal energy storage with solid salt plates, concrete plates and phase change salts as storage media, final report.

Benti, N.E., Chaka, M.D., Semie, A.G., 2023. Forecasting Renewable Energy Generation with Machine Learning and Deep Learning: Current Advances and Future Prospects. Sustainability 15, 7087. https://doi.org/10.3390/su15097087

Bergan, P.G., Greiner, C.J., 2014. A New Type of Large Scale Thermal Energy Storage. Energy Procedia 58, 152–159. https://doi.org/10.1016/j.egypro.2014.10.422

Boquera, L., Castro, J.R., Pisello, A.L., Cabeza, L.F., 2021a. Research progress and trends on the use of concrete as thermal energy storage material through bibliometric analysis. J. Energy Storage 38, 102562. https://doi.org/10.1016/j.est.2021.102562

Boquera, L., Castro, J.R., Pisello, A.L., Cabeza, L.F., 2021b. Research progress and trends on the use of concrete as thermal energy storage material through bibliometric analysis. J. Energy Storage 38, 102562. https://doi.org/10.1016/j.est.2021.102562

Borri, E., Zsembinszki, G., Cabeza, L.F., 2021. Recent developments of thermal energy storage applications in the built environment: A bibliometric analysis and systematic review. Appl. Therm. Eng. 189, 116666. https://doi.org/10.1016/j.applthermaleng.2021.116666

Bose, B.K., 2017. Artificial Intelligence Techniques in Smart Grid and Renewable Energy Systems—Some Example Applications. Proc. IEEE 105, 2262–2273. https://doi.org/10.1109/JPROC.2017.2756596

Breiman, L., 2017. Classification and Regression Trees.

Breiman, L., 2001. Random Forests. Mach. Learn. 45, 5–32. https://doi.org/10.1023/A:1010933404324

Brückner, S., Liu, S., Miró, L., Radspieler, M., Cabeza, L.F., Lävemann, E., 2015a. Industrial waste heat recovery technologies: An economic analysis of heat transformation technologies. Appl. Energy 151, 157–167. https://doi.org/10.1016/j.apenergy.2015.01.147

Brückner, S., Liu, S., Miró, L., Radspieler, M., Cabeza, L.F., Lävemann, E., 2015b. Industrial waste heat recovery technologies: An economic analysis of heat transformation technologies. Appl. Energy 151, 157–167. https://doi.org/10.1016/j.apenergy.2015.01.147

Burgaleta, J., Arias, S., Ramirez, D., 2011. Gemasolar, the first tower thermosolar commercial plant with molten salt storage. Solarpaces 69.

Buscemi, A., Panno, D., Ciulla, G., Beccali, M., Lo Brano, V., 2018. Concrete thermal energy storage for linear Fresnel collectors: Exploiting the South Mediterranean's

solar potential for agri-food processes. Energy Convers. Manag. 166, 719–734. https://doi.org/10.1016/j.enconman.2018.04.075
Cabeza, L.F. (Ed.), 2020a. Advances in thermal energy storage systems: methods and applications, Second edition. ed, Woodhead publishing series in energy. Woodhead Publishing, Duxford, United Kingdom ; Cambridge, MA.
Cabeza, L.F. (Ed.), 2020b. Advances in thermal energy storage systems: methods and applications, Second edition. ed, Woodhead publishing series in energy. Duxford, United Kingdom ; Cambridge, MA.
Cabeza, L.F., 2012a. Thermal Energy Storage, in: Comprehensive Renewable Energy. Elsevier, pp. 211–253.
Cabeza, L.F., 2012b. Thermal Energy Storage, in: Comprehensive Renewable Energy. pp. 211–253.
Cabeza, L.F., Vérez, D., Zsembinszki, G., Borri, E., Prieto, C., 2022a. Key Challenges for High Temperature Thermal Energy Storage in Concrete—First Steps towards a Novel Storage Design. Energies 15, 4544. https://doi.org/10.3390/en15134544
Cabeza, L.F., Vérez, D., Zsembinszki, G., Borri, E., Prieto, C., 2022b. Key Challenges for High Temperature Thermal Energy Storage in Concrete—First Steps towards a Novel Storage Design. Energies 15, 4544. https://doi.org/10.3390/en15134544
Cabeza, L.F., Vérez, D., Zsembinszki, G., Borri, E., Prieto, C., 2022c. Key Challenges for High Temperature Thermal Energy Storage in Concrete—First Steps towards a Novel Storage Design. Energies 15, 4544. https://doi.org/10.3390/en15134544
CARNAVOS, T.C., 1980. Heat Transfer Performance of Internally Finned Tubes in Turbulent Flow. Heat Transf. Eng. 1, 32–37. https://doi.org/10.1080/01457638008939566
Cebeci, T., 2004. Analysis of turbulent flows, 2nd rev. and expanded ed. ed. Elsevier, Amsterdam.
Chandan, R.R., C.r, A., G., C.S., Elankeerthana, R., Anitha, K., Sabitha, R., Sathyamurthy, R., Mohanavel, V., Sudhakar, M., 2022. Machine learning Technique for improving the stability of Thermal Energy storage. Energy Rep., The 2022 International Conference on Energy Storage Technology and Power Systems 8, 897–907. https://doi.org/10.1016/j.egyr.2022.09.205
Chen, C., Hu, Y., Karuppiah, M., Kumar, P.M., 2021. Artificial intelligence on economic evaluation of energy efficiency and renewable energy technologies. Sustain. Energy Technol. Assess. 47, 101358. https://doi.org/10.1016/j.seta.2021.101358
Chen, Y., Galal, K., Athienitis, A.K., 2010. Modeling, design and thermal performance of a BIPV/T system thermally coupled with a ventilated concrete slab in a low energy solar house: Part 2, ventilated concrete slab. Sol. Energy 84, 1908–1919. https://doi.org/10.1016/j.solener.2010.06.012
COMSOL Multiphysics® v. 6.1., n.d.
COMSOL Multiphysics, n.d.
Cuesta, A., Ayuela, A., Aranda, M.A.G., 2021. Belite cements and their activation. Cem. Concr. Res. 140, 106319. https://doi.org/10.1016/j.cemconres.2020.106319
Darcy, H., 1857. Recherches expérimentales relatives au mouvement de l’eau dans les tuyaux. Mallet-Bachelier.
DEB, K., 2012. OPTIMIZATION FOR ENGINEERING DESIGN: Algorithms and Examples. PHI Learning Pvt. Ltd.

Deb, K., 2011. Multi-objective Optimisation Using Evolutionary Algorithms: An Introduction, in: Wang, L., Ng, A.H.C., Deb, K. (Eds.), Multi-Objective Evolutionary Optimisation for Product Design and Manufacturing. Springer, London, pp. 3–34. https://doi.org/10.1007/978-0-85729-652-8_1

Dumont, O., Frate, G.F., Pillai, A., Lecompte, S., De Paepe, M., Lemort, V., 2020. Carnot battery technology: A state-of-the-art review. J. Energy Storage 32, 101756. https://doi.org/10.1016/j.est.2020.101756

Duxson, P., Fernández-Jiménez, A., Provis, J.L., Lukey, G.C., Palomo, A., van Deventer, J.S.J., 2007. Geopolymer technology: the current state of the art. J. Mater. Sci. 42, 2917–2933. https://doi.org/10.1007/s10853-006-0637-z

Fallahi, A., Haghighat, F., Elsadi, H., 2010. Energy performance assessment of double-skin façade with thermal mass. Energy Build. 42, 1499–1509. https://doi.org/10.1016/j.enbuild.2010.03.020

Famiglietti, A., Lecuona-Neumann, A., Nogueira, J., Rahjoo, M., 2020. Direct solar production of medium temperature hot air for industrial applications in linear concentrating solar collectors using an open Brayton cycle. Viability analysis. Appl. Therm. Eng. 169, 114914. https://doi.org/10.1016/j.applthermaleng.2020.114914

Fernandez, A.I., Martínez, M., Segarra, M., Martorell, I., Cabeza, L.F., 2010. Selection of materials with potential in sensible thermal energy storage. Sol. Energy Mater. Sol. Cells 94, 1723–1729. https://doi.org/10.1016/j.solmat.2010.05.035

Ferone, C., Colangelo, F., Frattini, D., Roviello, G., Cioffi, R., Maggio, R., 2014. Finite Element Method Modeling of Sensible Heat Thermal Energy Storage with Innovative Concretes and Comparative Analysis with Literature Benchmarks. Energies 7, 5291–5316. https://doi.org/10.3390/en7085291

Fraisse, G., Ménézo, C., Johannes, K., 2007. Energy performance of water hybrid PV/T collectors applied to combisystems of Direct Solar Floor type. Sol. Energy 81, 1426–1438. https://doi.org/10.1016/j.solener.2006.11.017

Frattini, D., Occhicone, A., Ferone, C., Cioffi, R., 2021. Fibre-Reinforced Geopolymer Concretes for Sensible Heat Thermal Energy Storage: Simulations and Environmental Impact. Materials 14, 414. https://doi.org/10.3390/ma14020414

Fürnkranz, J., 2010. Decision Tree, in: Sammut, C., Webb, G.I. (Eds.), Encyclopedia of Machine Learning. Springer US, Boston, MA, pp. 263–267. https://doi.org/10.1007/978-0-387-30164-8_204

Ge, Z., Li, Y., Li, D., Sun, Z., Jin, Y., Liu, C., Li, C., Leng, G., Ding, Y., 2014. Thermal energy storage: Challenges and the role of particle technology. Particuology, Energy storage: Materials and processes 15, 2–8. https://doi.org/10.1016/j.partic.2014.03.003

Gil, A., Medrano, M., Martorell, I., Lázaro, A., Dolado, P., Zalba, B., Cabeza, L.F., 2010. State of the art on high temperature thermal energy storage for power generation. Part 1—Concepts, materials and modellization. Renew. Sustain. Energy Rev. 14, 31–55. https://doi.org/10.1016/j.rser.2009.07.035

Gong, M., Ottermo, F., 2022. High-temperature thermal storage in combined heat and power plants. Energy 252, 124057. https://doi.org/10.1016/j.energy.2022.124057

González-Roubaud, E., Pérez-Osorio, D., Prieto, C., 2017. Review of commercial thermal energy storage in concentrated solar power plants: Steam vs. molten salts.

Renew. Sustain. Energy Rev. 80, 133–148. https://doi.org/10.1016/j.rser.2017.05.084
Graves, A., Mohamed, A., Hinton, G., 2013. Speech Recognition with Deep Recurrent Neural Networks. https://doi.org/10.48550/arXiv.1303.5778
Guerrero, A., Goñi, S., Moragues, A., Dolado, J.S., 2005. Microstructure and Mechanical Performance of Belite Cements from High Calcium Coal Fly Ash. J. Am. Ceram. Soc. 88, 1845–1853. https://doi.org/10.1111/j.1551-2916.2005.00344.x
Gunasekara, S.N., Barreneche, C., Inés Fernández, A., Calderón, A., Ravotti, R., Ristić, A., Weinberger, P., Ömur Paksoy, H., Koçak, B., Rathgeber, C., Ningwei Chiu, J., Stamatiou, A., 2021a. Thermal Energy Storage Materials (TESMs)—What Does It Take to Make Them Fly? Crystals 11, 1276. https://doi.org/10.3390/cryst11111276
Gunasekara, S.N., Barreneche, C., Inés Fernández, A., Calderón, A., Ravotti, R., Ristić, A., Weinberger, P., Ömur Paksoy, H., Koçak, B., Rathgeber, C., Ningwei Chiu, J., Stamatiou, A., 2021b. Thermal Energy Storage Materials (TESMs)—What Does It Take to Make Them Fly? Crystals 11, 1276. https://doi.org/10.3390/cryst11111276
Hagen, G.H.L., 1854. Über den einfluss der temperatur auf die bewegung des wassers in röhren–. Druckerei der Königl. akademie der wissenschaften.
Hahn, D.W., Özisik, M.N., 2012. Heat Conduction. Hoboken, NJ.
He, R., Dai, N., Wang, Z., 2020. Thermal and Mechanical Properties of Geopolymers Exposed to High Temperature: A Literature Review. Adv. Civ. Eng. 2020, 1–17. https://doi.org/10.1155/2020/7532703
He, Z., Guo, W., Zhang, P., 2022. Performance prediction, optimal design and operational control of thermal energy storage using artificial intelligence methods. Renew. Sustain. Energy Rev. 156, 111977. https://doi.org/10.1016/j.rser.2021.111977
Hoivik, N., Greiner, C., Barragan, J., Iniesta, A.C., Skeie, G., Bergan, P., Blanco-Rodriguez, P., Calvet, N., 2019. Long-term performance results of concrete-based modular thermal energy storage system. J. Energy Storage 24, 100735. https://doi.org/10.1016/j.est.2019.04.009
Hoivik, N., Greiner, C., Tirado, E.B., Barragan, J., Bergan, P., Skeie, G., Blanco, P., Calvet, N., 2017. Demonstration of EnergyNest thermal energy storage (TES) technology. Presented at the SOLARPACES 2016: International Conference on Concentrating Solar Power and Chemical Energy Systems, Abu Dhabi, United Arab Emirates, p. 080011. https://doi.org/10.1063/1.4984432
Ings, J.B., Brown, P.W., 1982. An evaluation of hydrated calcium aluminate compounds as energy storage media. NASA STIRecon Tech. Rep. N 83, 19308.
Innovation outlook: Thermal energy storage [WWW Document], 2020. URL https://www.irena.org/publications/2020/Nov/Innovation-outlook-Thermal-energy-storage (accessed 9.22.23).
IRENA, I.O., 2020. Thermal energy storage. Int. Renew. Energy Agency Abu Dhabi.
Irico, S., Mutke, S., Bertola, F., Gastaldi, D., Capelli, L., Canonico, F., 2022. Durability of high belite cement as new technical solution for concrete. Acta Polytech. CTU Proc. 33, 245–249. https://doi.org/10.14311/APP.2022.33.0245

Jiménez, J., 2004. TURBULENT FLOWS OVER ROUGH WALLS. Annu. Rev. Fluid Mech. 36, 173–196. https://doi.org/10.1146/annurev.fluid.36.050802.122103
John, E.E., Hale, W.M., Selvam, R.P., 2010. Effect of High Temperatures and Heating Rates on High Strength Concrete for Use as Thermal Energy Storage. Presented at the ASME 2010 4th International Conference on Energy Sustainability, American Society of Mechanical Engineers Digital Collection, pp. 709–713. https://doi.org/10.1115/ES2010-90096
Kadivar, M., Tormey, D., McGranaghan, G., 2021. A review on turbulent flow over rough surfaces: Fundamentals and theories. Int. J. Thermofluids 10, 100077. https://doi.org/10.1016/j.ijft.2021.100077
Kandlikar, S.G., Joshi, S., Tian, S., 2003. Effect of Surface Roughness on Heat Transfer and Fluid Flow Characteristics at Low Reynolds Numbers in Small Diameter Tubes. Heat Transf. Eng. 24, 4–16. https://doi.org/10.1080/01457630304069
Khamis, A., 2024. Optimization Algorithms: AI Techniques for Design, Planning, and Control Problems. Manning Publications.
Klein, S.J.W., 2013. Multi-Criteria Decision Analysis of Concentrated Solar Power with Thermal Energy Storage and Dry Cooling. Environ. Sci. Technol. 47, 13925–13933. https://doi.org/10.1021/es403553u
Koçak, B., Fernandez, A.I., Paksoy, H., 2020. Review on sensible thermal energy storage for industrial solar applications and sustainability aspects. Sol. Energy 209, 135–169. https://doi.org/10.1016/j.solener.2020.08.081
Kochenderfer, M.J., Wheeler, T.A., 2019. Algorithms for Optimization. Cambridge.
Kotsiantis, S.B., 2013. Decision trees: a recent overview. Artif. Intell. Rev. 39, 261–283. https://doi.org/10.1007/s10462-011-9272-4
Kraftblock, n.d. . STORWORKS POWER. URL https://kraftblock.com/en/technology.html
Krogstad, P.-Å., Antonia, R.A., Browne, L.W.B., 1992. Comparison between rough- and smooth-wall turbulent boundary layers. J. Fluid Mech. 245, 599. https://doi.org/10.1017/S0022112092000594
Krogstadt, P.-Å., Antonia, R.A., 1999. Surface roughness effects in turbulent boundary layers. Exp. Fluids 27, 450–460. https://doi.org/10.1007/s003480050370
Kuravi, S., Trahan, J., Goswami, D.Y., Rahman, M.M., Stefanakos, E.K., 2013. Thermal energy storage technologies and systems for concentrating solar power plants. Prog. Energy Combust. Sci. 39, 285–319. https://doi.org/10.1016/j.pecs.2013.02.001
Lai, J.-P., Chang, Y.-M., Chen, C.-H., Pai, P.-F., 2020. A Survey of Machine Learning Models in Renewable Energy Predictions. Appl. Sci. 10, 5975. https://doi.org/10.3390/app10175975
Laing, D., Bahl, C., Bauer, T., Fiss, M., Breidenbach, N., Hempel, M., 2012. High-Temperature Solid-Media Thermal Energy Storage for Solar Thermal Power Plants. Proc. IEEE 100, 516–524. https://doi.org/10.1109/JPROC.2011.2154290
Laing, D., Lehmann, D., Bahl, C., 2008. CONCRETE STORAGE FOR SOLAR THERMAL POWER PLANTS AND INDUSTRIAL PROCESS HEAT, in: Third International Renewable Energy Storage Conference (IRES 2008). Berlin.

Laing, D., Steinmann, W.-D., Tamme, R., Richter, C., 2006. Solid media thermal storage for parabolic trough power plants. Sol. Energy 80, 1283–1289. https://doi.org/10.1016/j.solener.2006.06.003

Lavagna, L., Burlon, D., Nisticò, R., Brancato, V., Frazzica, A., Pavese, M., Chiavazzo, E., 2020a. Cementitious composite materials for thermal energy storage applications: a preliminary characterization and theoretical analysis. Sci. Rep. 10, 12833. https://doi.org/10.1038/s41598-020-69502-0

Lavagna, L., Burlon, D., Nisticò, R., Brancato, V., Frazzica, A., Pavese, M., Chiavazzo, E., 2020b. Cementitious composite materials for thermal energy storage applications: a preliminary characterization and theoretical analysis. Sci. Rep. 10, 12833. https://doi.org/10.1038/s41598-020-69502-0

Lee, D., Ooka, R., Matsuda, Y., Ikeda, S., Choi, W., 2022. Experimental analysis of artificial intelligence-based model predictive control for thermal energy storage under different cooling load conditions. Sustain. Cities Soc. 79, 103700. https://doi.org/10.1016/j.scs.2022.103700

Lehmann, B., Dorer, V., Koschenz, M., 2007. Application range of thermally activated building systems tabs. Energy Build. 39, 593–598. https://doi.org/10.1016/j.enbuild.2006.09.009

Lin, Y., Li, B., Moiser, T.M., Griffel, L.M., Mahalik, M.R., Kwon, J., Alam, S.M.S., 2022. Revenue prediction for integrated renewable energy and energy storage system using machine learning techniques. J. Energy Storage 50, 104123. https://doi.org/10.1016/j.est.2022.104123

Liu, G.R., Quek, S.S. (Eds.), 2014a. The Finite Element Method, in: The Finite Element Method (Second Edition). Butterworth-Heinemann, Oxford, p. i. https://doi.org/10.1016/B978-0-08-098356-1.00014-X

Liu, G.R., Quek, S.S., 2014b. Chapter 12 - FEM for Heat Transfer Problems, in: Liu, G.R., Quek, S.S. (Eds.), The Finite Element Method (Second Edition). Butterworth-Heinemann, Oxford, pp. 347–396. https://doi.org/10.1016/B978-0-08-098356-1.00012-6

Lolli, F., Manzano, H., Provis, J.L., Bignozzi, M.C., Masoero, E., 2018. Atomistic Simulations of Geopolymer Models: The Impact of Disorder on Structure and Mechanics. ACS Appl. Mater. Interfaces 10, 22809–22820. https://doi.org/10.1021/acsami.8b03873

Malakouti, S.M., 2023. Use machine learning algorithms to predict turbine power generation to replace renewable energy with fossil fuels. Energy Explor. Exploit. 41, 836–857. https://doi.org/10.1177/01445987221138135

Martauz, P., Janotka, I., Strigáč, J., Bačuvčík, M., 2016. Fundamental properties of industrial hybrid cement: utilization in ready-mixed concretes and shrinkage-reducing applications. Mater. Constr. 66, e084. https://doi.org/10.3989/mc.2016.04615

Martins, M., Villalobos, U., Delclos, T., Armstrong, P., Bergan, P.G., Calvet, N., 2015. New Concentrating Solar Power Facility for Testing High Temperature Concrete Thermal Energy Storage. Energy Procedia 75, 2144–2149. https://doi.org/10.1016/j.egypro.2015.07.350

Masliyah, J.H., Nandakumar, K., 1976. Heat Transfer in Internally Finned Tubes. J. Heat Transf. 98, 257–261. https://doi.org/10.1115/1.3450528

MATLAB, 2020. MATLAB (R2020b). The MathWorks Inc., Natick, Massachusetts.
MATLAB, n.d.
Mikkelson, D., Doster, J.M., 2022. Investigation of two concrete thermal energy storage system configurations for continuous power production. J. Energy Storage 51, 104387. https://doi.org/10.1016/j.est.2022.104387
Miró, L., Gasia, J., Cabeza, L.F., 2016a. Thermal energy storage (TES) for industrial waste heat (IWH) recovery: A review. Appl. Energy 179, 284–301. https://doi.org/10.1016/j.apenergy.2016.06.147
Miró, L., Gasia, J., Cabeza, L.F., 2016b. Thermal energy storage (TES) for industrial waste heat (IWH) recovery: A review. Appl. Energy 179, 284–301. https://doi.org/10.1016/j.apenergy.2016.06.147
Multiphysics, C., 2022. COMSOL multiphysics®.
Narasimhan, T.N., 1999. Fourier's heat conduction equation: History, influence, and connections. Rev. Geophys. 37, 151–172. https://doi.org/10.1029/1998RG900006
Navarro, L., De Gracia, A., Colclough, S., Browne, M., McCormack, S.J., Griffiths, P., Cabeza, L.F., 2016a. Thermal energy storage in building integrated thermal systems: A review. Part 1. active storage systems. Renew. Energy 88, 526–547. https://doi.org/10.1016/j.renene.2015.11.040
Navarro, L., De Gracia, A., Colclough, S., Browne, M., McCormack, S.J., Griffiths, P., Cabeza, L.F., 2016b. Thermal energy storage in building integrated thermal systems: A review. Part 1. active storage systems. Renew. Energy 88, 526–547. https://doi.org/10.1016/j.renene.2015.11.040
Navarro, L., De Gracia, A., Niall, D., Castell, A., Browne, M., McCormack, S.J., Griffiths, P., Cabeza, L.F., 2016c. Thermal energy storage in building integrated thermal systems: A review. Part 2. Integration as passive system. Renew. Energy 85, 1334–1356. https://doi.org/10.1016/j.renene.2015.06.064
Navarro, L., De Gracia, A., Niall, D., Castell, A., Browne, M., McCormack, S.J., Griffiths, P., Cabeza, L.F., 2016d. Thermal energy storage in building integrated thermal systems: A review. Part 2. Integration as passive system. Renew. Energy 85, 1334–1356. https://doi.org/10.1016/j.renene.2015.06.064
Ndiaye, K., Cyr, M., Ginestet, S., 2020. Development of a cementitious material for thermal energy storage at low temperature. Constr. Build. Mater. 242, 118130. https://doi.org/10.1016/j.conbuildmat.2020.118130
Ndiaye, K., Ginestet, S., Cyr, M., LMDC, Université de Toulouse, INSAT, UPS, France, 2018. Thermal energy storage based on cementitious materials: A review. AIMS Energy 6, 97–120. https://doi.org/10.3934/energy.2018.1.97
Nikuradse, J., 1937. Laws of flows in rough pipes. Washington: NACA.
Nikuradse, J., 1933. Stromungsgesetze in rauhen Rohren. Vdi-Forschungsheft 361, 1.
Noble, W.S., 2006. What is a support vector machine? Nat. Biotechnol. 24, 1565–1567. https://doi.org/10.1038/nbt1206-1565
Novotny, V., Basta, V., Smola, P., Spale, J., 2022. Review of Carnot Battery Technology Commercial Development. Energies 15, 647. https://doi.org/10.3390/en15020647
Olabi, A.G., Abdelghafar, A.A., Maghrabie, H.M., Sayed, E.T., Rezk, H., Radi, M.A., Obaideen, K., Abdelkareem, M.A., 2023. Application of artificial intelligence for prediction, optimization, and control of thermal energy storage systems. Therm. Sci. Eng. Prog. 39, 101730. https://doi.org/10.1016/j.tsep.2023.101730

OpenFOAM, 2023.
Optimization Problem Types - Convex Optimization [WWW Document], 2011. . solver. URL https://www.solver.com/convex-optimization (accessed 3.15.23).
Ozisik, M.N., 2013. Boundary Value Problems of Heat Conduction.
Özişik, M.N., Orlande, H.R.B., Colaço, M.J., Cotta, R.M., 2017. Finite Difference Methods in Heat Transfer.
Palomo, A., Grutzeck, M.W., Blanco, M.T., 1999. Alkali-activated fly ashes: A cement for the future. Cem. Concr. Res. 29, 1323–1329. https://doi.org/10.1016/S0008-8846(98)00243-9
Paradowski, B., Sałabun, W., 2021. Are the results of MCDA methods reliable? Selection of materials for Thermal Energy Storage. Procedia Comput. Sci., Knowledge-Based and Intelligent Information & Engineering Systems: Proceedings of the 25th International Conference KES2021 192, 1313–1322. https://doi.org/10.1016/j.procs.2021.08.135
Pedregosa, F., Varoquaux, G., Gramfort, A., Michel, V., Thirion, B., Grisel, O., Blondel, M., Prettenhofer, P., Weiss, R., Dubourg, V., others, 2011. Scikit-learn: Machine learning in Python. J. Mach. Learn. Res. 12, 2825–2830.
Pelay, U., Luo, L., Fan, Y., Stitou, D., Rood, M., 2017. Thermal energy storage systems for concentrated solar power plants. Renew. Sustain. Energy Rev. 79, 82–100. https://doi.org/10.1016/j.rser.2017.03.139
Perera, K.S., Aung, Z., Woon, W.L., 2014. Machine Learning Techniques for Supporting Renewable Energy Generation and Integration: A Survey, in: Woon, W.L., Aung, Z., Madnick, S. (Eds.), Data Analytics for Renewable Energy Integration, Lecture Notes in Computer Science. Springer International Publishing, Cham, pp. 81–96. https://doi.org/10.1007/978-3-319-13290-7_7
Pompei, L., Nardecchia, F., Miliozzi, A., 2023. Current, Projected Performance and Costs of Thermal Energy Storage. Processes 11, 729. https://doi.org/10.3390/pr11030729
Prieto, C., Pino, F.J., Cabeza, L.F., 2023. Techno-economic analysis of a concrete storage concept for parabolic trough solar power plants. J. Energy Storage 58, 106372. https://doi.org/10.1016/j.est.2022.106372
Provis, J.L., Lukey, G.C., Van Deventer, J.S.J., 2005. Do Geopolymers Actually Contain Nanocrystalline Zeolites? A Reexamination of Existing Results. Chem. Mater. 17, 3075–3085. https://doi.org/10.1021/cm050230i
Rafidi, N., Blasiak, W., 2005. Thermal performance analysis on a two composite material honeycomb heat regenerators used for HiTAC burners. Appl. Therm. Eng. 25, 2966–2982. https://doi.org/10.1016/j.applthermaleng.2005.03.004
Rahjoo, M., Goracci, G., Gaitero, J.J., Martauz, P., Rojas, E., Dolado, J.S., 2022a. Thermal Energy Storage (TES) Prototype Based on Geopolymer Concrete for High-Temperature Applications. Materials 15, 7086. https://doi.org/10.3390/ma15207086
Rahjoo, M., Goracci, G., Martauz, P., Rojas, E., Dolado, J.S., 2022b. Geopolymer Concrete Performance Study for High-Temperature Thermal Energy Storage (TES) Applications. Sustainability 14, 1937. https://doi.org/10.3390/su14031937
Rahjoo, M., Rojas, E., Goracci, G., Gaitero, J.J., Martauz, P., Dolado, J.S., 2023. A Numerical Study of Geopolymer Concrete Thermal Energy Storage:

Benchmarking TES Module Design and Optimizing Thermal Performance. https://doi.org/10.2139/ssrn.4469955
Rahman, M.M., Oni, A.O., Gemechu, E., Kumar, A., 2020. Assessment of energy storage technologies: A review. Energy Convers. Manag. 223, 113295. https://doi.org/10.1016/j.enconman.2020.113295
Raschka, S., Mirjalili, V., 2019. Python Machine Learning: Machine Learning and Deep Learning with Python, scikit-learn, and TensorFlow 2. Packt Publishing Ltd.
Raupach, M.R., Antonia, R.A., Rajagopalan, S., 1991. Rough-Wall Turbulent Boundary Layers. Appl. Mech. Rev. 44, 1–25. https://doi.org/10.1115/1.3119492
Ren, G., Chuttar, A., Banerjee, D., 2022. Exploring efficacy of machine learning (artificial neural networks) for enhancing reliability of thermal energy storage platforms utilizing phase change materials. Int. J. Heat Mass Transf. 189, 122628. https://doi.org/10.1016/j.ijheatmasstransfer.2022.122628
Ricklefs, A., Thiele, A.M., Falzone, G., Sant, G., Pilon, L., 2017. Thermal conductivity of cementitious composites containing microencapsulated phase change materials. Int. J. Heat Mass Transf. 104, 71–82. https://doi.org/10.1016/j.ijheatmasstransfer.2016.08.013
Rivera, O.G., Long, W.R., Weiss Jr., C.A., Moser, R.D., Williams, B.A., Torres-Cancel, K., Gore, E.R., Allison, P.G., 2016. Effect of elevated temperature on alkali-activated geopolymeric binders compared to portland cement-based binders. Cem. Concr. Res. 90, 43–51. https://doi.org/10.1016/j.cemconres.2016.09.013
Saeed, R.M., Frick, K.L., Shigrekar, A., Mikkelson, D., Bragg-Sitton, S., 2022. Mapping thermal energy storage technologies with advanced nuclear reactors. Energy Convers. Manag. 267, 115872. https://doi.org/10.1016/j.enconman.2022.115872
Salomoni, V.A., Majorana, C.E., Giannuzzi, G.M., Miliozzi, A., Di Maggio, R., Girardi, F., Mele, D., Lucentini, M., 2014. Thermal storage of sensible heat using concrete modules in solar power plants. Sol. Energy 103, 303–315. https://doi.org/10.1016/j.solener.2014.02.022
Sarbu, I., Sebarchievici, C., 2018. A Comprehensive Review of Thermal Energy Storage. Sustainability 10, 191. https://doi.org/10.3390/su10010191
Sarkar, P.K., Goracci, G., Dolado, J.S., 2024. Thermal conductivity of Portlandite: Molecular dynamics based approach. Cem. Concr. Res. 175, 107347. https://doi.org/10.1016/j.cemconres.2023.107347
Schlichting, H., 1936. Experimentelle Untersuchungen zum Rauhigkeitsproblem. Ing.-Arch. 7, 1–34. https://doi.org/10.1007/BF02084166
Schlichting, H., Gersten, K., 2000. Boundary-layer theory, 8th rev. and enl. ed. ed. Springer, Berlin ; New York.
Scrivener, K.L., Juilland, P., Monteiro, P.J.M., 2015. Advances in understanding hydration of Portland cement. Cem. Concr. Res. 78, 38–56. https://doi.org/10.1016/j.cemconres.2015.05.025
Senior, A.W., Evans, R., Jumper, J., Kirkpatrick, J., Sifre, L., Green, T., Qin, C., Žídek, A., Nelson, A.W.R., Bridgland, A., Penedones, H., Petersen, S., Simonyan, K., Crossan, S., Kohli, P., Jones, D.T., Silver, D., Kavukcuoglu, K., Hassabis, D., 2020. Improved protein structure prediction using potentials from deep learning. Nature 577, 706–710. https://doi.org/10.1038/s41586-019-1923-7

Shafi, H.S., Antonia, R.A., 1995. Anisotropy of the Reynolds stresses in a turbulent boundary layer on a rough wall. Exp. Fluids 18, 213–215. https://doi.org/10.1007/BF00230269
Shah, R.K., Sekulic, D.P., 2003. Fundamentals of Heat Exchanger Design. John Wiley & Sons.
Shameri, M.A., Alghoul, M.A., Sopian, K., Zain, M.F.M., Elayeb, O., 2011. Perspectives of double skin façade systems in buildings and energy saving. Renew. Sustain. Energy Rev. 15, 1468–1475. https://doi.org/10.1016/j.rser.2010.10.016
Sharma, A.K., 2005. Text Book of Correlations and Regression. Discovery Publishing House.
Shaw, M.R., Treadaway, K.W., Willis, S.T.P., 1994. Effective use of building mass. Renew. Energy 5, 1028–1038. https://doi.org/10.1016/0960-1481(94)90130-9
Shettigar, N., Banerjee, D., Truong, M., Thyagarajan, A., Bamido, A., Meza, A., Kumar, N., 2020. Application of Machine Learning for Enhancing the Transient Performance of Thermal Energy Storage Platforms for Supplemental or Primary Thermal Management. Presented at the ASME 2020 Heat Transfer Summer Conference collocated with the ASME 2020 Fluids Engineering Division Summer Meeting and the ASME 2020 18th International Conference on Nanochannels, Microchannels, and Minichannels, American Society of Mechanical Engineers Digital Collection. https://doi.org/10.1115/HT2020-9167
Singh, B., Ishwarya, G., Gupta, M., Bhattacharyya, S.K., 2015. Geopolymer concrete: A review of some recent developments. Constr. Build. Mater. 85, 78–90. https://doi.org/10.1016/j.conbuildmat.2015.03.036
Singh, S., Sørensen, K., 2017. Concrete thermal energy storage for steam generation: A numerical investigation. Presented at the The 58th Conference on Simulation and Modelling (SIMS 58) Reykjavik, Iceland, September 25th – 27th, 2017, pp. 234–240. https://doi.org/10.3384/ecp17138234
Skinner, J.E., Strasser, M.N., Brown, B.M., Panneer Selvam, R., 2014. Testing of High-Performance Concrete as a Thermal Energy Storage Medium at High Temperatures. J. Sol. Energy Eng. 136, 021004. https://doi.org/10.1115/1.4024925
SONG, Y., LU, Y., 2015. Decision tree methods: applications for classification and prediction. Shanghai Arch. Psychiatry 27, 130–135. https://doi.org/10.11919/j.issn.1002-0829.215044
Spalding, D.B., 1974. The numerical computation of turbulent flow. Comp Methods Appl Mech Eng 3, 269.
Steinmann, W.-D., 2022. Thermal energy storage for medium and high temperatures: concepts and applications. Springer, Springer Fachmedien Wiesbaden, Wiesbaden.
STORWORKS POWER, n.d. . STORWORKS POWER. URL https://www.storworks.com/technology
Streb, F., Mengel, M., Schweitzer, D., Kasztelan, C., Schoderbock, P., Ruhl, G., Lampke, T., 2018. Characterization Methods for Solid Thermal Interface Materials. IEEE Trans. Compon. Packag. Manuf. Technol. 8, 1024–1031. https://doi.org/10.1109/TCPMT.2017.2748238

Suárez, C., Pino, F.J., Guerra, J., 2020. A new simplified model for the unsteady response of concrete passive sensible TES systems. J. Energy Storage 27, 101042. https://doi.org/10.1016/j.est.2019.101042

Tamme, R., Laing, D., Steinmann, W.-D., 2004a. Advanced Thermal Energy Storage Technology for Parabolic Trough. J. Sol. Energy Eng. 126, 794–800. https://doi.org/10.1115/1.1687404

Tamme, R., Laing, D., Steinmann, W.-D., 2004b. Advanced Thermal Energy Storage Technology for Parabolic Trough. J. Sol. Energy Eng. 126, 794–800. https://doi.org/10.1115/1.1687404

Tatsidjodoung, P., Le Pierrès, N., Luo, L., 2013. A review of potential materials for thermal energy storage in building applications. Renew. Sustain. Energy Rev. 18, 327–349. https://doi.org/10.1016/j.rser.2012.10.025

Taylor, J.B., Carrano, A.L., Kandlikar, S.G., 2006. Characterization of the effect of surface roughness and texture on fluid flow—past, present, and future. Int. J. Therm. Sci. 45, 962–968. https://doi.org/10.1016/j.ijthermalsci.2006.01.004

Tesfay, M, 2014. CFD analysis of sensible thermal energy storage system using solid medium in solar thermal power plant. Int. J. Adv. Eng. Technol.

Tesfay, Meseret, 2014. Cfd Analysis of Sensible Thermal Energy Storage System Using Solid Medium in Solar Thermal Power Plant. Int. J. Adv. Eng. Technol. 6, 2766–2783.

The hydration of Portland cement, 1978. . Proc. R. Soc. Lond. Math. Phys. Sci. 359, 435–451. https://doi.org/10.1098/rspa.1978.0050

Tyner, C.E., Sutherland, J.P., Gould, J., 1995. Solar two: A molten salt power tower demonstration (No. SAND-95-1828C; CONF-951072-1). Sandia National Lab. (SNL-NM), Albuquerque, NM (United States).

Versteeg, H.K., Malalasekera, W., 2007. An introduction to computational fluid dynamics: the finite volume method, 2nd ed. ed. Pearson Education Ltd, Harlow, England ; New York.

Vigneshwaran, K., Singh Sodhi, G., Muthukumar, P., Subbiah, S., 2019. Concrete based high temperature thermal energy storage system: Experimental and numerical studies. Energy Convers. Manag. 198, 111905. https://doi.org/10.1016/j.enconman.2019.111905

Voyant, C., Notton, G., Kalogirou, S., Nivet, M.-L., Paoli, C., Motte, F., Fouilloy, A., 2017. Machine learning methods for solar radiation forecasting: A review. Renew. Energy 105, 569–582. https://doi.org/10.1016/j.renene.2016.12.095

Wang, H., Lei, Z., Zhang, X., Zhou, B., Peng, J., 2019. A review of deep learning for renewable energy forecasting. Energy Convers. Manag. 198, 111799. https://doi.org/10.1016/j.enconman.2019.111799

Wang, S., Abdulridha, A., Bravo, J., Naito, C., Quiel, S., Suleiman, M., Romero, C., Neti, S., Oztekin, A., 2023a. Thermal energy storage in concrete: Review, testing, and simulation of thermal properties at relevant ranges of elevated temperature. Cem. Concr. Res. 166, 107096. https://doi.org/10.1016/j.cemconres.2023.107096

Wang, S., Abdulridha, A., Bravo, J., Naito, C., Quiel, S., Suleiman, M., Romero, C., Neti, S., Oztekin, A., 2023b. Thermal energy storage in concrete: Review, testing, and simulation of thermal properties at relevant ranges of elevated temperature. Cem. Concr. Res. 166, 107096. https://doi.org/10.1016/j.cemconres.2023.107096

Wilcox, D.C., 1998. Turbulence modeling for CFD, 2nd ed. ed. DCW Industries, La Cãnada, Calif.

Xie, G.N., Chen, Q.Y., Zeng, M., Wang, Q.W., 2008. Thermal Design of Heat Exchanger With Fins Inside and Outside Tubes. Presented at the ASME Turbo Expo 2006: Power for Land, Sea, and Air, American Society of Mechanical Engineers Digital Collection, pp. 263–268. https://doi.org/10.1115/GT2006-90260

YEGNANARAYANA, B., 2009. ARTIFICIAL NEURAL NETWORKS. PHI Learning Pvt. Ltd.

Zanganeh, G., 2014. High-temperature thermal energy storage for concentrated solar power with air as heat transfer fluid (Doctoral Thesis). ETH Zurich. https://doi.org/10.3929/ethz-a-010280563

Zhang, Y., Faghri, A., 1996. Heat transfer enhancement in latent heat thermal energy storage system by using the internally finned tube. Int. J. Heat Mass Transf. 39, 3165–3173. https://doi.org/10.1016/0017-9310(95)00402-5

Zunft, S., Hänel, M., Krüger, M., Dreißigacker, V., Göhring, F., Wahl, E., 2011. Jülich Solar Power Tower—Experimental Evaluation of the Storage Subsystem and Performance Calculation. J. Sol. Energy Eng. 133, 031019. https://doi.org/10.1115/1.4004358